# General Disclaimer

One or more of the Following Statements may affect this Document

- This document has been reproduced from the best copy furnished by the organizational source. It is being released in the interest of making available as much information as possible.

- This document may contain data, which exceeds the sheet parameters. It was furnished in this condition by the organizational source and is the best copy available.

- This document may contain tone-on-tone or color graphs, charts and/or pictures, which have been reproduced in black and white.

- This document is paginated as submitted by the original source.

- Portions of this document are not fully legible due to the historical nature of some of the material. However, it is the best reproduction available from the original submission.

(NASA-CR-169744) THE ISOTROPIC CONDITION OF
ENERGETIC PARTICLES EMITTED FROM A LARGE
SOLAR FLARE Ph.D. Thesis (California Inst.
of Tech.) 202 p HC A10/MF A01 CSCL 03B

N83-16272

Unclas
G3/92 02413
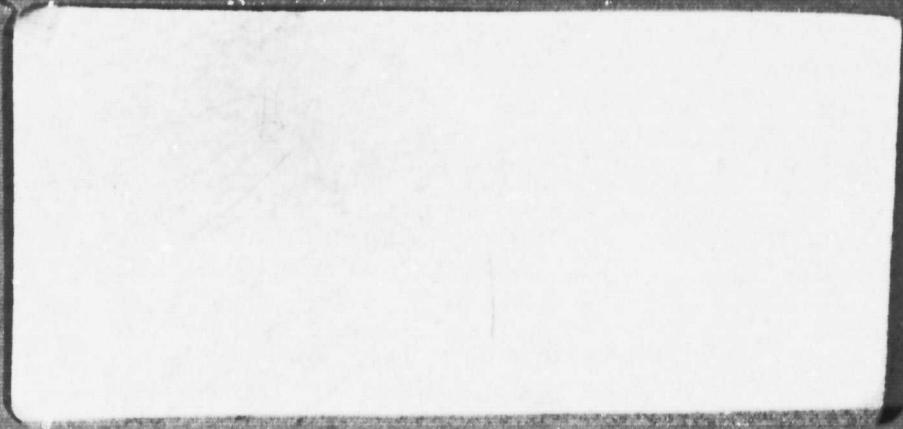
CALIFORNIA INSTITUTE OF TECHNOLOGY

The Isotopic Composition of Energetic Particles
Emitted from a Large Solar Flare

Thesis by
John Spalding

In Partial Fulfillment of the Requirements
for the Degree of
Doctor of Philosophy

California Institute of Technology
Pasadena, California

1983

(Submitted November 23, 1982)

(SRL 82-11)

Acknowledgements

I would like to thank my advisor, Edward Stone, for suggesting this project and for providing scientific and personal help and guidance. I would also like to thank Richard Mewaldt for all the help and criticism that he has given me throughout my graduate career.

I was fortunate to be associated with the HIST project. HIST was conceived, built, tested, and calibrated by a team led by Edward Stone and Rochus Vogt and consisting of William Althouse, Alan Cummings, Thomas Garrard, and Richard Mewaldt. I have greatly benefited from discussions with all of these men. Many others at SRL have contributed to the HIST project, including Brownley Gauld, Neil Hickey, and Marty Smith. Rick Cook has contributed proportional counters used in the calibration of HIST and provided advice about data analysis and interpretation. Neil Gehrels and Keith Krombel as fellow graduate students acted as sounding boards for ideas and schemes.

I would like to thank my parents, Margaret and Donald Spalding, for the encouragement they have given me, and I would like to thank my wife, Donna Livant, for her love and for being understanding and helpful as I completed this thesis.

Abstract

We report measurements of isotope abundance ratios for 5-50 MeV/nuc nuclei from a large solar flare that occurred on September 23, 1978. The measurements were made by the Heavy Isotope Spectrometer Telescope (HIST) on the ISEE-3 satellite orbiting the Sun near an Earth-Sun libration point approximately one million miles sunward of the Earth. We report finite values for the isotope abundance ratios $^{13}C/^{12}C$, $^{15}N/^{14}N$, $^{18}O/^{16}O$, $^{22}Ne/^{20}Ne$, $^{25}Mg/^{24}Mg$, and $^{26}Mg/^{24}Mg$, and upper limits for the isotope abundance ratios $^3He/^4He$, $^{14}C/^{12}C$, $^{17}O/^{16}O$, and $^{21}Ne/^{20}Ne$.

We measured element abundances and spectra to compare the September 23, 1978 flare with other flares reported in the literature. The flare is a typical large flare with "low" Fe/O abundance (≤ 0.1).

For $^{13}C/^{12}C$, $^{15}N/^{14}N$, $^{18}O/^{16}O$, $^{25}Mg/^{24}Mg$, and $^{26}Mg/^{24}Mg$, our measured isotope abundance ratios agree with the solar system abundance ratios of Cameron (1981). For neon we measure $^{22}Ne/^{20}Ne = 0.109 + 0.026 - 0.019$, a value that is different with confidence 97.5% from the abundance measured in the solar wind by Geiss et al. (1972) of $^{22}Ne/^{20}Ne = 0.073 \pm 0.001$. Our measurement for $^{22}Ne/^{20}Ne$ agrees with the isotopic composition of the meteoritic component neon-A.

Separate arguments appear to rule out simple mass fractionation in the solar wind and in our solar energetic particle measurements as the cause of the discrepancy in the comparison of the apparent compositions of these two sources of solar material.

Table of Contents

Chapter 1 - Introduction

The isotope abundances of the light elements in the solar system contain information that is useful to several fields of science. Theories of nucleosynthesis and solar system formation try to explain the observed isotope abundances. Geologists can use observed isotope abundance patterns as tracers of various geophysical processes on the Earth, planets, and meteorites.

A important observation, that has emerged after years of study, is that the pattern of isotope abundances is remarkable homogeneous. To a high degree of accuracy the relative abundances of different isotopes, for a given element, are the same in rocks analyzed from the moon, meteorites, or from Peoria, Illinois. A very good first approximation to the observed isotope abundance patterns states that the relative isotope abundances for a given element are independent of the source of the sample containing the element.

A more accurate model for observed solar system isotope abundance patterns postulates that the solar system was formed out of an initially isotopically homogeneous ball of gas or "soup". Some small present day isotope abundance differences might be expected in this model, as the result of physical and chemical fractionation processes operating on the solar system's initial isotopically homogeneous ancestral "soup".

It is only recently, that convincing evidence has been uncovered about inhomogeneity in the initial isotope abundance patterns of the "soup" out of which the solar system formed. In oxygen (Clayton, Grossman, and Mayeda 1973), and in magnesium and heavier elements (Wasserburg, Papanastassiou, and Lee 1979), isotope abundance anomalies have been found that differ from

terrestrial abundances by up to 5-6%. This may be evidence for inhomogeneity in the initial solar system isotope abundance pattern. In neon, Eberhardt *et al.* (1979) have found much larger differences from the common meteoritic components. A neon-E component was discovered which has over 5 times the $^{22}Ne/^{20}Ne$ abundance ratio measured in the "planetary" component of meteorites.

In view of the importance of the isotope abundance patterns in the solar system, it is interesting to study the isotopic composition of the Sun. The Sun is the largest reservoir of solar system material, containing over 99% of the total mass of the solar system. Yet, when most researchers quote "solar system" isotope abundances, they quote abundances obtained from laboratory analysis of terrestrial, lunar, or meteoritic material. The Sun is a qualitatively different type of solar system object than the objects (Earth, moon, and meteorites) from which solar system isotopic abundance information is typically obtained. Information about the isotopic composition of the Sun might be used to check theories about the isotopic fractionation of the solar system's ancestral "soup" or to check the hypothesis that the ancestral "soup" was initially isotopically homogeneous. However, observational constraints make isotope abundance measurements of the Sun very difficult, and as a result, isotope abundances on the Sun are not very well known.

The determination of solar isotope abundances with analysis of the spectra of radiation emitted by the Sun is a difficult task. Electronic transitions in different isotopes of the same element are so close in energy that weak isotope lines may be unidentifiable due to overlap from the wings of adjacent stronger isotope lines. Rotational and vibrational transitions have been analyzed, but require the existence of molecules, and thus a cooler environment than the solar photosphere. The atmosphere above sunspots provides the necessary

cooler environment, but there are still many systematic and observational problems. In one analysis, the $^{12}C/^{13}C$ isotope abundance ratio was determined to an accuracy of 15%, the $^{16}O/^{18}O$ abundance ratio was determined to an accuracy of 35%, and the $^{17}O/^{18}O$ abundance ratio was only determined to within a factor of two (Hall, Noyes, and Ayres 1972).

Isotope abundances have been measured in the solar wind for noble gases (Geiss 1973), but the measurement of other elements presents formidable difficulties.

Solar energetic particles (SEPs) are a sample of the solar system material accelerated to high energies by the explosive energy release mechanisms that operate in solar flares. The measurement of the isotopic composition of SEPs might be useful for the study of the isotopic composition of the Sun or to study the flare environment that produced the SEPs. The isotopic composition of the SEPs might also provide useful information about nuclear reactions that occur during solar flares.

Several technical innovations have recently been applied to a spacecraft SEP detection system, constructed from a stack of silicon solid state particle detectors. The innovations include priority systems to select particles with charge $Z \geq 3$ for detailed analysis, trajectory measuring devices to reduce the mass measurement uncertainty for charged particles, stable electronics, improved solid state detectors, and heavy ion calibrations. These developments have made it possible to measure the isotopic composition of SEPs. In particular, the instrument HIST, flown on the satellite ISEE-3 (Althouse *et al.* 1978), can measure the isotopic composition of nuclei with charges $1 \leq Z \leq 28$ and energies 5 MeV/nuc $\leq E \leq$ 200 MeV/nuc.

We will report on the isotopic composition of SEPs, observed with HIST, from a large solar flare that occurred on September 23, 1978. We measured

isotope abundance ratios for $^{13}C/^{12}C$, $^{15}N/^{14}N$, $^{18}O/^{16}O$, $^{22}Ne/^{20}Ne$, $^{26}Mg/^{24}Mg$, and $^{25}Mg/^{24}Mg$, and upper limits to the abundance ratios, $^{3}He/^{4}He$, $^{14}C/^{12}C$, $^{17}O/^{16}O$, and $^{21}Ne/^{20}Ne$. We obtain results that are consistent with solar system abundances, except in the case of neon, where the solar $^{22}Ne/^{20}Ne$ abundance ratio is controversial. The SEP measurement of $^{22}Ne/^{20}Ne$ disagrees with the measurement of $^{22}Ne/^{20}Ne$ in the solar wind of Geiss *et al.* (1972), but agrees with the meteoritic component neon-A.

Separate arguments appear to rule out simple mass fractionation in the solar wind and in our solar energetic particle measurements as the cause of the discrepancy in the comparison of the apparent compositions of these two sources (solar wind and SEPs) of solar material.

Chapter 2 - The Experiment

2.1. HIST Overview

The Heavy Isotope Spectrometer Telescope experiment, (HIST), was designed to measure the isotopic composition of nuclei with energies in the range from 5 to 250 MeV/nucleon and in the charge range with Z = 3 to 28. A general overview of HIST is available in Althouse *et al.* (1978), and here we will concentrate only on the characteristics of HIST that are relevant to measurements made in a solar flare particle environment.

HIST is carried on the spacecraft ISEE-3 described by Ogilvie *et al.* (1977, 1978). ISEE orbits the Sun at approximately the location of a Sun-Earth libration point, about one million miles sunward of the Earth. This orbit is an ideal observation point for solar particle measurements because it is distant enough from the Earth that the Earth's magnetosphere does not disturb the solar particle measurements.

The design of HIST can be understood and partitioned as two separate tasks, single particle identification and the generation of rate and telemetry information. We will first describe the physical structure of HIST which is relevant to the single particle detection task and give a brief explanation of the particle detection method. We will then discuss the generation of rate and telemetry information. Finally, we will present a calculation of the instrument's nominal mass resolution.

2.2. The HIST Particle Detection Telescope

HIST includes a stack of eleven silicon solid-state particle detectors arranged to form a particle telescope, and the associated signal processing electronics. Figure 2.2.1 is a schematic diagram of the telescope, and table 2.2.1 is a list of the detectors that comprise it. Detectors M1 through D3 are

silicon surface-barrier solid-state detectors. Detectors D4 through D9 are Li-drifted detectors with a central detection area and an annular guard ring (shaded in figure 2.2.1), which is used as an active anti-coincidence shield. The nominal detection areas for the detectors are 505 $mm.^2$ for M1 and M2, 600 $mm.^2$ for D2 and D3, and 920 $mm.^2$ for detectors D4 through D9.

Single particle identification in HIST is accomplished by a multiple parameter analysis of the energy deposition history of an ion slowing down in the silicon particle detectors. As is well known (Bertolini and Coche 1968), for a wide range of energies, the charge collected from a reverse-biased silicon diode is proportional to the amount of energy lost by a fast ion passing through the diode. In HIST the detectors M1 through D8 are connected to charge sensitive preamps and amplifiers. The amplifiers' outputs are digitized by a series of 4096 channel analog to digital converters, with one ADC for each detector. The result is a series of pulse heights that are a measure of the energy loss of the ion in each detector.

A particular innovation of this telescope is the use of two position sensitive silicon solid-state detectors (M1 and M2), as a hodoscope to measure the incoming ion's trajectory. Detectors M1 and M2 are special surface-barrier solid-state detectors that have had their metallic contacts deposited as 24 parallel strips with a 1 mm. spacing, rather than as one large electrode. On each detector the metallic strips on one side are perpendicular to the metallic strips on the other side. Each strip has a separate preamplifier and discriminator. Thus when an ion passes through "matrix detectors" M1 or M2, the position where the ion penetrated the detector is known. Figure 2.2.2 shows a picture of one such detector.

Table 2.2.1 -

HIST Detectors

Detector	Nominal Thickness (μ of Si)	Detector Type	Nominal Gain (MeV/chan)	Nominal Threshold (MeV)	A Ω[d] ($cm^2 str$)
M1	50	sb--Mdet[a]	0.121	0.30	---
M2	50	sb-Mdet	0.121	0.30	0.79
D1	90	sb[b]	0.227	0.54	0.73
D2	150	sb	0.296	0.71	0.73
D3	500	sb	0.617	1.46	0.72
D4	1700	Li--D[c]	1.160	2.76	0.70
D5	3000	Li-D	1.531	3.64	0.66
D6	3000	Li-D	1.531	3.64	0.60
D7	6000	Li-D	2.272	5.41	0.53
D8	6000	Li-D	2.272	5.41	0.46
D9	3000	Li-D	---	0.19	0.40

[a] surface-barrier detector - "matrix detector"
[b] surface-barrier detector
[c] Lithium drifted detector
[d] estimated error: ± 0.01

figure 2.2.1 - A schematic diagram (to scale) of the HIST particle detection telescope. The shaded areas of detectors D4 to D9 are annular guard rings used as an active anti-coincidence shield.
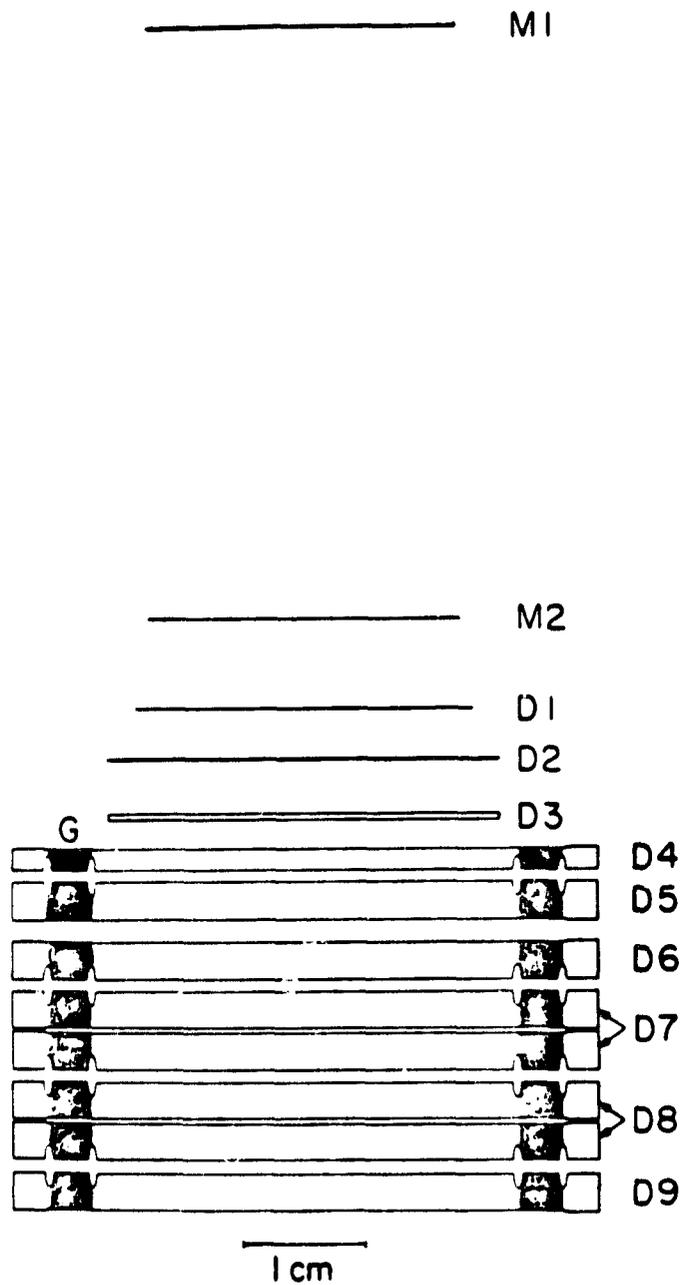
figure 2.2.2 - A photograph of a matrix detector showing the 24 separate charge collection electrodes. The electrodes have a nominal spacing of ≈ 1 mm. The other side of the matrix detector also has 24 charge collection electrodes, which run in the orthogonal direction to the electrodes shown.

2.3. Single Particle Identification

Particle identification in HIST is based upon a two parameter analysis method called dE/dX - E, that is valid for ions that stop in the particle detector stack. Figure 2.3.1 shows an ion of charge Z, mass M, and energy E, which entered the telescope stack at an angle ϑ, and then stopped in the detector stack. The ion has passed through a detector of thickness T, depositing there an energy ΔE, and stopped in a second detector, losing there an energy E'. If the range in silicon, of an ion of charge Z and mass M, is R(Z,M,E), then the equations

$$\frac{T}{\cos\vartheta} = R(Z,M,E) - R(Z,M,E') \quad . \tag{2.3.1}$$

$$\text{and } E = E' + \Delta E \quad . \tag{2.3.2}$$

express the relations between the variables.

Equations 2.3.1 and 2.3.2 are two equations for the three unknowns E, M, and Z. For a given charge estimate z^*, there is a solution $M(z^*)$ of 2.3.1, for each ΔE and E'. Thus, it seems that we must estimate the charge independently, if we are to measure the ion's mass M. Actually, there is a third implicit equation that allows a solution for both Z and M. We can use the fact that the incident nuclei are stable as a constraint on the number of isotopes that can exist for a given charge Z. For example, a ^{14}N ion is incident on the telescope, and deposits 94.62 MeV in D2 and 41.22 MeV in D1. The solutions are then M = 20.844 amu for $z^* = 6$, M = 14.003 amu for $z^* = 7$, and M = 9.921 amu for $z^* = 8$. The $z^* = 6$ and $z^* = 8$ solutions can be eliminated, because the solutions, $M(z^*)$, are not near the masses of stable or long-lived radioactive isotopes. Then the only solution for a stable isotope is M = 14.003 amu, and Z = 7. Throughout the entire operating range of HIST, unique solutions for M and Z are always possible.

Figure 2.3.2 is a plot of ΔE vs. E' for ions that stop in D2, for all stable

isotopes with charges in the interval $2 \leq Z \leq 14$. Each labeled line, or track, is the locus of all possible ΔE, E' pairs for a given ion that stops in D2. Here, it is easy to see that there is no ambiguity in the solution for M and Z. The isotope tracks shown are well separated.

Figure 2.3.3 is a plot of ΔE vs. E' for data spanning the time interval from 1978: 286 to 1978:272, for ions that stop in detector D2. The figure 2.3.3 data set consists of "raw" data. No consistency requirements have been placed on the data to reduce the background apparent below the carbon track, for example. For the following two reasons, only charge tracks are visible. First, ions incident at different angles have different track positions, and the figure 2.3.3 data set accepted all incident angles out to $\approx 25°$. Secondly, each charge has only one abundant isotope. We will later find, for example, that ^{13}C has an abundance only 1% as large as ^{12}C, so that separate isotope tracks may be too faint to be seen on this type of plot.

figure 2.3.1 - A schematic diagram illustrating the basic components of the
dE/dX - E technique of particle detection.
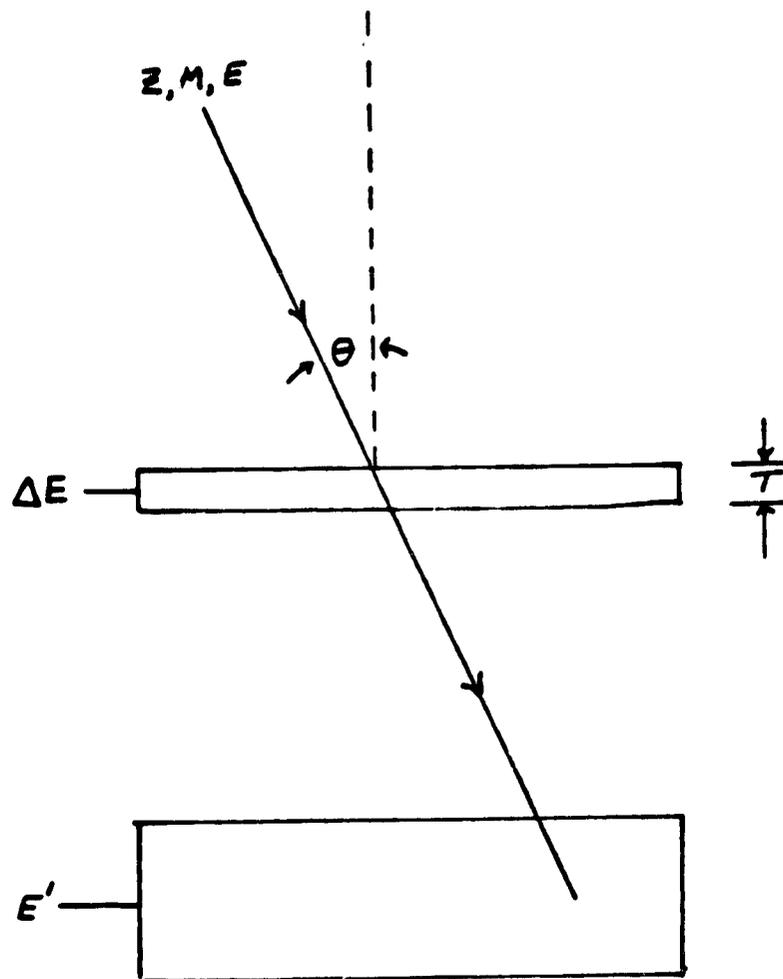
figure 2.3.2 - Calculated tracks of ΔE vs. E' for all stable isotopes with $2 \le Z \le 14$, that stop in detector D2. ΔE is the energy deposited in the 90μ thick detector D1. E' is the energy deposited in the 150μ thick detector D2.

- 15 -
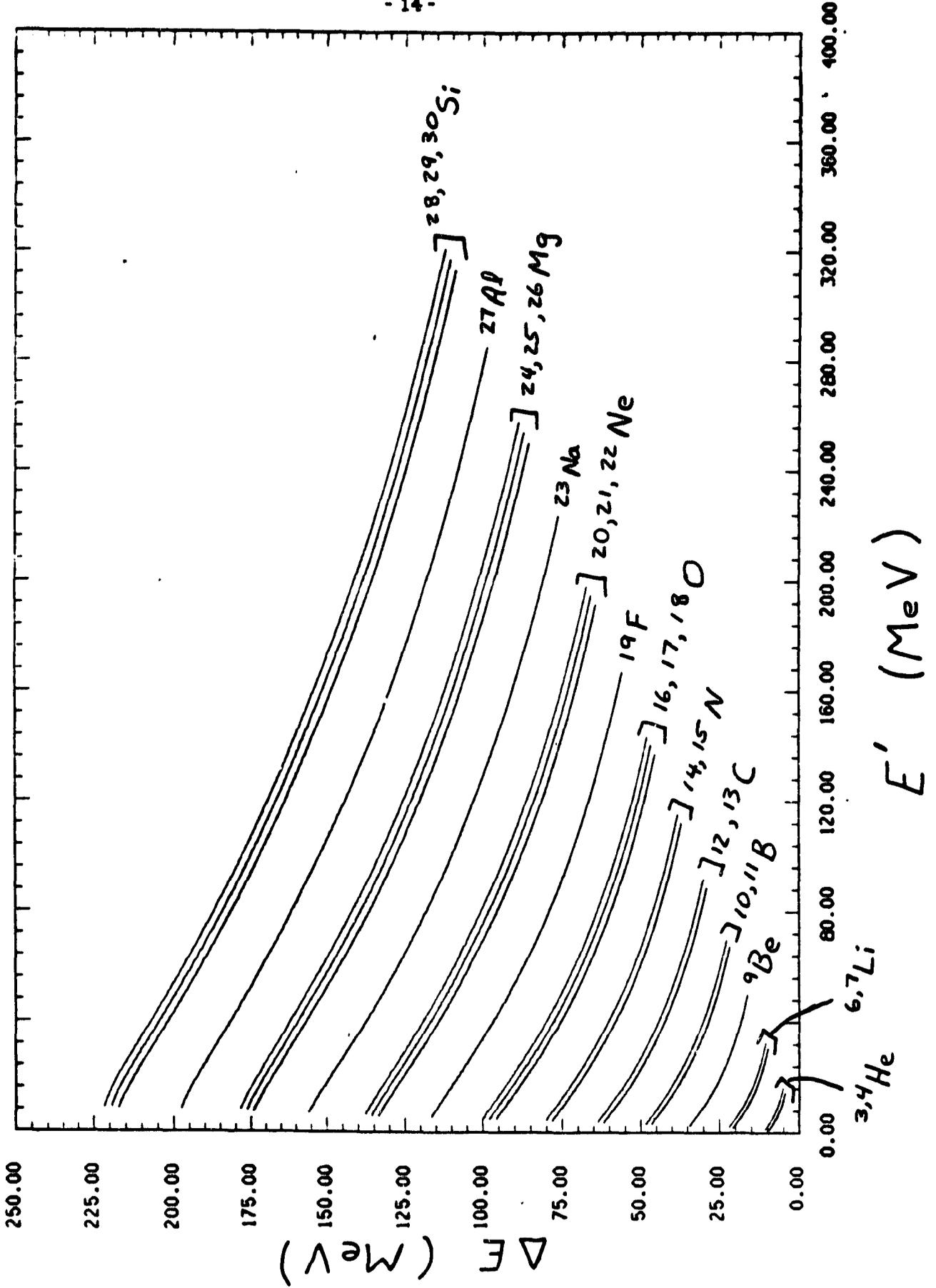
figure 2.3.3 - A plot of ΔE vs. E' with experimental data for particles that stop in detector D2. Each point corresponds to one event. The figure 2.3.3 data set consists of "raw" data. No consistency requirements have been placed on the data. ΔE is the energy deposited in the 90μ thick detector D1. E' is the energy deposited in the 150μ thick detector D2.

RANGE 2
78:266 - 78:272

E' (MeV)

ΔE (MeV)

2.4. Event and Rate Records

An event refers to the simultaneous occurrence of a signal above the detector thresholds in detectors M1 and M2. The telemetry record kept by HIST of the set of pulse heights, hodoscope discriminator triggers and and other information, coincident with an event trigger, is called an event record. The deepest detector in the stack triggered by the particle determines the RANGE. An event is a RANGE 0 event if M2 and M1 are triggered. An event is a RANGE 3 event if D3 is the deepest detector triggered. In an event record up to five detector pulse heights are recorded. The pulse height for M1, PHA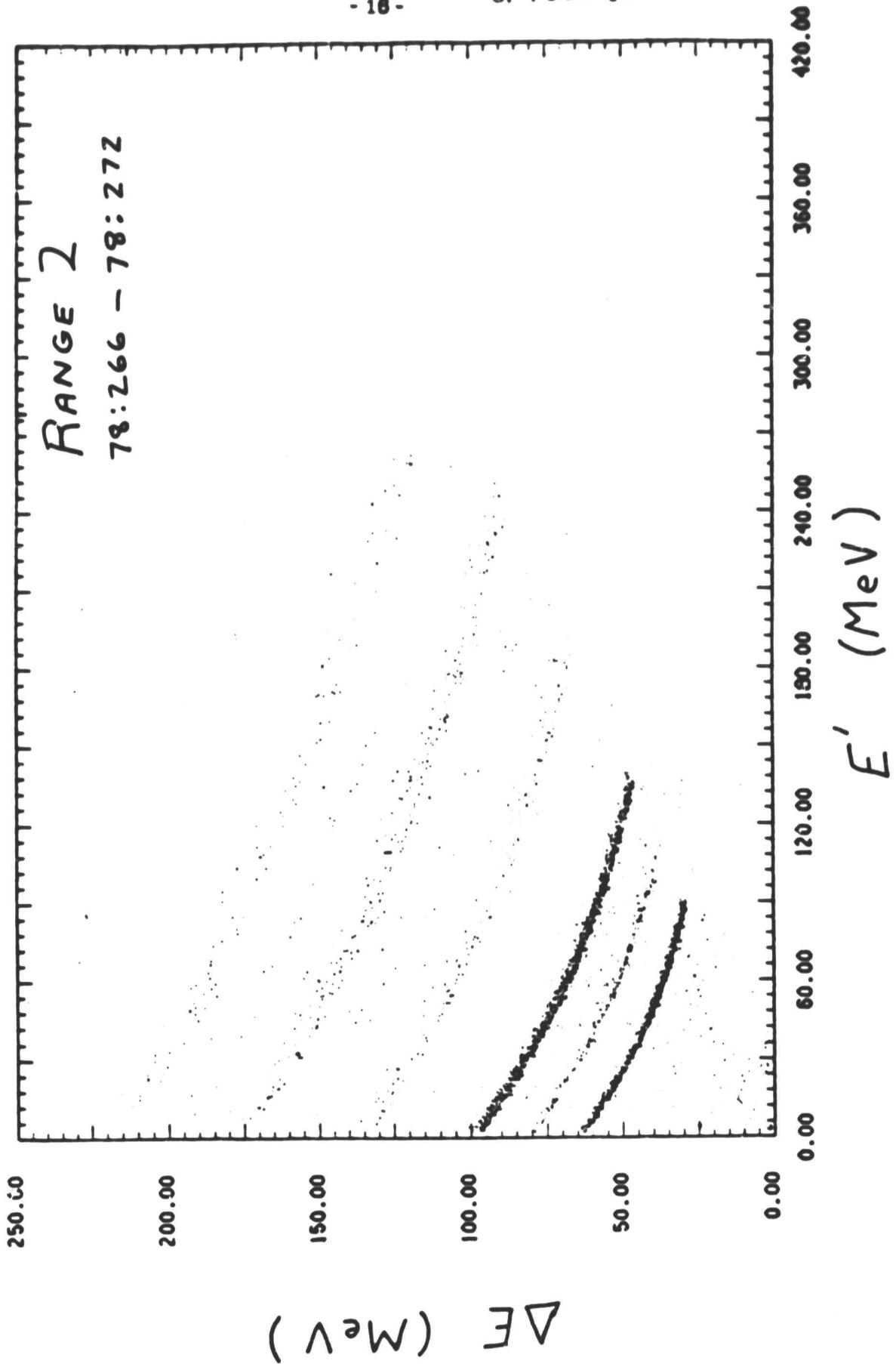M1, is always recorded. The pulse height from the deepest triggered detector in the stack, PHA1, is also always recorded. Up to three pulse heights from the next three detectors above the deepest triggered detector are recorded. The three pulse heights are named PHA2, PHA3, and PHA4, with the convention that PHA2 is the pulse height of the next detector above the deepest triggered detector in the stack. A particle that enters the stack and stops in D5, has PHA1 for the D5 pulse height, and PHA2 for the D4 pulse height.

The pattern of triggered strips in the matrix detector is not stored directly in the event record, but is processed to extract the significant information. Any set of as many as four adjacent triggered strips is called a group. The hodoscope electronics counts the number of strips in a group, and the number of groups on each side (plane) of each matrix detector. If only one group of strips is triggered in a matrix detector plane, the event record contains the address of the highest numbered strip, and the number of strips in the group, called the strip count. For two groups of strips, the event record contains the addresses of highest numbered strip and the strip count for each group. With two or more groups of strips in *any* matrix detector plane, we have a condition known as the multiple hodo condition, or MH. The MH condition prevents us

from assigning a unique one particle trajectory to the pattern of triggered strips in the hodoscope. For three or more groups of strips, the event record contains only the strip address and strip count for the first group, as well as a record that three or more groups have fired.

HIST also classifies an event as one of either PEN, HIZ or LOZ. The PEN class contains all events that trigger detector D9, the last detector in the detector stack. All "stopping events", that is, events that trigger detectors M2 through D8 as the deepest detector, are either HIZ or LOZ. The HIZ condition is a requirement that the charge of the particle be $Z \geq 3$, as determined by two parameter pulse height analysis. The LOZ condition is a requirement that the charge of the particle be $Z \leq 2$. This is accomplished with a "box discriminator". The HIZ, LOZ, and PEN conditions can be written as a set of logical equations, with

$$Z3 = (PHA1 > H_j) \; OR \; (PHA2 > H_{j-1}) \; OR \tag{2.4.1}$$
$$\left[(PHA1 > L_j) \; AND \; (PHA2 > L_{j-1}) \right].$$

$$HIZ = Z3 \cdot \overline{D9} \cdot M1 \cdot M2 \tag{2.4.2}$$

$$LOZ = \overline{Z3} \cdot \overline{D9} \cdot M1 \cdot M2 \tag{2.4.3}$$

$$PEN = D9 \cdot M1 \cdot M2 \tag{2.4.4}$$

Here, j specifies the detector, and H_j and L_j are the commandable high and low discriminator settings, listed in table 2.4.1.

Table 2.4.1 -

Box Discriminator Levels

Detector	(channels) H Discriminator	(MeV)	(channels) L Discriminator	(MeV)
M1	144	12.82	120	10.14
M2	136	11.55	104	8.08
D1	128	16.46	96	9.59
D2	136	23.48	96	12.37
D3	96	41.33	56	16.91
D4	128	82.94	104	56.93
D5	128	107.96	96	62.33
D6	128	109.82	96	63.76
D7	128	156.87	96	90.45
D8	128	160.61	96	94.14

HIST has 159 rate registers, that are read out to ISEE-3 every 64 seconds, to make a rate record. The rate registers count the number of occurrences of various coincidence requirements, and are listed in table 2.4.2. Rates 1-16 refer to "sectored" rates. ISEE-3 is spinning about a fixed axis in space, normal to the ecliptic plane, and the sectors specify the 45° octant, relative to the Sun, into which HIST points. Rates 1-8 accumulate only when HIST is not busy processing triggers or generating event records, and thus measure the live time in each sector. Rate registers 29 through 159 are only accumulated part time, they are active from 1/3 to 1/24 of the time depending on the specific rate register.

Table 2.4.2 -

HIST Rate Registers

Rate Register	Purpose
1-8	50 khz. sectored live time clock
9-16	sectored HIZ events
17-25	range distribution of HIZ events
26	LOZ events
27	PEN events
28	ADC triggers
29-124	matrix detector single strip triggers
125-132	range distribution of LOZ events
133-142	single detector triggers
143-146	matrix detector triggers by plane
147-149	single detector triggers
150-159	guard ring triggers

2.5. Telemetry and Event Sampling

A very important characteristic of the ISEE-3 spacecraft system is the telemetry bandwidth allocated to HIST, 16 eight bit bytes per second, for communications from the spacecraft to the ground. HIST has the capability to *count* particles at rates of over 5×10^4 particles per second. HIST can also send complete event records to the spacecraft at over 5×10^2 particle events per second. At the ISEE-3 telemetry rate allocated to HIST, a maximum of only ≈ 0.9 event record per second can be returned to Earth. Thus it was necessary to design a data sampling system that made some rough cuts in the data, and sent only significant samples back to the ground. We will describe a very simple functional model for HIST, a ' then show how it meets the special needs of measurements in the solar flare environment.

The solar flare particle environment in which HIST must make measurements is characterized by particle spectra that decline rapidly with energy. If F_i is the flux per unit energy, for a given element averaged over a solar flare, and F_i is fit to the functional form $F_i = AE^{-\gamma}$, then γ is often found to be in the range 3 to 5. The spectral shapes for different elements are often roughly similar and the relative abundances are not too different from solar system abundance tables, such as Cameron's (1981), though systematic trends do appear in the data (Cook 1981).

Suppose there is a solar flare with $F_i = A_i E^{-3.5}$, and all the elements have the same spectral form. Suppose that the element abundance distribution is the same as the Cameron (1981) abundance table. Then, if HIST observes 10^4 carbon nuclei in RANGE 0, there will be 2030 carbon nuclei in RANGE 1, 484 in RANGE 2, 174 in RANGE 3 and 30 carbon nuclei in RANGE 4. If 10^8 protons are observed in RANGEs 0 through 3, then there will be in RANGEs 0 through 3, 7.2×10^6 helium nuclei, 5800 carbon, 6050 oxygen, 616 neon, and 119 iron

nuclei. The solar flare particle environment is weighted strongly towards the low RANGEs and hydrogen and helium nuclei.

What we desire as experimenters, is an event sample with a more equal distribution of elements and RANGEs. The higher RANGEs have better mass resolution, and more pulse height measurements of each particle are available as checks on measurement errors. When measuring spectra, for a given number of events, the least uncertainty in the spectral shape occurs when there are roughly equal numbers of event samples per RANGE. For the measurement of the ratio of the abundances of two elements, the minimum uncertainty in the abundance ratio is obtained when there are equal numbers of event samples per element.

HIST has an event sampling system that partially meets some of the needs expressed in the previous paragraph. HIST has eleven registers in which to store event records while waiting for the ISEE-3 spacecraft to periodically request data to send to Earth. Nine of the registers are reserved for HIZ event records, with RANGEs 0 through 8. One register each is reserved for LOZ and PEN event records. HIZ events are given absolute priority. Each time the spacecraft requests an event record, a HIZ event record is read out, if there are any event records stored in the HIZ registers. If R is the RANGE of the last HIZ event record read out then registers for RANGEs R-1, R-2, ... 0, 8, ... and R are checked in turn. This feature makes the HIZ event sample have a more equal RANGE distribution. Only if no HIZ event records are available, is either a LOZ or a PEN event record read out to the spacecraft.

The measurement process is started when the signal in any one of the detectors exceeds the threshold energy listed in table 2.2.1. In a relatively quick period of time ($\approx 10\,\mu s$) HIST decides whether or not to generate an event record. HIST first determines if an event has occurred and whether the

event meets the specified coincidence requirements. Then HIST checks to see if there is an empty register in which to store the event record. In the same period of time the appropriate rate registers are incremented. If there is an empty event register of the proper type, HIST will complete the measurement task, generate an event record, and load it into an event register. This takes about 1 ms. If there is no empty event register of the proper type, HIST will reset itself and wait for the next event trigger. Because HIST has only to provide event records to ISEE-3 at the maximum rate of ≈ 0.9 per second it can operate at triggering rates $\approx 5 \times 10^4$ per second, rather than at maximum triggering rates of $\approx 5 \times 10^5$ per second, that would be necessary if HIST had to read out every trigger as an event record.

2.6. Theoretical Mass Resolution in HIST

The solution of equation 2.3.1 for the mass estimator

$$M(z^-) = M(z^\bullet, L, E', \Delta E) \qquad (2.3.1)$$

depends on three experimentally determined quantities, E', ΔE and the pathlength $L = \dfrac{T}{\cos\theta}$ in the ΔE detector. We will examine how experimental errors and physical fluctuations in L, E' and ΔE affect the width of the distribution of the mass estimator. We will follow and expand upon the treatment of Stone and Vogt (1972).

We will now examine the structure of equation 2.3.1 under the influence of two simplifying assumptions. The first assumption is that the incident particle is going fast enough when it passes through the slab of thickness L that the ion is fully stripped of electrons. Then the range of an ion of mass M and charge Z is

$$R(Z,M,E) = \frac{1}{Z^2}\frac{M}{M_p} R_p\left[1, M_p, E(\frac{M_p}{M})\right] = \frac{A}{Z^2} R_p(\frac{E}{A}) \qquad (2.6.2)$$

where R_p is the range of a proton, M_p is the proton's mass, and $A = \dfrac{M}{M_p}$. A

further assumption is that

$$R_p = k \left[\frac{E}{A}\right]^\lambda \tag{2.6.3}$$

with k = 11.71 microns of silicon and $\lambda = 1.775$. Within the energy interval $10\ MeV \le \frac{E}{A} \le 200\ MeV$ equation 2.6.2 reproduces the tabulated proton range in silicon given by Janni (1966) with a maximum error of less than 3%.

Equation 2.3.1 then becomes

$$A = \frac{L\ Z^2}{\left[R_p(\frac{E}{A}) - R_p(\frac{E'}{A})\right]} \tag{2.6.4}$$

or

$$A = \left[\frac{L\ Z^2}{k\left[E^\lambda - (E')^\lambda\right]}\right]^{\frac{1}{1-\lambda}} \tag{2.6.5}$$

The derivatives that we need for our error analysis are given below,

$$\frac{\partial M}{\partial L}\bigg|_E = \left[\frac{-1}{\lambda-1}\right]\frac{M}{L} \tag{2.6.6}$$

$$\frac{\partial M}{\partial E'}\bigg|_E = -\frac{\partial M}{\partial \Delta E}\bigg|_E = \left[\frac{\lambda}{\lambda-1}\right]\frac{M}{E'}\left[\frac{R}{L}-1\right] \tag{2.6.7}$$

$$\frac{\partial M}{\partial \Delta E}\bigg|_{E'} = \left[\frac{\lambda}{\lambda-1}\right]\frac{M}{E}\left[\frac{R}{L}\right] \tag{2.6.8}$$

$$\frac{\partial M}{\partial E}\bigg|_{\Delta E} = \left[\frac{\lambda}{\lambda-1}\right]\frac{M}{E}\left[1 - \frac{R}{L}(1 - \frac{E'}{E})\right] \tag{2.6.9}$$

where $R = R(Z,M,E)$. The uncertainty in M from fluctuations in N independent quantities, x_i, each with uncertainty σ_{x_i}, is

$$(\sigma_M)^2 = \sum_{i=1}^N \left[\sigma_{M,x_i}\right]^2 \tag{2.6.10}$$

where

$$\sigma_{M,x_i} = \sigma_{x_i}\ \frac{\partial M}{\partial x_i}\bigg|_{x_j,\ j \neq i}. \tag{2.6.11}$$

If we look at the structure of equations 2.6.6-9 they can be written as

$$\frac{\partial M}{\partial z_i} = \left(\frac{M}{z_i}\right) \frac{1}{\lambda-1} f_i \left(\frac{R}{L}, \frac{E}{E'}, \lambda\right) \tag{2.6.12}$$

where f_i is of order 1. Thus the relative precision that we will get in the mass measurement is about the same as the relative precision to which L, E', and ΔE are known as

$$\frac{\sigma_{M, z_i}}{M} = \frac{\sigma_{z_i}}{z_i} \frac{1}{\lambda-1} f_i . \tag{2.6.13}$$

Thus a mass uncertainty of 0.20 amu at ^{20}Ne, as will be demonstrated, means that all quantities must be known to a precision of better than 1%.

2.6.1. Pathlength Variations

Equations 2.6.5 and 2.6.10 show that

$$\frac{\sigma_{M, L}}{M} = \left[\frac{1}{\lambda-1}\right] \frac{\sigma_L}{L} \approx 1.29 \frac{\sigma_L}{L} . \tag{2.6.1.1}$$

One cause of the variation in the pathlength is variation in the thickness of the ΔE detector from place to place on the detector. Since the position at which a given incident particle hits a particular detector can be extrapolated with the position information obtained in the instrument hodoscope, the instrument response can be corrected for thickness variations in the detectors by the use of thickness maps.

The thickness variations of the HIST detectors were measured using particle beams. A beam of constant energy was incident on a particle hodoscope and then penetrated the detector to be mapped. The thickness of the detector can then be calculated using the amount of energy deposited in the detector and the value of dE/dX, the energy loss per unit distance, appropriate to the particle. The particle hodoscope was an argon proportional counter. Three different particle beams were used, protons from the Caltech Kellogg Laboratory van de Graaff accelerator at 8-12 MeV, argon ions at $\approx$ 900 MeV/nuc, and iron ions at $\approx$ 600 MeV/nuc from the Lawrence Berkeley Laboratory Bevalac.

Most of the detectors had measurable thickness variations, with $\frac{\delta T}{T}$ of order 1%. The thickness maps were stored on 1 mm grids, to a precision of $\approx 0.2\%$.

A possible limitation of this mapping technique is its inability to discriminate between variations in detector thickness and positional variations in the charge collection efficiency of the detector. Another limitation of the particle mapping technique is that the absolute thickness of the detector can only be determined to the same accuracy to which the relationship between range and energy is known.

The other source of pathlength variations arises from variations in the incident particle's angle ϑ, expressed in the equation $L = \frac{T}{\cos\vartheta}$. Suppose that a particle intersects detector M1 at (x_1, y_1) and M2 at (x_2, y_2), as illustrated in figure 2.6.1.1. For ease in calculation, let $y_1 = y_2$, and assume that x_2 is known without error. Then, $\Delta x \le x_2 - x_1 \le \Delta x + w$, for w equal to the matrix detector strip width, if we assume that only one M1 matrix detector strip has fired.

$$\sigma_L = \frac{\partial L}{\partial \vartheta} \frac{\partial \vartheta}{\partial (x_2 - x_1)} \sigma_{x_2 - x_1} \qquad (2.6.1.2)$$

to first order and

$$\sigma_{x_2 - x_1} = \frac{w}{\sqrt{12}}. \qquad (2.6.1.3)$$

If both x_1 and x_2 are confined to an interval of width w, on matrix detectors M1 and M2, then σ_L is $\sqrt{2}$ larger. Then we get a final result for the pathlength uncertainty,

$$\frac{\sigma_L}{L} = \frac{\sin\vartheta \cos\vartheta}{\sqrt{6}} \left[\frac{w}{l} \right] \qquad (2.6.1.4)$$

with l equal to the separation of detectors M1 and M2. This result also holds for $y_1 \ne y_2$. At the maximum incident angle for HIST of $\approx 25°$, and with parameters $w = 1$ mm and $l = 50$ mm, $\frac{\sigma_L}{L} = 0.0031$. For [20]Ne this translates to a maximum

mass uncertainty $\sigma_M = 0.061$ amu. For a better estimate we can average in quadrature $\frac{\sigma_L}{L}$ over an isotropic distribution of incident particles so that

$$\left[\frac{\sigma_L}{L}\right]^2\Bigg|_{rms\ ave} = \frac{\int (\frac{\sigma_L}{L})^2 \cos\theta\ dA\ d\Omega}{\int \cos\theta\ dA\ d\Omega} \qquad (2.6.1.5)$$

The case with the largest $<\frac{\sigma_L}{L}>$ would be range 0 particles. If we approximate M1 and M2 as disks of radius 1.2 cm, and integrate numerically, $<\frac{\sigma_L}{L}> = 0.00174$, corresponding to $\sigma_M(^{20}Ne) \approx 0.045$ amu, and $\sigma_M(^{56}Fe) \approx 0.126$ amu.

figure 2.6.1.1 - A schematic diagram of a particle passing through the HIST

hodoscope.
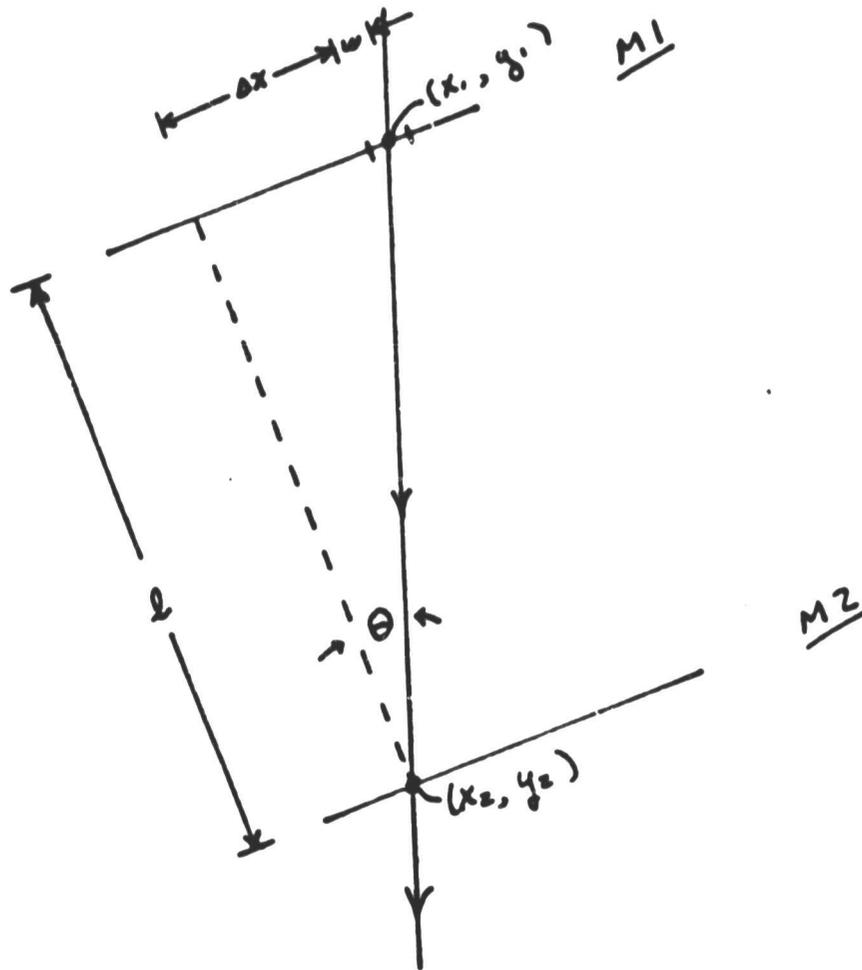
2.6.2. Energy Loss Fluctuations

When an ion passes through the ΔE detector the amount of energy lost, ΔE, fluctuates essentially because the number of electrons that the ion "hits" is a statistical process. Rossi (1952) describes this energy loss fluctuation process from a semi-classical viewpoint, for thin detectors. For thick detectors a correction factor for the thin detector result, developed in Spalding (1981), is needed. The correction factor accounts for the fact that a particle's energy changes significantly as it passes through a thick detector. The result is

$$\sigma_{\Delta E}^2 = \sigma_o^2 \, h(\beta) \, L \, D^2 \qquad (2.6.2.1)$$

where

$$\sigma_o^2 = Z^2 \, (\, 0.135 \, MeV \,)^2 \, / \, (mm \; of \; silicon) \qquad (2.6.2.2)$$

and

$$h(\beta) = \gamma^2 \left(1 - \frac{\beta^2}{2}\right) \; . \qquad (2.6.2.3)$$

D^2 is the correction factor for the thin detector result and in our power law range energy approximation,

$$D^2 = \left[\frac{\lambda}{3\lambda-2}\right] \frac{R}{L} \left[(1 - \frac{L}{R})^{\frac{2}{\lambda}-2} - (1 - \frac{L}{R}) \right] \; . \qquad (2.6.2.4)$$

For large $\frac{R}{L}$, we have a thin detector pathlength and $D^2 \approx 1$. Table 2.6.2.1 shows D as a function of $\frac{R}{L}$ for $\lambda = 7/4$ and demonstrates that the correction is important for $\frac{R}{L} \leq 2$.

Table 2.6.2.1 -

Thick detector correction factor

R/L	D	R/L	D
1.01	5.33	2.00	1.19
1.05	2.77	3.00	1.10
1.10	2.14	5.00	1.05
1.25	1.59	10.0	1.02
1.50	1.34	20.0	1.009

To compute the mass estimator uncertainty we need the derivative of M with respect to ΔE, equation 2.6.7, at fixed E. This is because the energy loss fluctuations of ΔE and E' are correlated, with $\delta (\Delta E) = -\delta (E')$, as long as the particle still stops within the E' detector. Then

$$\sigma_{M, \Delta E} = \frac{\lambda}{\lambda-1} \frac{M}{E} \left[\frac{R}{L} - 1\right]^{\frac{1}{2}} \sigma_o \left[h(\beta) L\right] D \qquad (2.6.2.5)$$

and

$$\sigma_{M, \Delta E} = \sigma_{M \Delta E}(0) \frac{R}{L} \left[(\frac{R}{L})^{2-\frac{2}{\lambda}} - (\frac{R}{L} - 1)^{2-\frac{2}{\lambda}} (1 - \frac{L}{R})\right] . \qquad (2.6.4.6)$$

Figure 2.6.4.11 shows $\sigma_{M, \Delta E}$ as a function of $\frac{R}{L}$ for a 3 mm detector. As a function of $\frac{R}{L}$, $\sigma_{M, \Delta E}$ has a finite intercept, $\sigma_{M, \Delta E}(0)$, at $\frac{R}{L} = 1$, and then monotonically increases. For the power law approximation the intercept is given by

$$\sigma_{M, \Delta E}(0) = \left[\frac{\lambda}{\lambda-1}\right] \frac{M}{E} \left[\frac{\lambda \sigma_o^2 h(\beta) L}{3\lambda-2}\right]^{\frac{1}{2}} \qquad (2.6.2.6)$$

and in silicon for $\lambda = 7/4$,

$$\sigma_{M, \Delta E}(0) = 1.712 \, Z \, M \left[\frac{.135 \, MeV}{E(L)}\right] \left[h(\beta) (\frac{L}{1mm})\right]^{\frac{1}{2}} \qquad (2.6.3.7)$$

where E(L) is the energy for the ion to go a distance L. For a 3 mm. detector this works out to $\sigma_{M, \Delta E}(0) = 0.117$ amu for ^{56}Fe, and $\sigma_{M, \Delta E}(0) = 0.042$ amu for ^{20}Ne. These are fundamental limits for this thickness of detector.

2.6.3. Energy Measurement Errors

The effect of uncertainties in the measurement of ΔE or E' can be computed using equations 2.6.8-9 and 2.6.10. In particular, note that at R/L = 1 errors in ΔE and E' are equally important since

$$\lim_{\frac{R}{L} \to 1} \frac{\partial M}{\partial E'}\bigg|_{\Delta E} = \frac{\lambda}{\lambda-1} \frac{M}{E(L)} \qquad (2.6.3.1)$$

where E(L) is the energy for the ion to go a distance L.

Digitization of the energy signal causes an uncertainty $\frac{c}{\sqrt{12}}$, where c is the energy width of one pulse height channel. Except for very small signals such as for proton and helium ions, this contribution to the mass uncertainty is negligible. For a ^{20}Ne ion in range 2 with R/L = 1, σ_M (*digitization*) = 0.016 *amu*.

An electronic calibration of HIST was performed, introducing a signal of known charge at the preamp inputs by allowing a test pulse of known height to charge up a test capacitor. The calibration was done at several temperatures over the full dynamic range of the ADC's. Thirty points per detector were taken, approximately logarithmically spaced in energy. The result is that the charge to pulse height conversion is known to better than one half of a channel. Comparison with the digitization error shows that electronic calibration errors are of the same order and thus negligible.

2.6.4. Deviation of the Range Energy Equation From the Power Law Form

A single power law representation of the range energy relationship with A/Z^2 scaling is only an approximation for the range of energies and ion species measured by HIST. To calculate the mass uncertainty, two approximations were made, that the proton range energy equation could be approximated by a power law form and that ions were completely stripped of their atomic electrons while slowing down. At the lowest energies in the HIST operating region both of these factors become increasingly important. We have therefore carried out calculations to examine to what extent the mass resolution calculations depended on the above two assumptions.

To evaluate

$$\sigma_{M,\Delta E} = \sigma_o \left[h(\beta) L \right]^{\frac{1}{2}} D \left. \frac{\partial M}{\partial \Delta E} \right|_E \qquad (2.6.4.1)$$

for arbitrary range energy relations, D and $\frac{\partial M}{\partial \Delta E}$ must be computed numeri-

cally. $\frac{\partial M}{\partial \Delta E}$ was computed by finite differences and D was calculated using numerical techniques from Spalding (1981).

To assess the effects of the power law approximation, the range energy equation for protons was obtained by integrating (Marmier and Sheldon 1969)

$$\frac{dE}{dX} = \left(\frac{\sigma_0^2}{mc^2}\right) Z^2 \frac{1}{\beta^2} \left[\ln(\frac{2mc^2}{I}) + \ln(\beta^2) - \ln(1-\beta^2) - \beta^2 \right] . \quad (2.6.4.2)$$

with I = 170 eV. In figure 2.6.4.1, we plotted $\sigma_{M, \Delta E}$ vs. R/L for ^{56}Fe ions, as a set of solid lines, assuming complete stripping of the ion. The dashed lines are the single power law approximation of equation 2.6.2.6, and the lines are labeled by the pathlength L. This power law approximation is a very good approximation, except for R/L ≥ 4 for the 3000μ detector. This corresponds to R ≥ 12 mm and $E \geq 200$ MeV/ nuc, or RANGE 7 and 8 events, which are not important for solar flare particles.

To describe the effects of incomplete stripping, ions were assumed to lose energy at a rate

$$\frac{dE}{dX} = (Z^*)^2 \left.\frac{dE}{dX}\right|_{proton} \quad (2.6.4.3)$$

where Z^* is the effective charge, and the relation

$$\left(\frac{Z^*}{Z}\right)^2 = \frac{1}{1+q} \quad where \quad q = 1.3 \; x \; 10^{-6} \; \frac{Z^{\frac{8}{3}}}{\beta^{\frac{7}{3}}} \quad (2.6.4.4)$$

(Barkas and Berger, 1964) was used. The range of an ion was then obtained by integrating $(\frac{dE}{dX})^{-1}$. $\sigma_{M, \Delta E}$ was then calculated for ^{56}Fe ions, with pathlengths in the ΔE detector of 50μ, 90μ, 150μ, 500μ, and 3000μ, and plotted in figure 2.6.4.2. The 3000μ power law results are plotted for comparison. With incomplete stripping, the ion does not slow down as fast as when stripped. Thus an effective range energy power law exponent "λ" $= E \frac{d(\ln R)}{dE}$ would be lower than for a stripped ion. A lower "λ" will raise $\sigma_{M, \Delta E}$, as it is proportional to $\frac{1}{\lambda-1}$.

Also, a slower ion will have a lower "λ" then a faster ion. Thus, the thinner detectors will have larger $\sigma_{M,\Delta E}$ at the same R/L, which the calculations illustrate.

In figure 2.6.4.3, $\sigma_{M,\Delta E}$ vs. R/L is shown for a pathlength of 50μ and ions ^{4}He, ^{12}C, ^{20}Ne, ^{28}Si, ^{40}Ca, and ^{56}Fe, along with power law results for comparison. Here we can see that only for ions with charges $Z \geq 14$ will the power law approximation to $\sigma_{M,\Delta E}$ be a serious underestimate for moderate $R/L \leq 2$. For the thicker detectors the power law approximation will work better. For $Z \leq 14$, and detectors with $L \geq 90\mu$, the power law approximation provides a result with acceptable error. Since iron is the only element analyzed in this report with $Z \geq 14$, figures 2.6.4.2-3 and the power law approximation span the necessary range to calculate $\sigma_{M,\Delta E}$ for this work.

figure 2.6.4.1 - A calculation of $\sigma_{M,\Delta E}$ for ^{56}Fe ions, assuming complete stripping. The solid lines use the range energy curve obtained by integrating equation 2.6.4.2 and the dashed lines are the power law approximation. The lines are labeled by the value of the pathlength L.
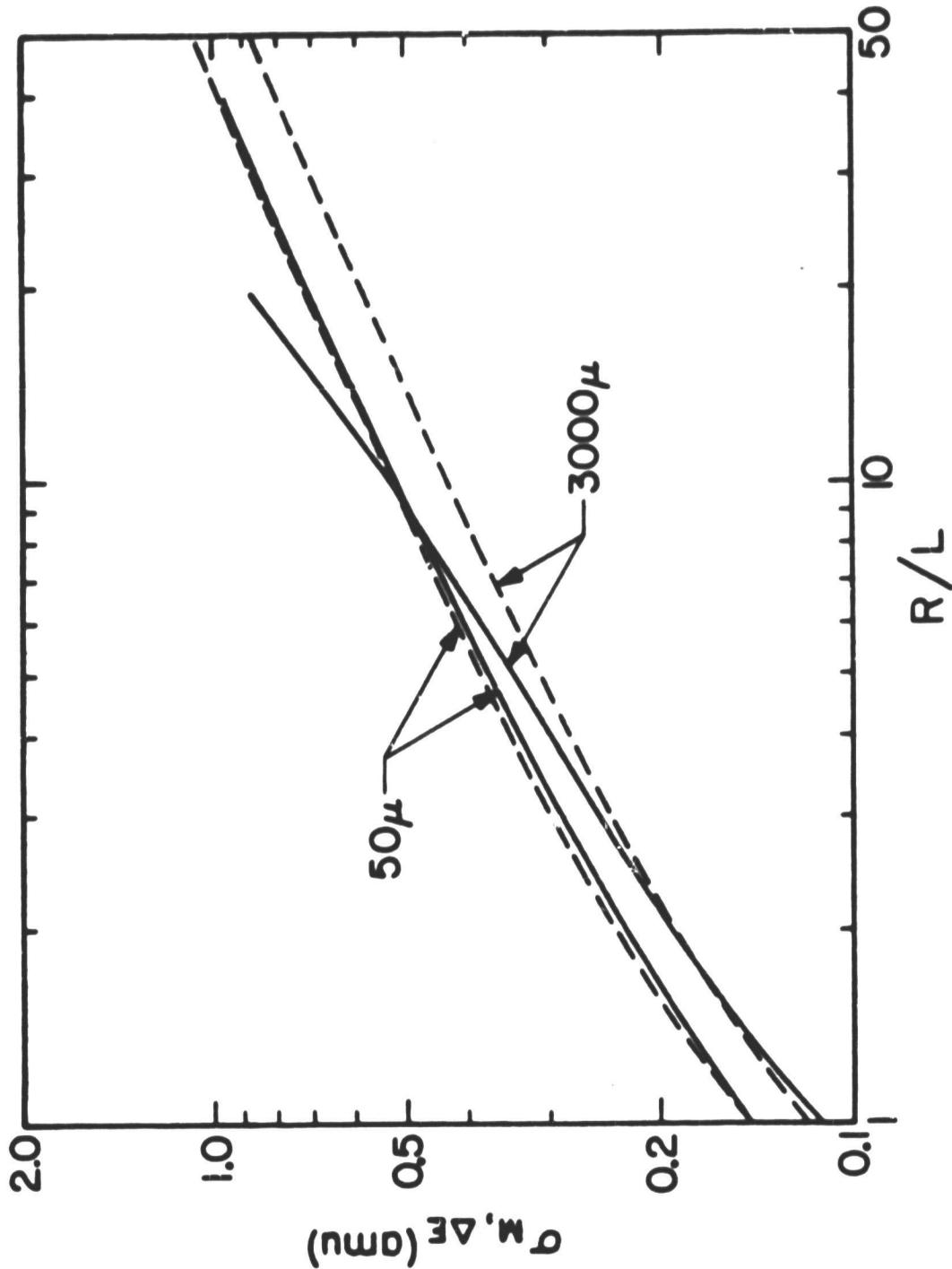
figure 2.6.4.2 - Calculation of $\sigma_{M,\Delta E}$ for ^{56}Fe with the Barkas and Berger (1964) effective charge. The lines are labeled by the value of the path-length L and the dashed line is the power law approximation.
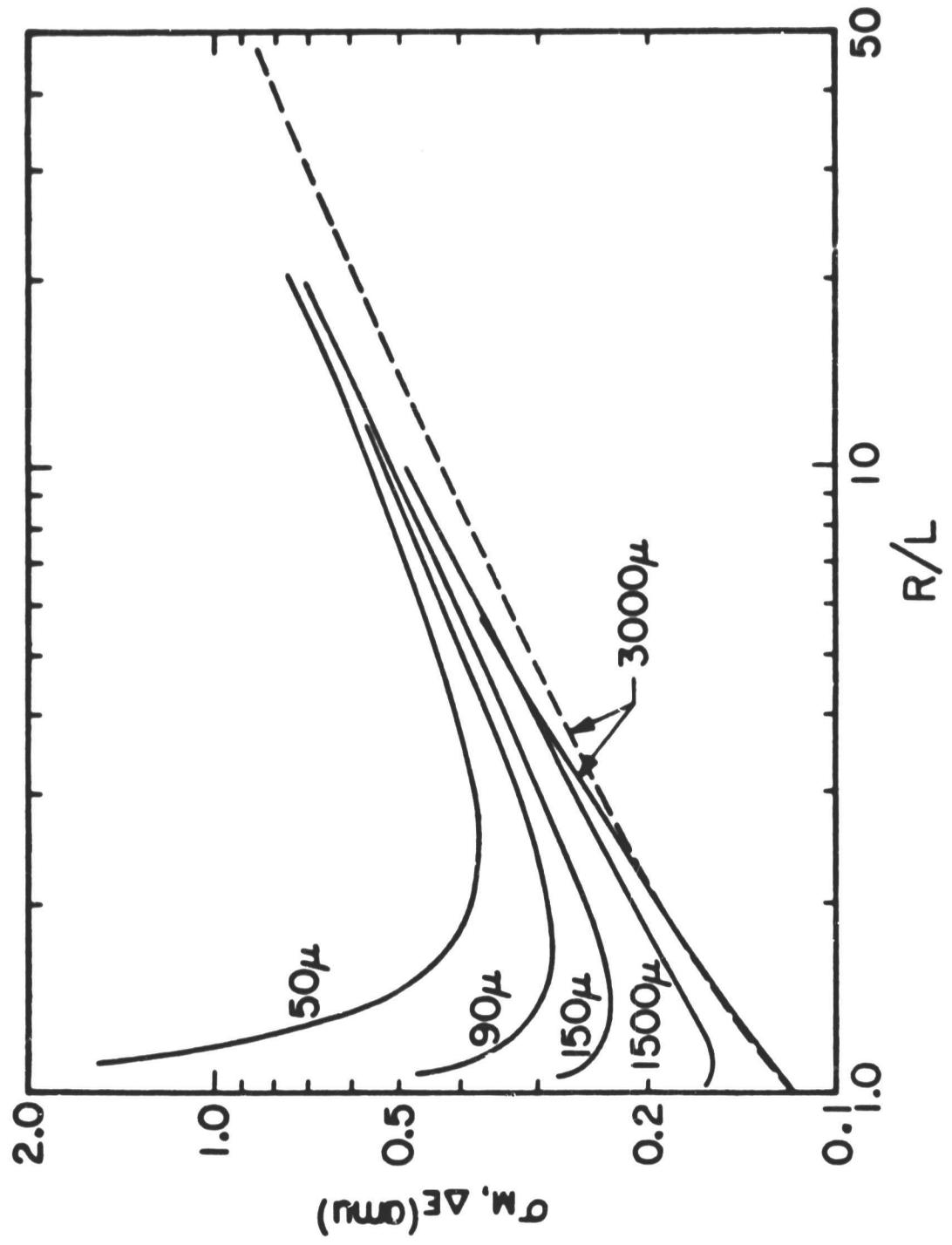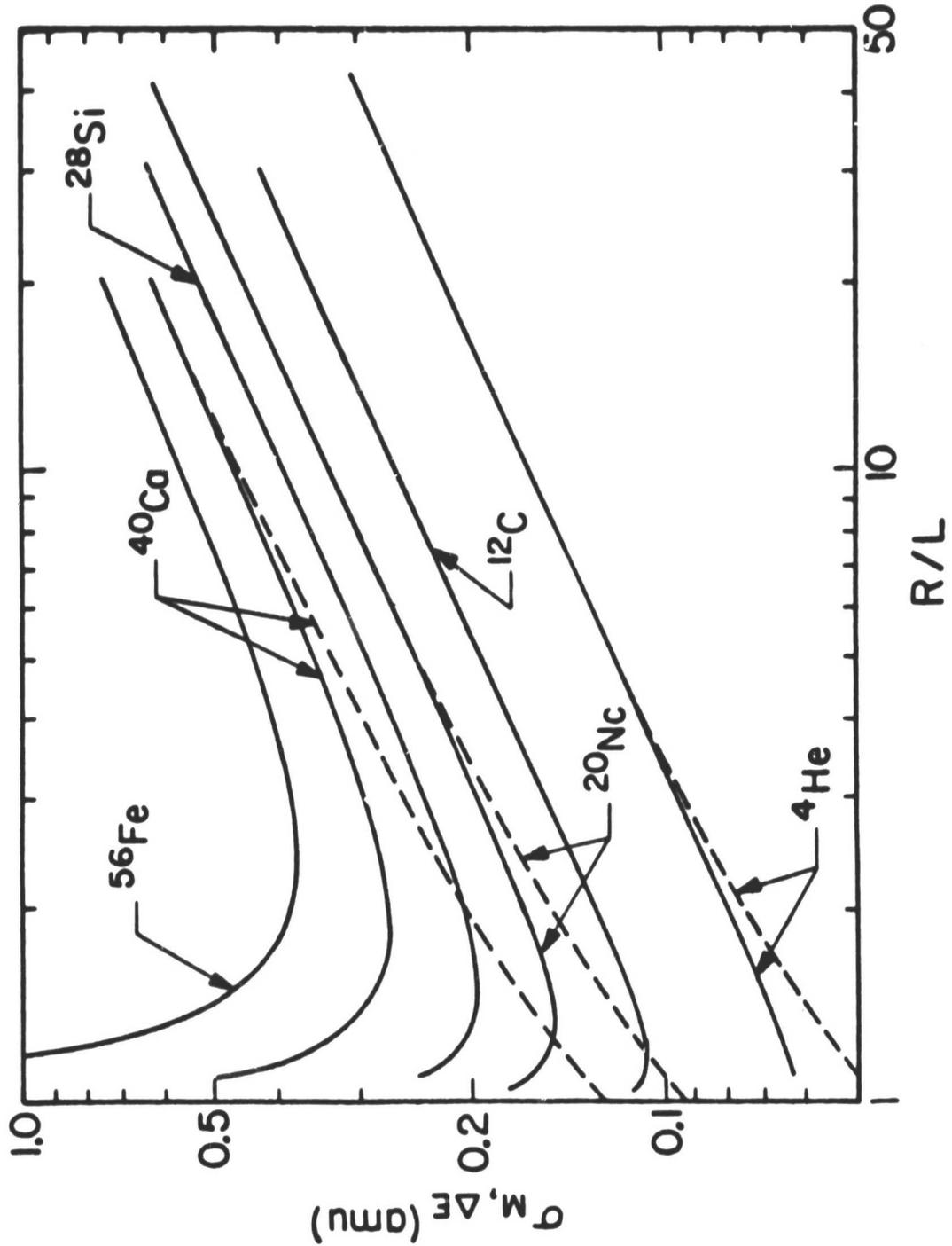
figure 2.6.4.3 - Calculation of $\sigma_{M,\Delta E}$ for a 50μ pathlength L and with Barkas and Berger effective charge for various ions. The dashed lines are the power law approximation.

Just as a reduced "λ" tends to increase $\frac{\partial M}{\partial \Delta E}$, a reduced "$\lambda$" will also increase $\frac{\partial M}{\partial L}$. The correction for incomplete stripping at low energies affects the derivative $\frac{\partial M}{\partial L}$ used to calculate the effect of pathlength variations on the mass estimator. In the single power law approximation the value of this derivative given by equation 2.6.5 is a constant, as a function of R/L. The derivative was calculated numerically using the Barkas and Berger (1964) effective charge. The reduced derivative

$$\frac{\partial M}{\partial L}\bigg|_{reduced} = \frac{\frac{\partial M}{\partial L}(numerical\ calculation)}{\frac{\partial M}{\partial L}(power\ law\ approximation)} \qquad (2.6.4.5)$$

was calculated for ^{56}Fe ions and pathlengths of 50μ, 90μ, 150μ, and 500μ of silicon, and is shown in figure 2.6.4.4. For the 50μ detector, incomplete stripping causes $\sigma_{M,L}$ to be $\geq 50\%$ larger than the value given by the single power law approximation, for R/L $\leq$ 2.30. For lower charges the effect is not so severe, for silicon and a 50μ pathlength, $\frac{\partial M}{\partial L}\bigg|_{reduced} \geq 1.50$ only for $R/L \leq 1.40$, and for neon $\frac{\partial M}{\partial L}\bigg|_{reduced} \geq 1.50$ for $R/L \leq 1.20$.

figure 2.6.4.4 - Calculations of the reduced derivative $\frac{\partial M}{\partial L}$, as defined in equation 2.6.4.5, for ^{56}Fe and with the Barkas and Berger effective charge. The lines are labeled by the value of the pathlength L.
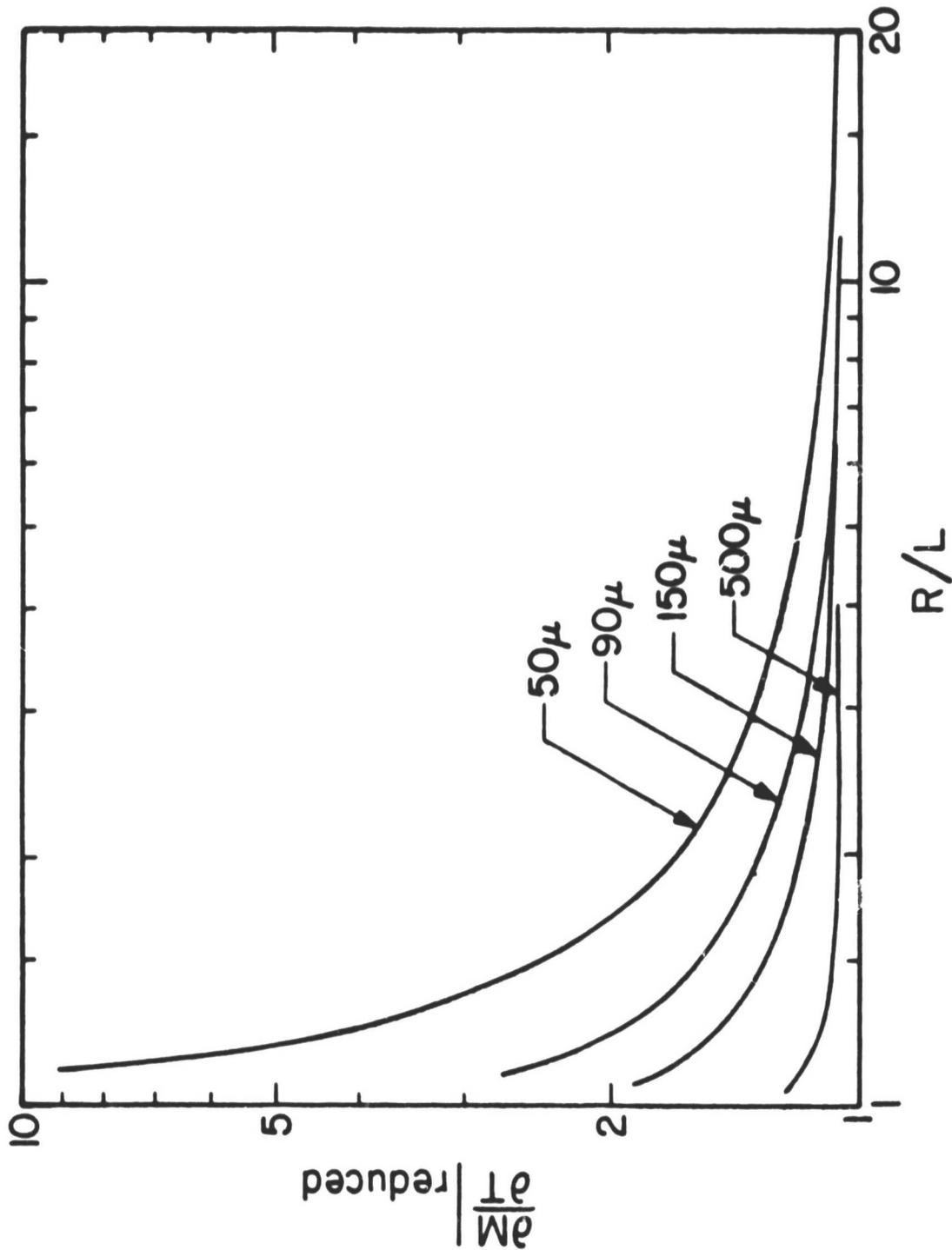
For Fe ions, the inclusion of information about the charge state of the ions, represented by the Barkas and Berger correction, in the calculations for $\sigma_{M, L}$ and $\sigma_{M, \Delta E}$, substantially changes the results. For detectors thinner than 150μ, and for $R/L \leq 3$, the mass resolution is substantially worse than would be predicted if the ions were completely stripped of their atomic electrons. The Barkas and Berger correction is only approximate and was derived from measurements in emulsions, rather than in silicon. We can use the Barkas and Berger correction as a guide to see where the incomplete stripping of atomic electrons influences the mass resolution. An accurate evaluation of incomplete stripping's effects on $\sigma_{M L}$ and $\sigma_{M \Delta E}$, may require more accurate knowledge of the ion's charge state as a function of velocity, than is represented by the Barkas and Berger correction.

2.6.5. Summary

For table 2.6.5.1 we have calculated the nominal mass resolution of HIST for RANGE 1, 2, and 3 events in an idealized situation. The E' detector used was the deepest triggered detector in the stack and the ΔE detector used was the second deepest triggered detector. We used the Barkas and Berger effective charge to do the computations, which were carried out for $R/L = 2$. We assumed a flat detector and that $\frac{\sigma_L}{L} = 0.00174$, as calculated in section 2.6.1. We calculated the mass uncertainty due to digitization and ignored the mass uncertainty due to uncertainties in the electronic calibration. The mass resolution uncertainty due to energy loss fluctuations dominates the mass uncertainty for this choice of parameters. For the heavier ions, the second most important contribution to the mass uncertainty is due to thickness variations. For the lighter ions, the second most important contribution to the mass uncertainty is due to channel digitization.

Table 2.6.5.1 -

RANGE 1 - Nominal Mass Resolution (R/L = 2)

Z	(pathlength variations) $\sigma_{M,L}$	(energy loss fluctuations) $\sigma_{M,\Delta E}$	(channel digitization) $\sigma_{M,\Delta E}$	(channel digitization) $\sigma_{M,E}$	(total) σ_M
2	0.010	0.060	0.052	0.025	0.099
6	0.030	0.126	0.028	0.014	0.133
12	0.065	0.186	0.020	0.010	0.198
26	0.211	0.384	0.019	0.008	0.439

RANGE 2 - Nominal Mass Resolution (R/L = 2)

Z	(pathlength variations) $\sigma_{M,L}$	(energy loss fluctuations) $\sigma_{M,\Delta E}$	(channel digitization) $\sigma_{M,\Delta E}$	(channel digitization) $\sigma_{M,E}$	(total) σ_M
2	0.010	0.073	0.067	0.023	0.102
6	0.029	0.117	0.036	0.013	0.126
12	0.060	0.166	0.025	0.009	0.178
26	0.167	0.290	0.020	0.007	0.335

RANGE 3 - Nominal Mass Resolution (R/L = 2)

| Z	(pathlength variations) $\sigma_{M,L}$	(energy loss fluctuations) $\sigma_{M,\Delta E}$	(channel digitization) $\sigma_{M,\Delta E}$	(channel digitization) $\sigma_{M,E}$	(total) σ_M
2	0.009	0.069	0.064	0.035	0.101
6	0.028	0.110	0.034	0.020	0.120
12	0.057	0.155	0.024	0.013	0.167
26	0.150	0.252	0.019	0.010	0.294

Chapter 3 - Data Analysis

3.1. Mass Measurement Overview

In the two parameter $\frac{dE}{dX} - E$ analysis technique of section 2.3, a single mass estimator was generated. For the purpose of making accurate isotope measurements, three and four parameter measurement techniques will be used. With three and four measurements of a particle's energy deposition history in the particle telescope, several mass estimators can be calculated and compared. With this type of redundancy, we can detect and remove sources of background events from the data set. Also, to reduce the mass measurement uncertainty, the measurements from several mass estimators can be used in a weighted mean mass estimator.

Figure 3.1.1a is a schematic diagram illustrating a three parameter RANGE 3 event. A particle has stopped in detector D3, depositing an energy E' and losing energies ΔE_1 and ΔE_2 in the two previous detectors. In this configuration there are actually three separate ways to form a two parameter mass estimator. The "ΔE detector" can be taken to be D1, or D2. Also, D1 and D2 can be treated together, as one detector. Only two of the mass estimators are independent; therefore, once the total energy $E = E' + \Delta E_1 + \Delta E_2$, is computed, there are only two parameters left in this system.

figure 3.1.1a - A schematic diagram of a three parameter event. ΔE_1, ΔE_2, and E' are the energies deposited by a particle slowing down in the indicated detectors.

figure 3.1.1b - A schematic diagram of a four parameter event.

(a)

(b)
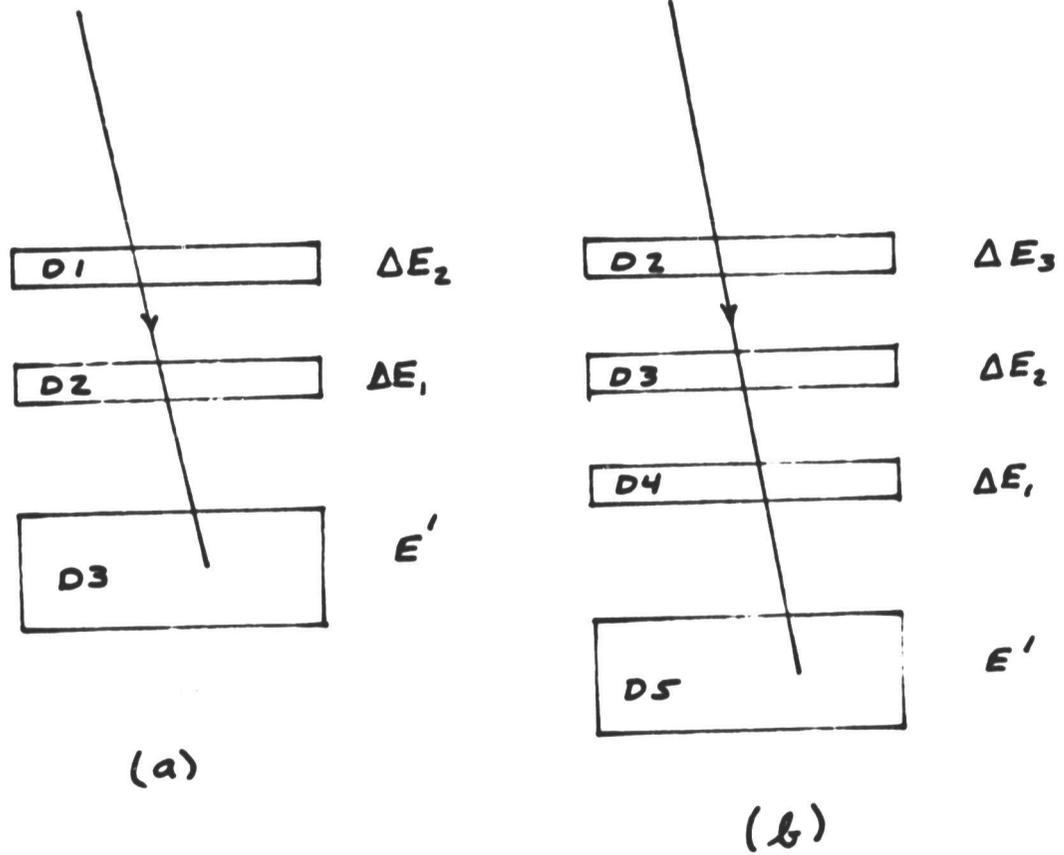
For this three parameter system, we will compute two mass estimators. The first estimator, called M_{23}, uses D2 as the "ΔE detector" and is found by solving

$$L = R(M_{23}, Z, \Delta E_1 + E') - R(M_{23}, Z, E') \quad . \tag{3.1.1}$$

The second, M_{13}, uses D1 as the "ΔE detector" and can be found by solving

$$L = R(M_{13}, Z, \Delta E_2 + \Delta E_1 + E') - R(M_{13}, Z, \Delta E_1 + E') \quad . \tag{3.1.2}$$

For the special case in which all of the mass uncertainty is caused by energy loss fluctuations, and in which the fluctuation in ΔE_2, $\delta(\Delta E_2)$, is small compared to ΔE_2, the mass estimators M_{23} and M_{13} are statistically independent. For the four parameter case illustrated in figure 3.1.1b we compute analogously M_{46}, M_{36} and M_{26}. To avoid confusion, detectors M1 and M2 are labeled as A and B, respectively. Thus the mass estimator that uses detector M1 as the ΔE detector and M2 as the stopping detector is called M_{AB}. For all RANGEs except RANGEs 0 and 1, three mass estimators are produced. For RANGE 1 we calculate the two mass estimators M_{B1} and M_{A1}, and for RANGE 0, we calculate M_{AB}.

In the following sections, we will describe the calibration of the mass estimators and then use mass vs. mass correlation plots to describe data selection and background reduction procedures.

3.2. Mass Estimator Calibration

In order to measure accurately a particle's mass by the two parameter $\frac{dE}{dX} - E$ technique, the range energy relation used in equation 2.3.1

$$L = R(M, Z, E) - R(M, Z, E') \tag{2.3.1}$$

must be known to sufficient accuracy. If $\delta(\Delta R)$ is the systematic error in $\Delta R = R(E) - R(E')$, then the systematic error in the mass estimator is

$$\frac{\delta M}{M} = \left[\frac{1}{\lambda - 1} \right] \frac{\delta(\Delta R)}{\Delta R} \quad . \tag{3.2.1}$$

Unfortunately, published tables of the range energy relations are insufficiently

accurate for our purposes and have systematic errors of the order of a few per cent. We need to know the location of each isotope track to ≤ 0.2 amu if track location errors are to make only a small contribution to the mass uncertainty. For ^{20}Ne this means that the systematic error in ΔR must be less than 0.75%.

One approach used by Vidor (1975) and Cook (1981) is to attempt to construct a new corrected range energy relation

$$R(M,Z,E) = R_0(M,Z,E) + R_{COR}(M,Z,E) \qquad (3.2.2)$$

where R_{COR} is a function of several unknown parameters $\{ a_i \}$ The values of the a_i are found by minimizing the distance, in some sense, between the experimental and theoretical isotope tracks.

The R_{COR} method needs enough experimental points to locate accurately the experimental isotope track in a sufficient number of energy bins in each RANGE. If 20 particles are sufficient to locate the isotope track in each of 25 energy bins per RANGE, then one needs about 500 particles per RANGE to calibrate an element. Unfortunately, for the set of HIST flight data, the only elements with charge $Z > 3$, in RANGEs 0-4, for which there is an an amount of data approaching the above amounts, are carbon and oxygen.

A factor that limits the accuracy of the R_{COR} function is the possibility of small systematic errors in the energy calibration or in the thickness maps. Since the energy ranges for all the possible mass estimators M_{ij} overlap, attempting to fit one R_{COR} relation to the data for several mass estimators may not be completely successful.

Oxygen data from RANGEs 0 to 3 and mass estimators M_{A0}, M_{A1}, M_{A2}, M_{A3}, M_{B1}, M_{B2}, M_{B3}, M_{12}, M_{13} and M_{23} were used in an attempt to find one unique R_{COR} to represent the oxygen data. A 16 point R_{COR} function and the thicknesses of detectors M1, M2, D1, D2 and D3 were the parameters to be fit to the data. The resulting R_{COR} function was then used to recompute all the mass estimators.

Deviations of up to 0.5 amu from the correct ^{16}O mass were found. For ^{12}C there was a similar result. Thus a correction scheme was developed to correct each mass estimator, separately.

In each RANGE the preliminary mass estimator was plotted vs. E1, the energy in the stopping detector. Figure 3.2.1 shows an example of this type of plot, for helium in RANGE 0. The approximate form of M_y vs. E1 for the principal isotope of an element was then fit by hand to the plot by a series of line segments. This approximate form of the preliminary mass estimator, $g(E1)$, was then used to correct the mass estimator of each particle with the equation

$$M_y \text{ (corrected)} = M_y \text{ (preliminary)} \frac{M_o}{g(E1)} . \qquad (3.2.3)$$

where M_o is the mass in amu of the principal isotope.

The advantage of this procedure was that it was quick and easy to implement on a small computer system. One disadvantage is that the procedure is not functionally exact. If the range energy relation is a function of E/M, and g/M_o varies slowly with E1, then $M_y(\text{corrected})$ is equal to M_o plus terms of order $(g/M_o)^2$. Another "disadvantage" of the procedure might be the practice of doing the fits to mass vs. E1 by hand. A difficulty is that you do not get any information about the "goodness of fit" or errors in the fit parameters. In practice the hand process is quicker, much less confused by noise and background and gives quite acceptable accuracy. The maximum error in this track location procedure is about 0.2 amu.

figure 3.2.1 - M_{AB} vs. E1 for RANGE 0 helium data. The solid line is the hand
fit, $g(E1)$, used to correct the preliminary mass estimator, using equation
3.2.3.
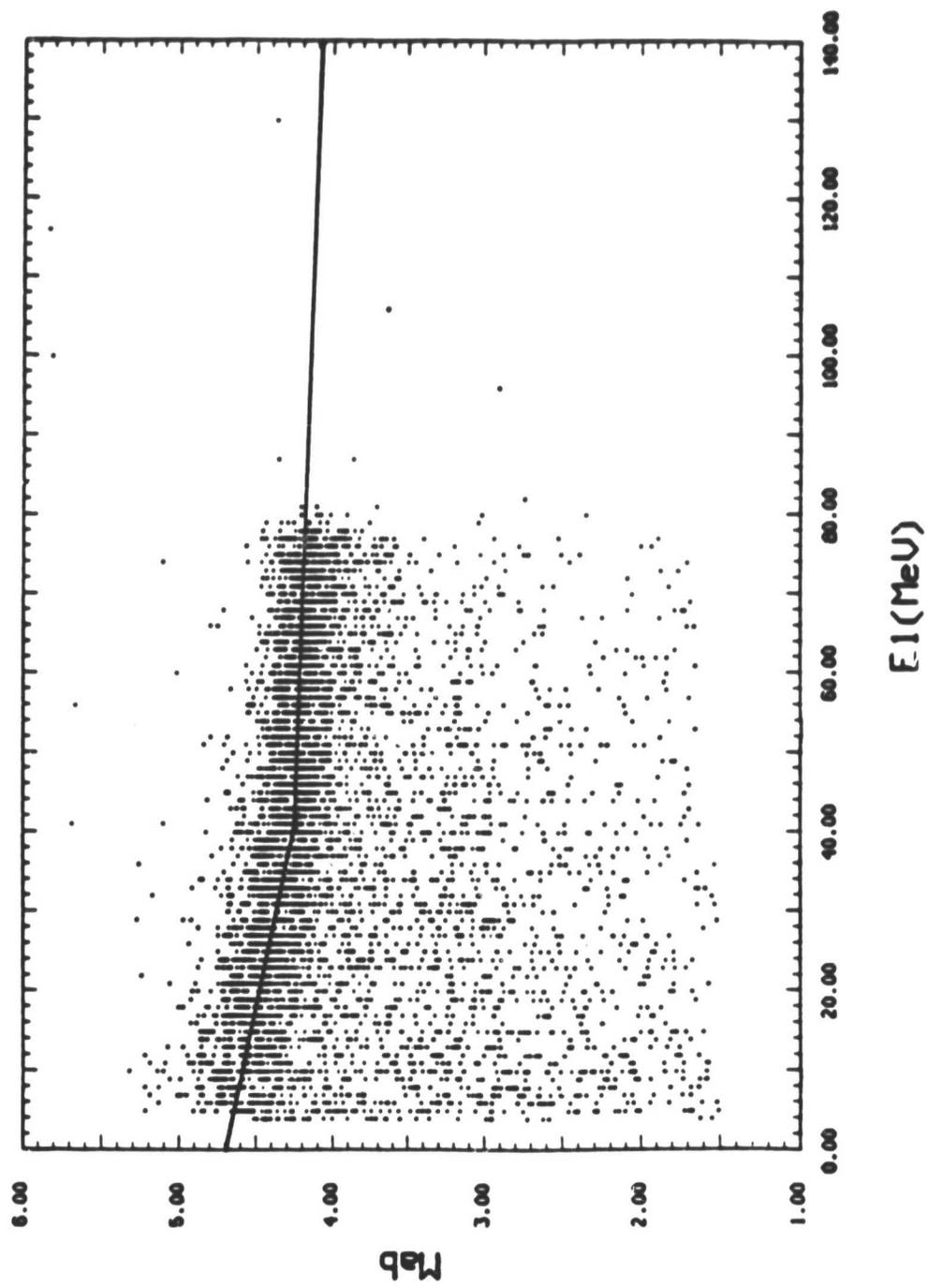
3.3. High Resolution Data Set Selection

To measure isotope abundances, a high resolution data set was prepared. We will describe selection process for that high resolution data set. Restrictions on the hodoscope state, energy deposited in D1, radial position in certain detectors, and mass estimator consistency, will be described.

3.3.1. Hodoscope Requirements

To compute a mass estimator, the pathlength of the particle in the ΔE detector must be calculated. The basic requirement is that the hodoscope information specify a unique particle trajectory through the telescope. Thus, we must have only one group of triggered strips per matrix detector plane, or the MH condition must be false. The MH events were rejected, as were event records in which over two strips per group were triggered. The fraction of event records with the MH condition was as large as 1/4 of the total number of events, at times of high particle counting rates. Most of the MH events were thought to be caused by accidental coincidences at times of high singles rates, as detailed in Spalding (1983). Records with over two strips per group were an insignificant part ($\leq 1\%$) of the data.

The remaining event records were divided into two groups, event records in which only one matrix detector strip triggered per hodoscope plane, and event records in which one or more planes had two adjacent triggered strips. If hodoscope information were all that was required from detectors M1 and M2, since the particle had stopped deep in the detector stack, then both classes of events were accepted. Because the particle had to penetrate the detector right between the strips, we think that the double strip groups may have even located the particle better in the hodoscope, thereby reducing the position uncertainty, although this idea has not been put to a conclusive test.

The significance of the double strip condition lies in what it tells us about the measurement of the energy deposited in a matrix detector. Suppose that a particle has triggered two adjacent strips on one plane of a matrix detector. Then there is a large probability that a "signal defect" in that matrix detector has occurred. The energy measured by HIST in that matrix detector will be less than the energy actually lost by the particle slowing down in that matrix detector. There is also a population of events that have energy measurements characteristic of the "signal defect" condition, and have only single strips triggered.

The "signal defect" behavior can be illustrated with a mass vs. mass correlation plot. Figure 3.3.1.1 shows M_{B1} plotted vs. M_{A1} for carbon with the single strip hodoscope requirement. On this plot, if there was no signal defect mechanism, about 99% of the data should be in a clump at the point (12,12) and 1% at the point (13,13). The clump at (12,12) has a horizontal streamer of particles with $M_{B1} \sim 12$ and M_{A1} with some arbitrary lower value. This is caused by a signal defect in the matrix detector M1, used as ΔE detector for M_{A1}, and not considered for M_{B1}. The slanted streamer falling from (12,12) is caused by a signal defect in the matrix detector M2. M2 is used as the ΔE detector for M_{B1}, and as part of the E' detector, together with detector D1, for M_{A1}. The streamer then slants because the M2 signal defects introduce correlated errors into M_{B1} and M_{A1}.

In figure 3.3.1.2 and 3.3.1.3, we plot carbon RANGE 1 events in which double strip events are required in the "y plane" of detectors M1 and M2, respectively. The double strip requirements have greatly increased the signal defect probability. Figures 3.3.1.4a-b are histograms of M_{A1} and M_{B1} with a single strip hodoscope requirement. Figures 3.3.1.5a-b are histograms of M_{A1} and M_{B1} with a double strip requirement in the "y planes" of matrix detectors M1 and M2,

respectively. The mass resolution for the double strip events is so bad that we must discard them from the high resolution data set. Table 3.3.1.1 shows the fraction of HIZ events in the time period 266:10 to 272:00 in RANGEs 0 through 4 for each of four coincidence equations. M2d and M1d refer to the double strip condition in detectors M2 and M1 respectively. In parentheses is the ratio of the number of carbon events for the coincidence equation to the number of carbon events in that RANGE.

Table 3.3.1.1 -

Carbon Double Strip Events

RANGE	$(M2d) \cdot (M1d)$	$(M2d) \cdot (\overline{M1d})$	$(\overline{M2d}) \cdot (M1d)$	$(\overline{M2d}) \cdot (\overline{M1d})$
1	130 (.050)	665 (.256)	355 (.136)	1581 (.608)
2	42 (.027)	252 (.164)	184 (.120)	1061 (.689)
3	21 (.017)	179 (.147)	146 (.120)	868 (.715)
4	1 (.004)	28 (.111)	24 (.095)	199 (.790)

In appendix A we find that the probability of a double strip event in a matrix detector is a function of the energy deposited in that matrix detector. For the ions analyzed in this report, the probability of a double strip increases with the amount of energy deposited in the matrix detector. This effect can be observed in table 3.3.1.1. The carbon ions that stop in RANGE 1 are going slower as they penetrate detectors M1 or M2 than carbon ions that stop in RANGES 2-4, and thus deposit more energy in detectors M1 or M2. The RANGE 1 events then have a higher fraction of double strip events than the RANGE 2-4 events.

We can obtain some insight into the double strip events by considering briefly charge collection in a "normal" (continuous electrode) solid state detector of the same nominal thickness and applied voltage as the matrix detector M1. With an applied voltage of 25 volts, electrons would take about 1.3 nsec, and holes about 2.5 nsec, to cross 50 μ of silicon. The time constant of the preamps is about 2 μ sec, so that in a normal detector, all the charge would be collected. In a matrix detector, the strong association of a large signal loss with the two strip events suggests that something happens to the charge collection procedure in the gap between the two strips. The electric field configuration in the gaps might cause some fraction of the electrons and holes to be directed to regions of low field strength. There the electrons and holes may either recombine or travel to the strip electrodes so slowly that the signal is reduced, because part of it is effectively filtered out by the preamp time constant.

figure 3.3.1.1 - M_{B1} vs. M_{A1} for carbon data. The hodoscope triggers are restricted to single strip events.
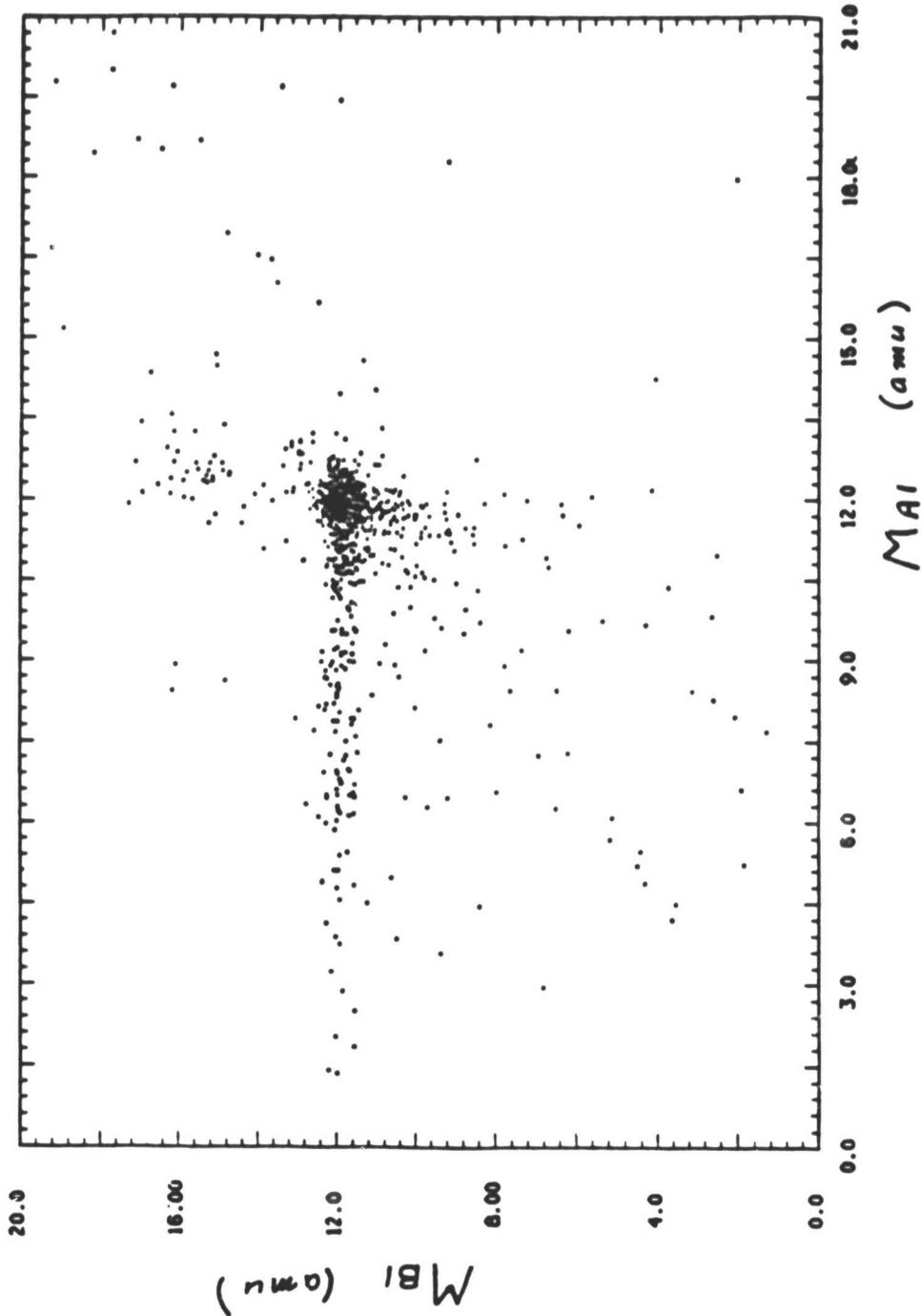
figure 3.3.1.2 - M_{B1} vs. M_{A1} for carbon data. The hodoscope triggers are
restricted to events with double strip triggers in the "y plane" of M1, and
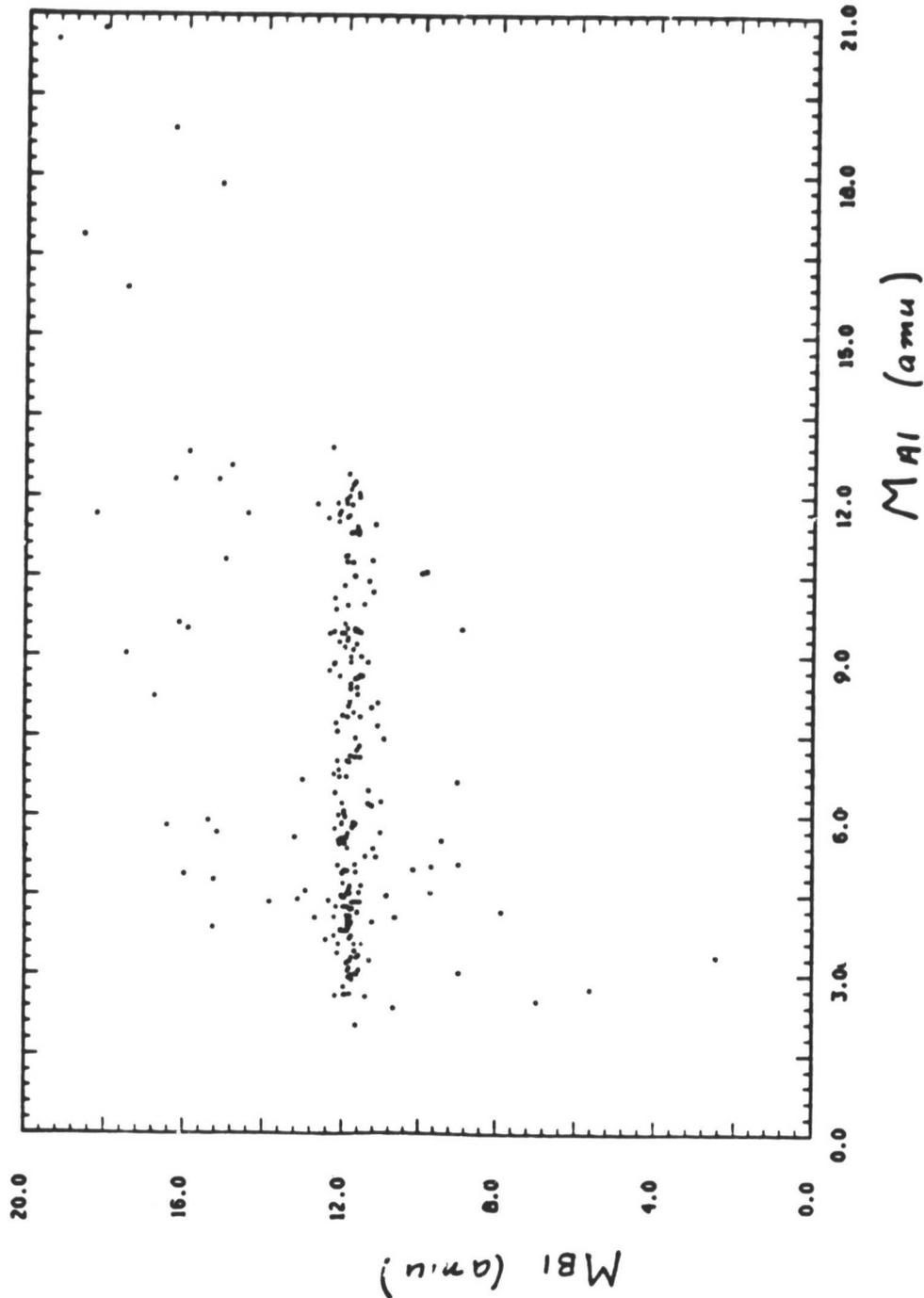single strip triggers in the remaining matrix detector planes.

figure 3.3.1.3 - M_{B1} vs. M_{A1} for carbon data. The hodoscope triggers are restricted to events with double strip triggers in the "y plane" of M2, and single strip triggers in the remaining matrix detector planes. The streamer of events around $M_{A1} \approx 18-21$ and $M_{B1} \approx 8-20$ is due to nitrogen events which have had their mass estimators calculated with Z=6 instead of Z=7.
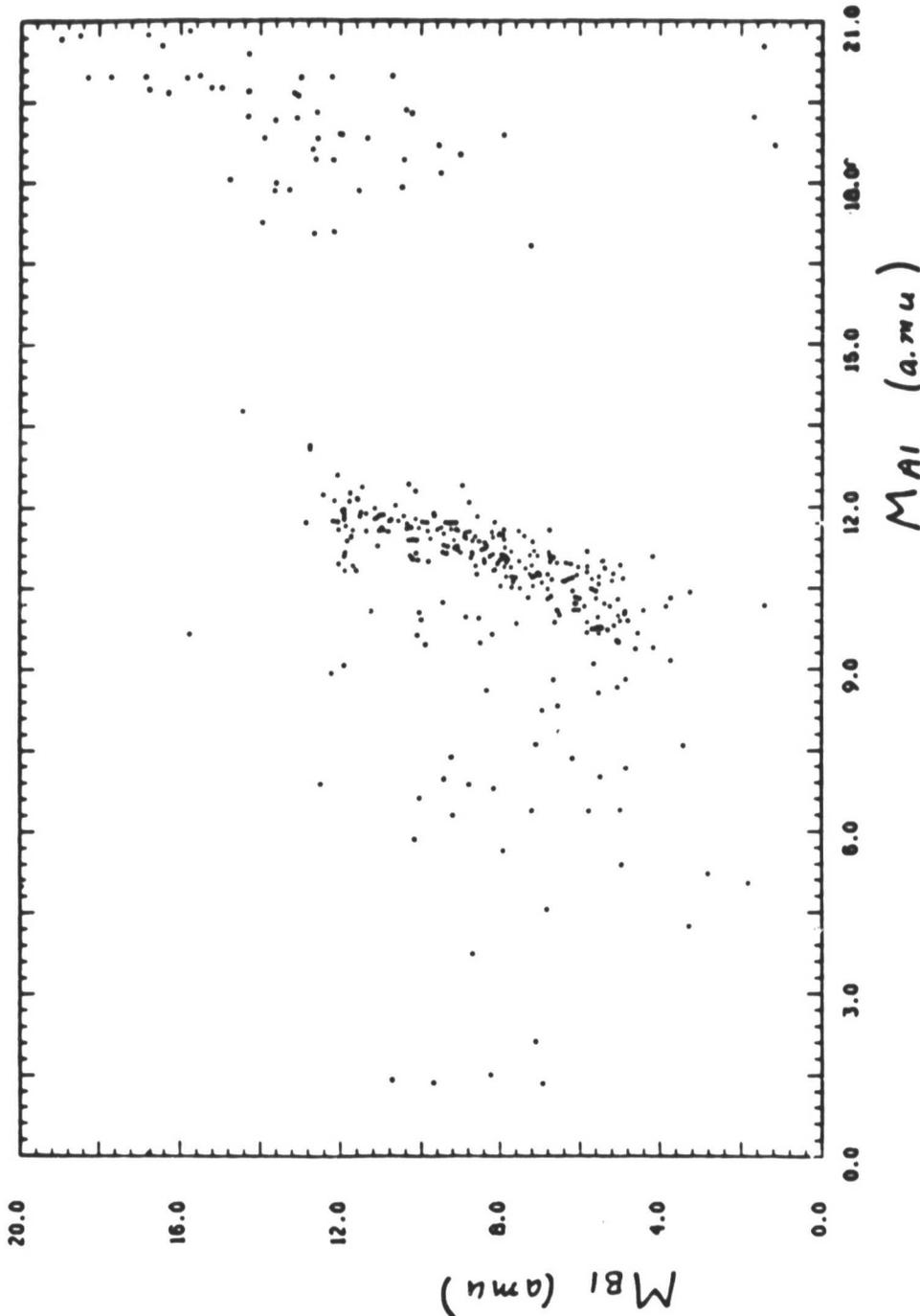
figure 3.3.1.4a-b - Mass histograms of carbon RANGE 1 events with single strip triggers. Figure 3.3.4a shows M_{A1} and figure 3 3.4b shows M_{B1}.
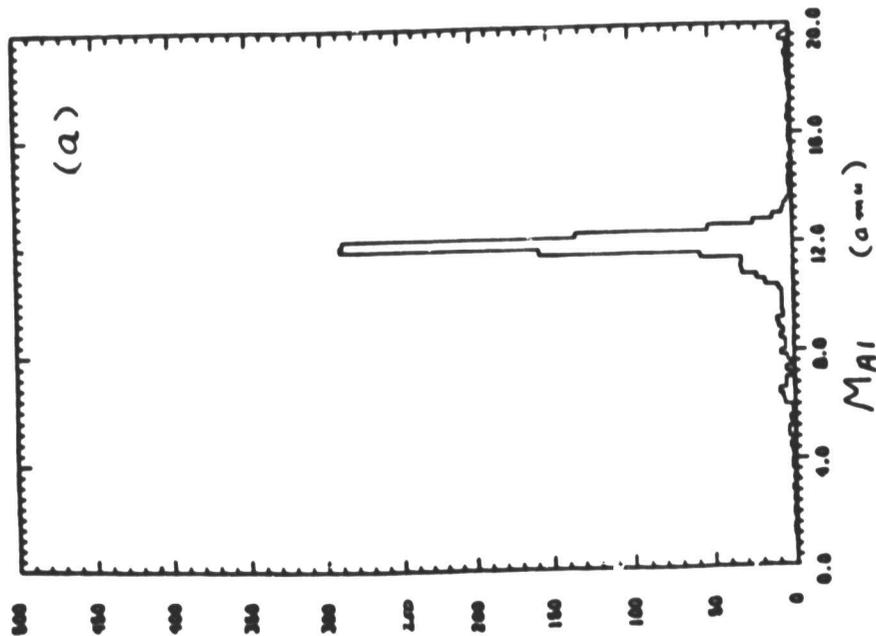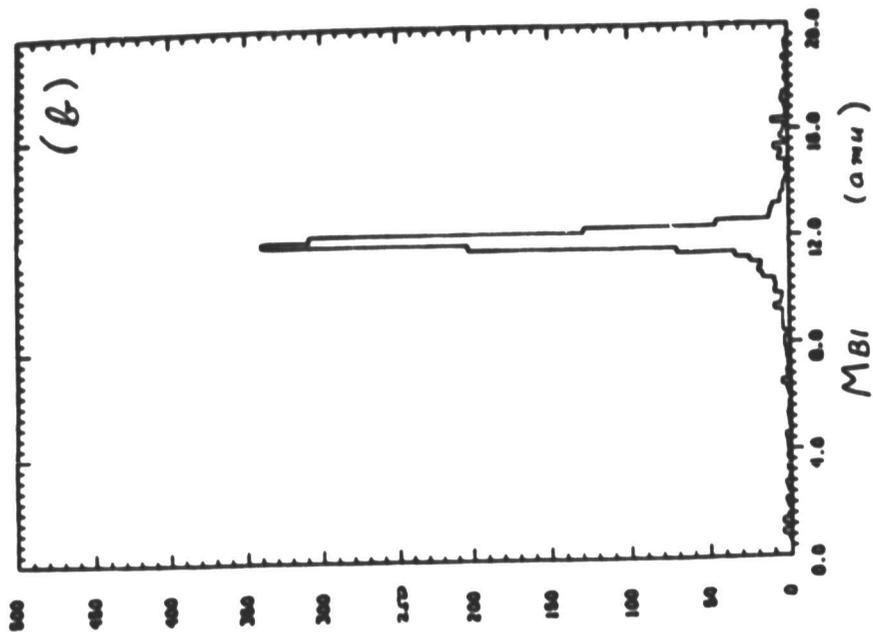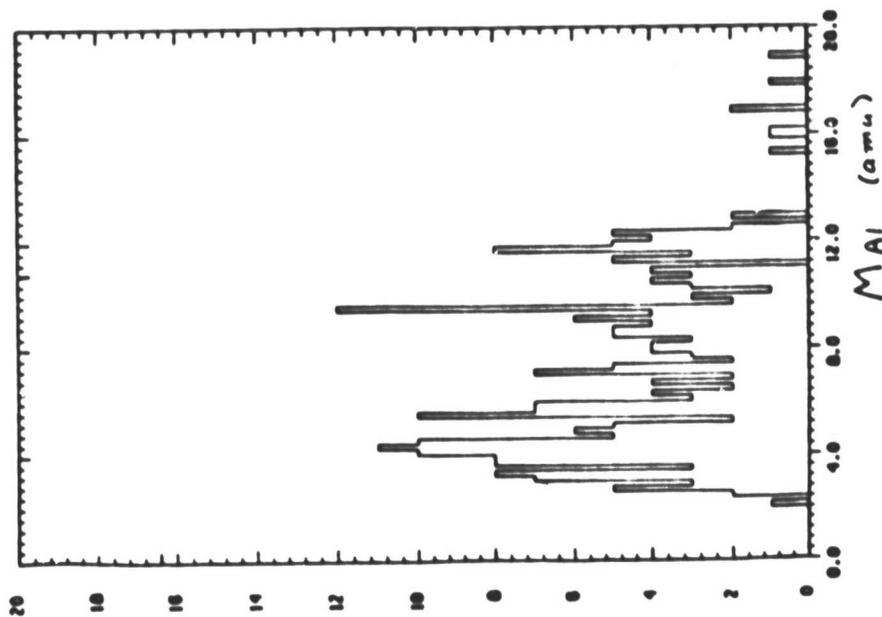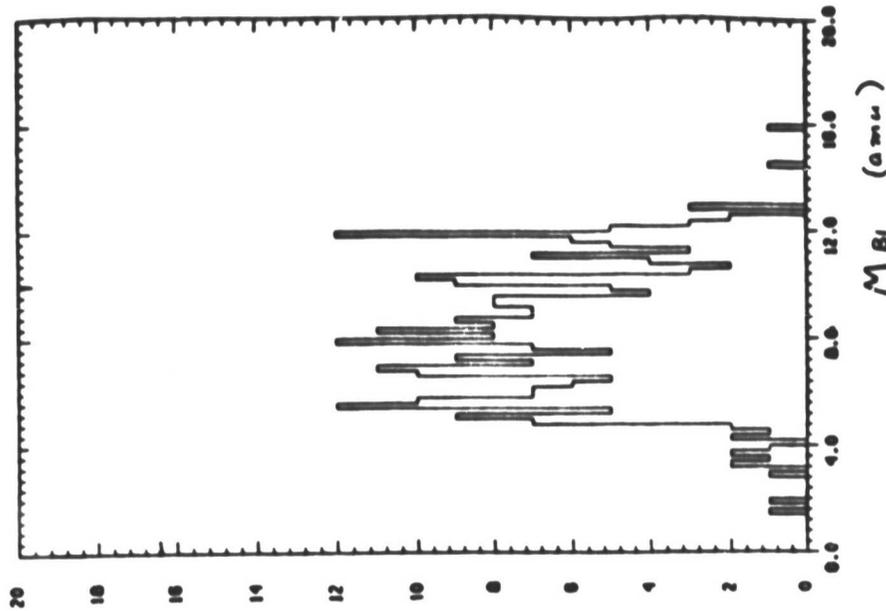
figure 3.3.1.5a-b - Mass histograms of carbon RANGE 1 events. Events in figure 3.3.5a have double strip hodoscope triggers in detector M1's "y plane" and single strip triggers in the remaining detector planes. Events in figure 3.3.5b have double strip hodoscope triggers in detector M2's "y plane" and single strip triggers in the remaining detector planes.

3.3.2. Radius Requirements

The particle trajectory in the hodoscope is extrapolated to all the detectors that the particle hits. In two detectors, the radial distances from the center of the detectors to the positions where the extrapolated trajectories intersect the detectors, were computed. D1, the smallest detector exclusive of the matrix detectors, and the next detector deeper in the stack beyond the stopping detector, D(R+1), were chosen. Particles that had an impact point near the edge of a detector were more likely to show a signal defect than others nearer the center of the detector. For the high resolution data set we set maximum radii in the two detectors based on the behavior of the mass estimator near the detector edge.

Figure 3.3.2.1 shows the weighted mean of the RANGE 1 oxygen mass estimators plotted vs. radius in D1. At the largest radii one can see a systematic underestimate of the mass caused by the signal defect at the detector edge. For D1, a maximum radius of 13.8 mm was set. The oxygen mass estimator weighted sum was plotted vs. radius in D2 in figure 3.3.2.2. Again there is a systematic mass underestimate and a maximum radius of 15.0 mm was set here. For RANGEs 2-4 no maximum radius was set in detector D(R+1). For the helium data set more restrictive radius restrictions were needed, because the rare isotope ^{3}He lay below the more abundant isotope ^{4}He. Correlated mass errors produced by signal defects at the detector edge might then masquerade as ^{3}He events. Table 3.3.2.1 lists the radial restrictions for helium and elements with charge $Z \geq 6$ for the high resolution data set.

Table 3.3.2.1 -

Maximum Radii (mm)

RANGE	$Z \geq 6$		Helium	
	Radius D1	Radius D(R+1)	Radius D1	Radius D(R+1)
1	13.8	15.0	13.8	12.90
2	13.8	none	13.8	16.75
3	13.8	none	13.8	16.75
4	13.8	none	13.8	none
5	13.8	none	13.8	none

figure 3.3.2.1 - The RANGE 1 oxygen weighted sum mass estimator is plotted vs. the radius in detector D1. The maximum D1 radius chosen for the high resolution data set is shown as a dashed line.
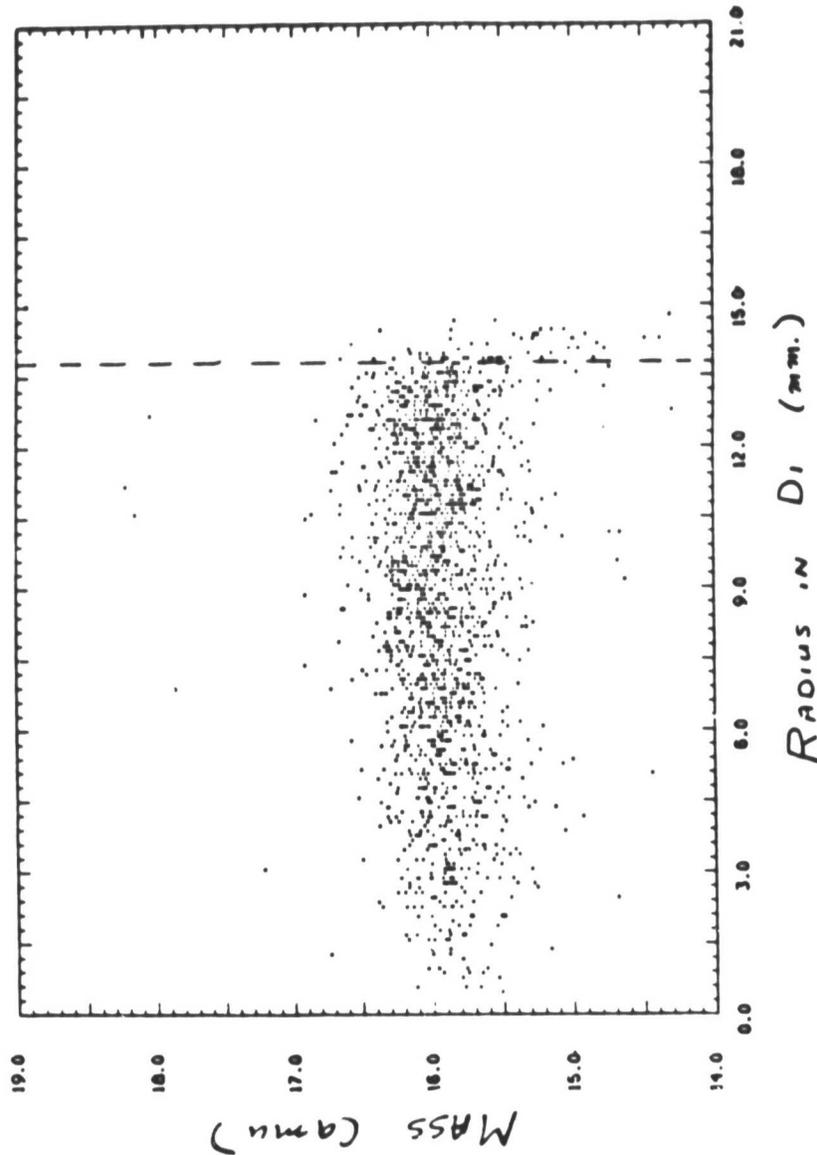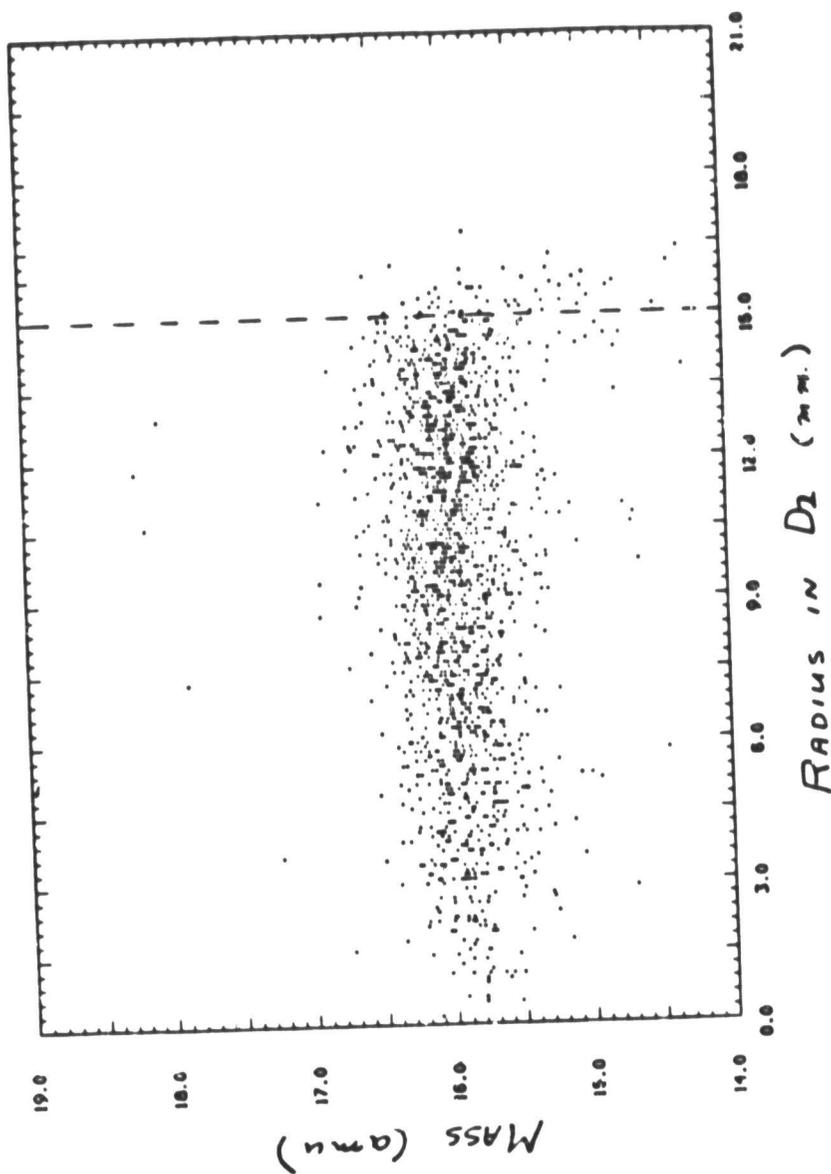
figure 3.3.2.2 - The RANGE 1 oxygen weighted sum mass estimator is plotted vs. the radius in detector D2. The maximum D2 radius chosen for the high resolution data set is shown as a dashed line.

3.3.3. Energy Limits

In four instances particles were required to pass a requirement on $E1$, the energy deposited in the stopping detector. For RANGE 1 carbon events we felt that the ^{12}C track position for $E1 < 7MeV$ was not known sufficiently well, so RANGE 1 carbon events had to have $E1 \geq 7MeV$ to be included in the high resolution data set. Thus we eliminated about 12% of the RANGE 1 carbon data.

For RANGE 1 neon events, M_{B1} vs. M_{A1} cross plots were prepared for five E1 energy intervals of width 28 MeV. In the lowest energy interval, the mass resolution was much worse than in the other four energy intervals; so therefore neon RANGE 1 events were required to have $E1 \geq 28MeV$. Thus we eliminated about 23% of the RANGE 1 neon data. For nitrogen in RANGE 1, the mass resolution for $E1 < 30MeV$ appeared worse than for $E1 \geq 30MeV$. Nitrogen events in RANGE 1 were required to have $E1 \geq 30MeV$, thus eliminating about 40% of the RANGE 1 data.

In RANGE 4, particles that have completely penetrated detector D4 encounter two "dead layers" which have a total thickness of approximately 100 microns of silicon, at the rear of D4 and at the front of D5. In these dead layers, charge is not collected, thus causing a signal loss that systematically lowers the mass estimators. A signal loss in the stopping detector would cause a correlated mass underestimate in both M_{34} and M_{24}, that would interfere with the ^3He measurement. A particle of a given mass that stops in the dead layer of D4 has the same energy measurements in the E' and ΔE detectors, D3 and D4, as a lighter particle that stops in D4, but in front of the dead layer. Thus, the mass measurement is ambiguous near the "end of range" position in D4. Only for helium is there a significant population of solar flare events in this RANGE 4 "end of range" position ($\approx$ 50 out of 207 range 4 events). We therefore chose a requirement $E1 < 50 MeV$, for RANGE 4 helium events, which removes the region

of dead layer mass ambiguity.

3.3.4. Mass Consistency Requirements

Because of the presence of occasional large errors in the mass estimators, which would bias the weighted mass estimator, data included in the high resolution data set had to pass consistency requirements on the mass estimators. For elements C, N, O, Ne, and Mg, we chose as a mass consistency estimator the ratio of two mass estimators. For the three parameter systems the ratio chosen was

$$R_1 = \frac{M_{j-1,j}}{M_{j-2,j}} \quad . \tag{3.3.4.1}$$

where j is the detector number. For RANGE 2, $R_1 = \frac{M_{12}}{M_{B2}}$. For a four parameter system, R_1 is the same as above and R_2 was defined as

$$R_2 = \frac{M_{j-1,j}}{M_{j-3,j}} \quad . \tag{3.3.4.2}$$

For RANGE 3, $R_2 = \frac{M_{23}}{M_{B3}}$.

The distribution of R_1 and R_2 is approximately Gaussian. For each RANGE and element the entire HIST data set was used to form histograms for R_1 and R_2. The histograms were then fit to determine the location and width of the peaks in R_1 and R_2. Figure 3.3.4.1 shows a histogram of R_1 for RANGE 1 oxygen events. For C, O, and Mg, mass consistency ratio requirements were set, which were symmetric about $R_j = 1.0$, and approximately included the central two standard deviations, $2 \chi_{od}$, of the ratio peak. For N, the ratio limits were set exactly at the fit peak location, plus and minus two standard deviations of the ratio peak. With Ne, the same procedure was followed but the requirements were relaxed to plus and minus 2.5 χ_{od}, because we wished to include as many Ne as possible, in order to reduce statistical uncertainties in the $^{22}Ne/^{20}Ne$ abundance ratio.

The RANGE 3 neon consistency requirements were widened to accept all of the RANGE 3 neon data except for very large mass disagreements. Figures 3.3.4.2a-b show RANGE 1 and RANGE 3 neon mass cross plots with the consistency requirements drawn in. Other exceptions are the RANGE 1 C, N, and O consistency requirements, which are about plus and minus 1.5 X_{σ}. In RANGE 1 the background problems were more severe than in the other RANGEs and the C, N, and O measurements were for isotopes at or less than the 1% level of the more abundant isotopes. Thus we chose a more restrictive consistency requirement, selecting on the ratio histogram only the central Gaussian peak and excluding most of the tails of the ratio distribution. Table 3.3.4.1 contains the mass consistency requirements chosen for the elements C, N, O, Ne and Mg.

figure 3.3.4.1 - A histogram of the mass consistency estimator,
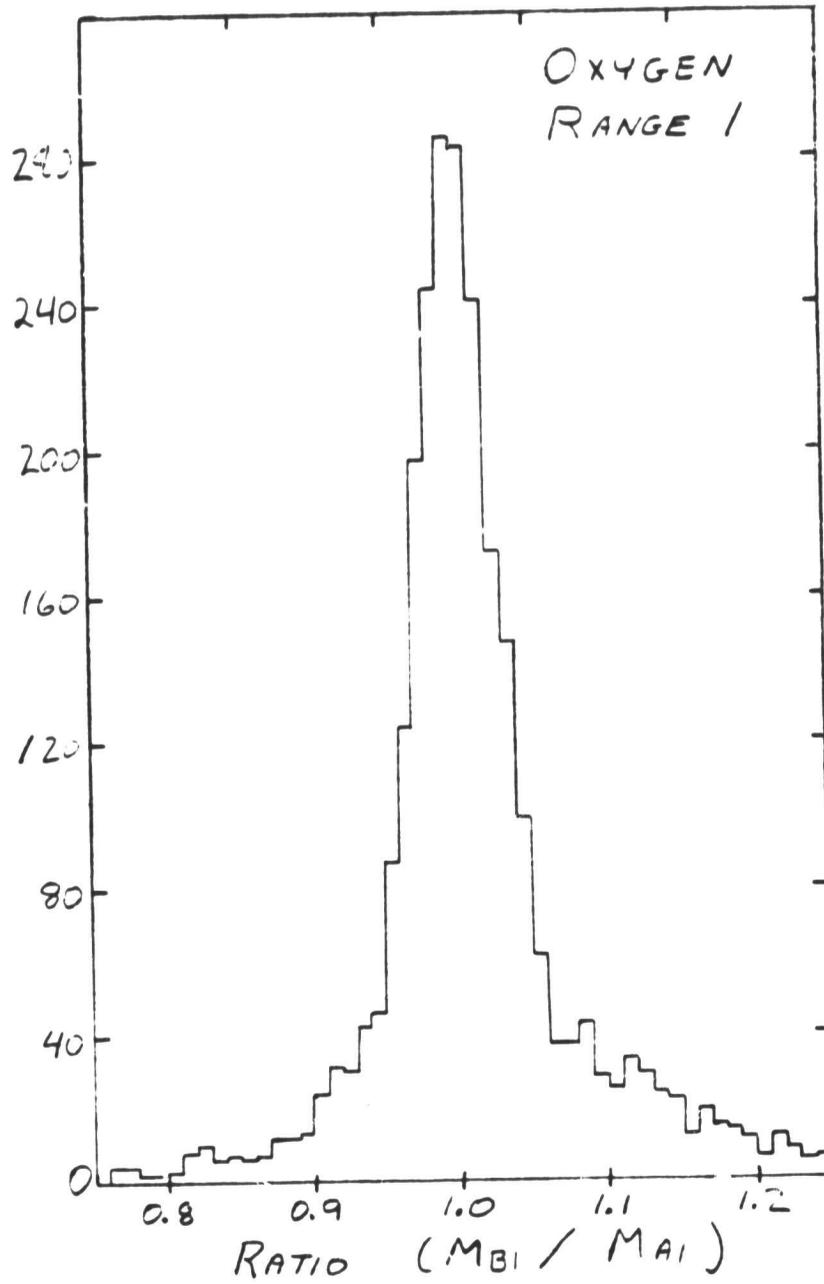$R_1 = M_{B1}/M_{A1}$, for RANGE 1 oxygen data.

figure 3.3.4.2a - A plot of M_{B1} vs. M_{A1} for neon RANGE 1 events, in the time period 78:266:10 to 78:272:00. The mass consistency requirements are shown as dashed lines.
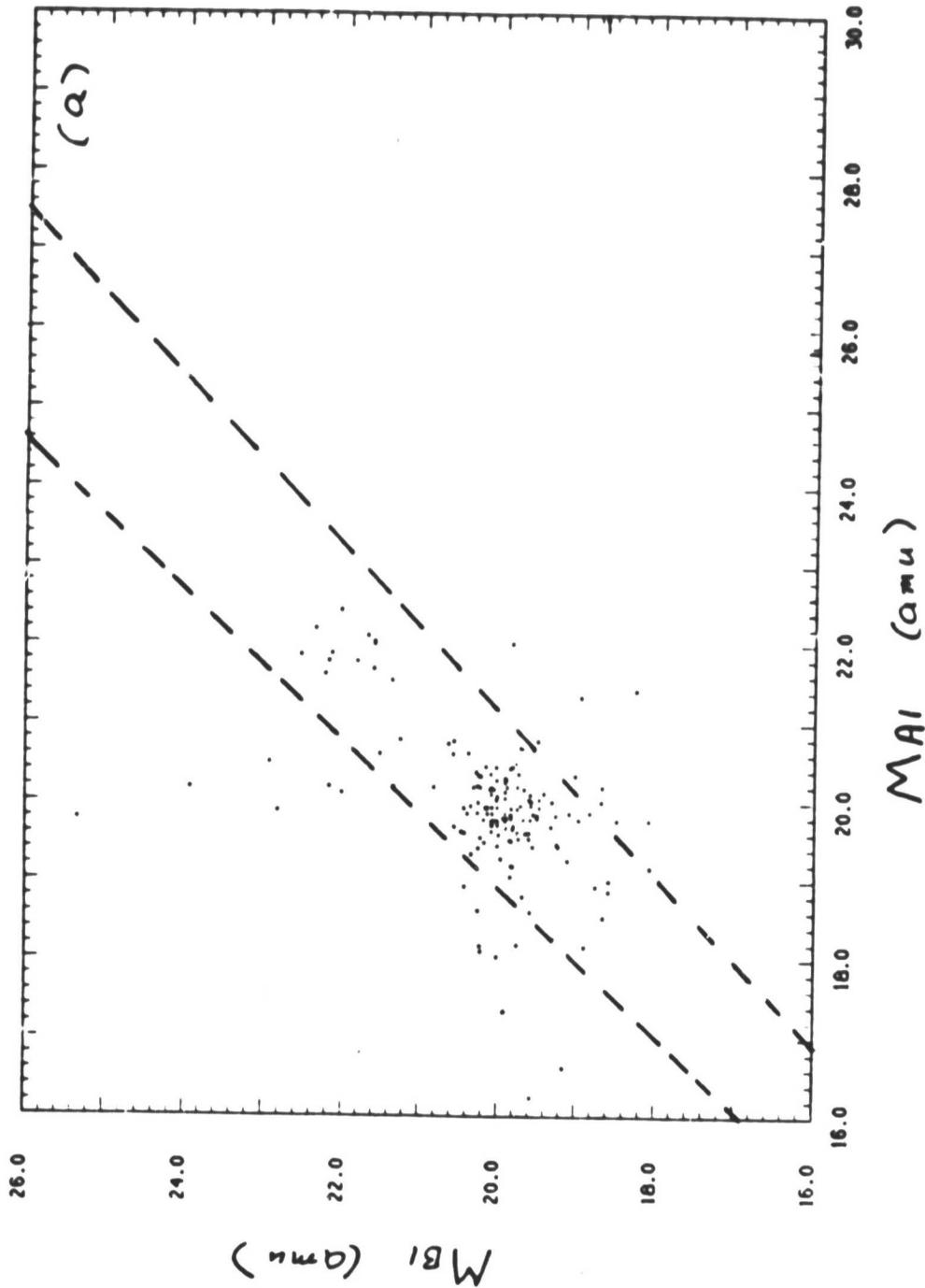
figure 3.3.4.2b - A plot of M_{23} vs. M_{13} for neon RANGE 3 events, in the time period 78:266:10 to 78:272:00. The mass consistency requirements are shown as dashed lines.
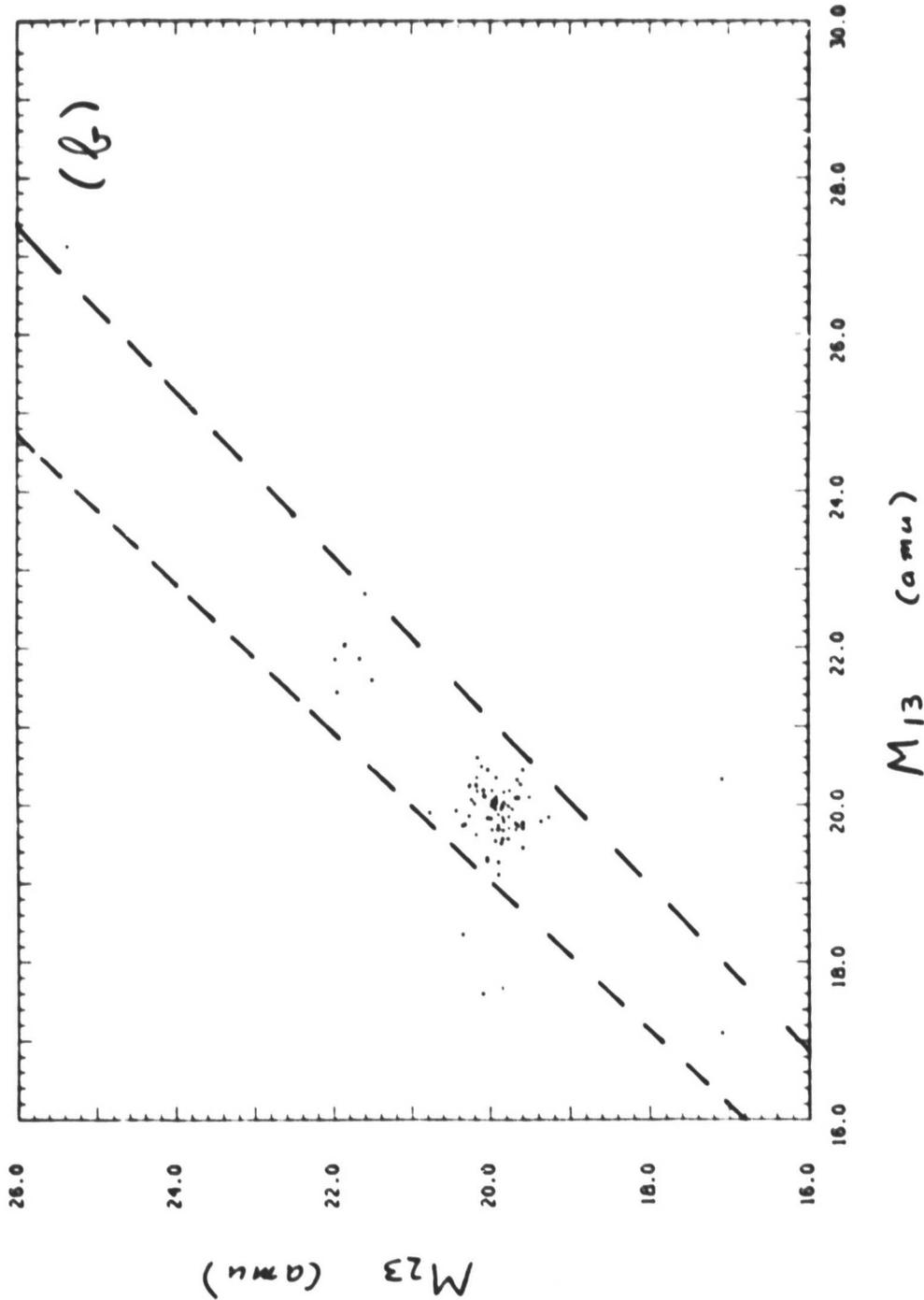
Table 3.3.4.1 -

Mass Ratio Requirements

Element	RANGE	Ratio	Limits	χ_{ed}
carbon	1	M_{B1}/M_{A1}	1.0 ± 0.050	1.4
	2	M_{12}/M_{B2}	1.0 ± 0.070	2.1
	2	M_{12}/M_{A2}	1.0 ± 0.075	2.0
	3	M_{23}/M_{13}	1.0 ± 0.060	2.0
	3	M_{23}/M_{B3}	1.0 ± 0.065	2.0
	4	M_{34}/M_{24}	1.0 ± 0.050	1.9
	4	M_{34}/M_{14}	1.0 ± 0.070	2.1
nitrogen	1	M_{B1}/M_{A1}	1.000 ± 0.052	1.5
	2	M_{12}/M_{B2}	1.000 ± 0.053	2.0
	2	M_{12}/M_{A2}	1.008 ± 0.067	2.0
	3	M_{23}/M_{13}	0.998 ± 0.044	2.0
	3	M_{23}/M_{B3}	0.994 ± 0.055	2.0
	4	M_{34}/M_{24}	1.006 ± 0.047	2.0
	4	M_{34}/M_{14}	0.995 ± 0.058	2.0
oxygen	1	M_{B1}/M_{A1}	1.0 ± 0.050	1.4
	2	M_{12}/M_{B2}	1.0 ± 0.065	2.1
	2	M_{12}/M_{A2}	1.0 ± 0.070	2.0
	3	M_{23}/M_{13}	1.0 ± 0.060	2.1
	3	M_{23}/M_{B3}	1.0 ± 0.065	2.0
	4	M_{34}/M_{24}	1.0 ± 0.050	2.0
	4	M_{34}/M_{14}	1.0 ± 0.050	2.0
neon	1	M_{B1}/M_{A1}	1.000 ± 0.055	2.5
	2	M_{12}/M_{B2}	1.000 ± 0.049	2.5
	2	M_{23}/M_{B3}	1.007 ± 0.064	2.5
	3	M_{23}/M	1.000 ± 0.051	3.0
	4	M_{34}/M_{24}	1.000 ± 0.062	2.5
magnesium	2	M_{12}/M_{B2}	1.0 ± 0.04	1.8
	2	M_{12}/M_{A2}	1.0 ± 0.05	2.3
	3	M_{23}/M_{13}	1.0 ± 0.04	1.9
	3	M_{23}/M_{B3}	1.0 ± 0.05	2.1
	4	M_{34}/M_{24}	1.0 ± 0.04	1.7

The choice of a mass consistency requirement based on mass ratios implies that σ_M is proportional to M for different isotopes of the same charge. We would expect such a result if most of the contribution to σ_M came from uncertainties in the detector thickness, or in the isotope track location. On the other hand, if most of the contribution to σ_M came from other sources, such as energy measurement uncertainties, or energy loss fluctuations, then σ_M would be more nearly constant. For C, N, O, Ne, and Mg, the variation in M is not sufficient to test the behavior of σ_M.

For helium, there are sufficient events to check the scaling of σ_M experimentally. The time intervals 296:09 to 297:09 and 307:00 to 308:00 contain two ^{3}He rich flares. RANGEs 1 and 2 have enough events to measure σ_M for both ^{3}He and ^{4}He, separately (see figure 3.4.9). Table 3.3.4.2 contains σ_M for that time period as a function of RANGE and isotope. For helium, in this case, the data are consistent with the hypothesis that σ_M is independent of M.

Table 3.3.4.2 -

Helium Mass Resolution

Mass	$\sigma_M(^3He)$	$\sigma_M(^4He)$
M_{B1}	0.118 ± 0.018	0.162 ± 0.020
M_{A1}	0.238 ± 0.037	0.228 ± 0.029
M_{12}	0.138 ± 0.031	0.137 ± 0.020
M_{B2}	0.170 ± 0.040	0.182 ± 0.028

We chose a consistency statistic for helium that was different than for elements with charges $Z \geq 6$. All of the helium measurements were made with the three parameter analysis method. We therefore chose the difference of the two mass estimators,

$$M_{diff} = M_{j-1, j} - M_{j-2, j} \quad . \tag{3.3.4.3}$$

where j is the detector number, as a consistency estimator. For the entire HIST helium data set, histograms of M_{diff} were accumulated for each RANGE, and fit to determine the M_{diff} peak location and width. Helium events were accepted

into the high resolution data set if M_{eff} for each event was less than two standard deviations from the peak location. The limits adopted are listed in table 3.3.4.3.

Table 3.3.4.3 -

Helium M_{eff} Requirements

RANGE	Limits(amu)
1	-0.027 ± 0.504
2	-0.005 ± 0.446
3	0.023 ± 0.440
4	-0.001 ± 0.454
5	-0.014 ± 0.384

3.3.5. Mass Resolution

Events that passed the selection criterion of section 3.3.1-4 were summed into a histogram for each mass estimator. The histograms were fit using Gaussian peak shapes, and the peak location and σ_M were determined for each mass estimator. For each RANGE a weighted sum of the mass estimators was formed, using for weights $(\sigma_M)^{-2}$, as determined in the fits of the individual mass estimators. Table 3.3.5.1 lists the mass resolution obtained by element and RANGE, where W_j is the weighted sum for RANGE j.

The mass resolution that we measured for the HIST flight data is significantly larger than the nominal resolution calculated in chapter 2, table 2.6.5.1. Let us compare the measurements of σ_M for M_{B1}, M_{12}, and M_{23} to the calculations of σ_M for R/L = 2 and RANGEs 1-3 in table 2.6.5.1. The experimental measurement of σ_M for helium is 35% to 50% larger, σ_M for carbon is about 65% larger, and σ_M for magnesium is 40% to 75% larger, than was calculated. The reasons for this discrepancy are not known at present. However, the precision of the main results of this work, involving the abundances of isotopes ^{3}He, ^{13}C, ^{22}Ne, ^{25}Mg, and ^{26}Mg, is mainly limited by the statistical fluctuations in the number of particles observed in the 78.266 solar flare.

Table 3.3.5.1 -

HIST Mass Resolution

Mass	Helium	Carbon	Nitrogen
M_{A1}	0.152 ± 0.003	0.225 ± 0.006	0.216 ± 0.017
M_{B1}	0.169 ± 0.002	0.228 ± 0.007	0.277 ± 0.025
W_1	0.127 ± 0.002	0.194 ± 0.006	0.191 ± 0.017
M_{12}	0.136 ± 0.003	0.203 ± 0.006	0.206 ± 0.018
M_{B2}	0.170 ± 0.003	0.256 ± 0.008	0.211 ± 0.018
M_{A2}	---	0.253 ± 0.009	0.272 ± 0.028
W_2	0.122 ± 0.002	0.159 ± 0.006	0.162 ± 0.013
M_{23}	0.139 ± 0.003	0.191 ± 0.007	0.185 ± 0.018
M_{13}	0.173 ± 0.003	0.208 ± 0.008	0.232 ± 0.022
M_{B3}	---	0.303 ± 0.011	0.276 ± 0.033
W_3	0.124 ± 0.003	0.159 ± 0.006	0.137 ± 0.013
M_{34}	0.113 ± 0.003	0.148 ± 0.010	0.138 ± 0.006
M_{24}	0.186 ± 0.006	0.227 ± 0.018	0.273 ± 0.012
M_{14}	---	0.322 ± 0.024	0.373 ± 0.020
W_4	0.099 ± 0.003	0.128 ± 0.009	0.145 ± 0.008
M_{45}	0.094 ± 0.003	---	---
M_{35}	0.155 ± 0.005	---	---
W_5	0.088 ± 0.003	---	---

Table 3.3.5.1 -
(continued)

Mass	Oxygen	Neon	Magnesium
M_{A1}	0.307 ± 0.006	0.377 ± 0.031	---
M_{B1}	0.293 ± 0.006	0.302 ± 0.024	---
W_1	0.240 ± 0.005	0.266 ± 0.020	---
M_{12}	0.261 ± 0.006	0.204 ± 0.024	0.310 ± 0.032
M_{B2}	0.300 ± 0.007	0.268 ± 0.032	0.401 ± 0.052
M_{A2}	0.287 ± 0.008	0.356 ± 0.046	0.461 ± 0.131
W_2	0.176 ± 0.005	0.170 ± 0.019	0.232 ± 0.024
M_{23}	0.214 ± 0.005	0.213 ± 0.020	0.238 ± 0.029
M_{13}	0.278 ± 0.007	0.260 ± 0.027	0.282 ± 0.042
M_{B3}	0.344 ± 0.010	---	0.285 ± 0.057
W_3	0.176 ± 0.005	0.203 ± 0.020	0.211 ± 0.027
M_{34}	0.152 ± 0.012	0.224 ± 0.041	0.233 ± 0.019
M_{24}	0.285 ± 0.024	0.399 ± 0.089	0.363 ± 0.057
M_{14}	0.360 ± 040	---	---
W_4	0.137 ± 0.012	0.232 ± 0.048	0.194 ± 0.018

3.4. A Critical Evaluation of the High Resolution Data Set

The high resolution data set is to be used for the purposes of computing the ratio of abundances of two isotopes of the same element. In all the cases to be considered here, especially for the elements He, C, N, and O, one isotope is very much less abundant than the other. Much of the difficulty in estimating the isotope abundance ratios arises from the necessity of estimating the shapes of the distribution functions for the mass estimators, due to a single isotope.

Unfortunately, HIST was not exposed to pure beams of single isotopes for calibration purposes, and the flight data must be used both to calibrate HIST and to measure isotope abundances. We will make plausible inferences about the shape of the various mass estimator distribution functions in order to obtain isotope abundance ratio measurements.

Carbon

The measurement of the $^{13}C/^{12}C$ abundance ratio is the most difficult measurement attempted here. Figure 3.4.1 shows a plot of M_{B1} vs. M_{A1} for RANGE 1 carbon. There is a background source for events that have high values of M_{B1}, which may interfere with the clump of events at (13,13) that are probably due to the isotope ^{13}C. The events with high M_{B1} values are possibly caused by M2 retriggering, a phenomenon that is discussed in Spalding (1983). Retriggering is a type of error that can occur in the analog to digital conversion process. If the output of an ADC is equal to $gain \cdot voltage + offset$, then retriggering error gives a digital output equal to $gain \cdot voltage + 2 \cdot offset$, where $offset$ is about ≈ 30 channels.

Figures 3.4.2a-e show the weighted sum mass histograms for carbon events in the time interval 78:266:10 to 78:272:00 (the 78:266 flare), for each RANGE and for the sum of all RANGEs. We will take a very simple approach to finding

the $^{13}C/^{12}C$ abundance ratio. We will count the number of events in the intervals $12.5 \leq W_j \leq 13.5$ and $11.5 \leq W_j \leq 12.5$ and assign them to "^{13}C" and "^{12}C" respectively. Then we will try to correct for spillover from the ^{12}C peak only, as spillover from the ^{13}C peak into the ^{12}C peak makes a statistically insignificant contribution to the $^{13}C/^{12}C$ abundance ratio.

In RANGEs 1 and 2 it appears that a smooth continuation of the ^{12}C peaks will show that events with $12.5 \leq W_j \leq 12.6$ are most likely ^{12}C events. Thus we excluded events with $11.5 \leq W_j \leq 11.6$ from the ^{12}C events and $12.5 \leq W_j \leq 12.6$ from the ^{13}C events. For the remainder of the events in the mass interval $12.6 \leq W_j \leq 13.5$, we made plausible assumptions about the minimum and maximum number of ^{13}C events in the mass interval, and listed those assumptions in table 3.4.1. For example, in RANGE 1, a smooth continuation of the ^{12}C peak might also include up to 2 additional events in the interval $12.6 \leq W_1 \leq 13.5$.

The number of events around mass 11 is comparable to or even greater than the number at mass 13. The two situations are not the same because, as seen in the mass vs. mass cross plots, energy loss mechanisms like those that operate in double strip events, or high radius events, cause the mass estimators to be lower, increasing the low mass background. Thus it makes sense to consider the background separately above and below the main isotope peak.

Table 3.4.1 -

Carbon Mass Assignments

RANGE	max ^{13}C	min ^{13}C	est ^{13}C	^{12}C sampling interval	Total C
1	13	11	12	$11.6 \leq W_1 \leq 12.5$	784
2	3	2	2.5	$11.6 \leq W_2 \leq 12.5$	561
3	6	4	5	$11.5 \leq W_3 \leq 12.5$	535
4	2	1	1.5	$11.5 \leq W_4 \leq 12.5$	151
total R1-4	24	18	21		2031

figure 3.4.1 - A plot of M_{B1} vs. M_{A1} for the time interval 78:266:10 to 78:272:00, for RANGE 1 carbon events. The mass consistency requirements are shown as dashed lines.
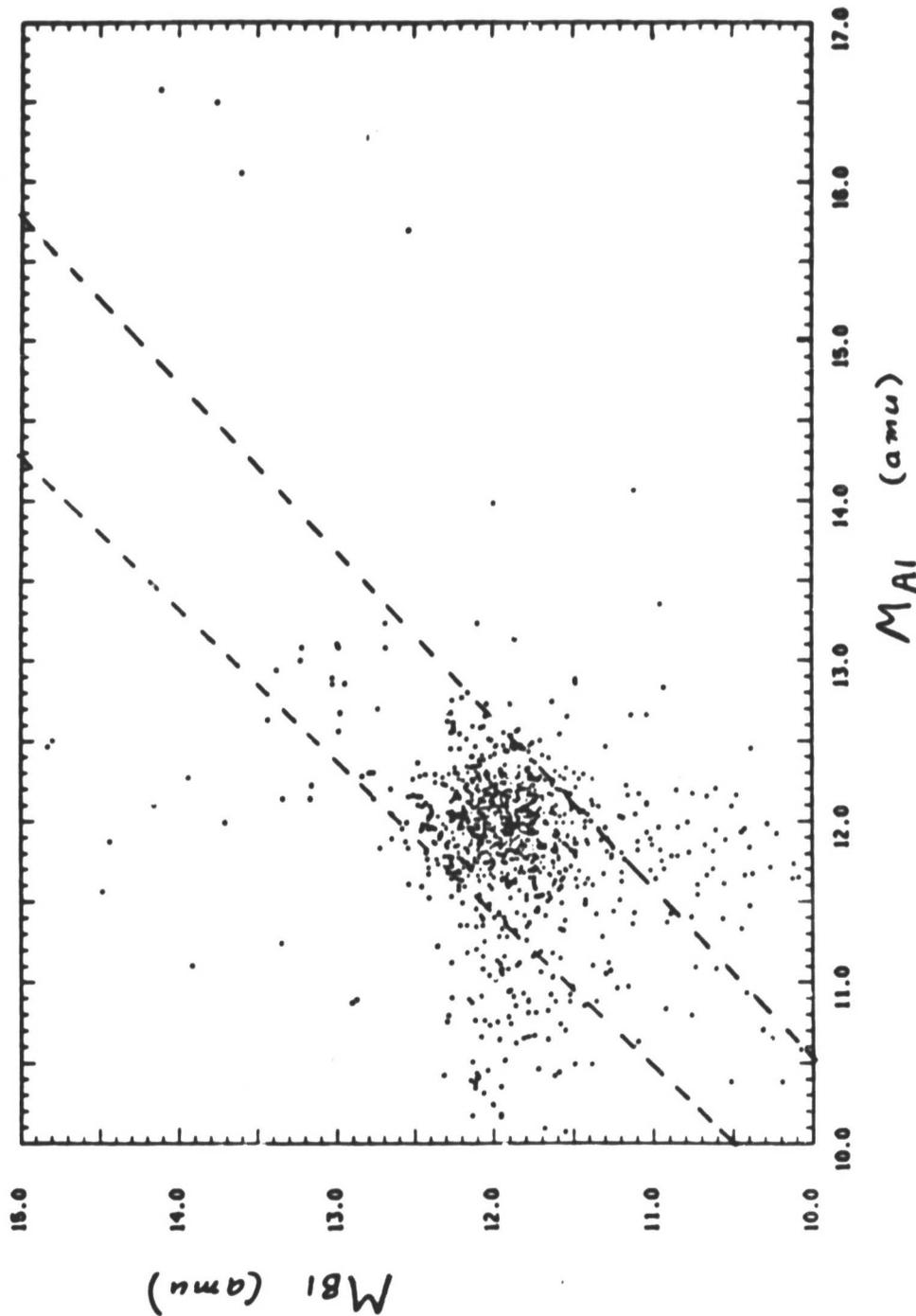
figure 3.4.2a-b - Mass histograms of the weighted sum mass estimator for carbon, for the time interval 78:266:10 to 78:272:00. Figure 3.4.2a is for RANGE 1 and figure 3.4.2b is for RANGE 2.
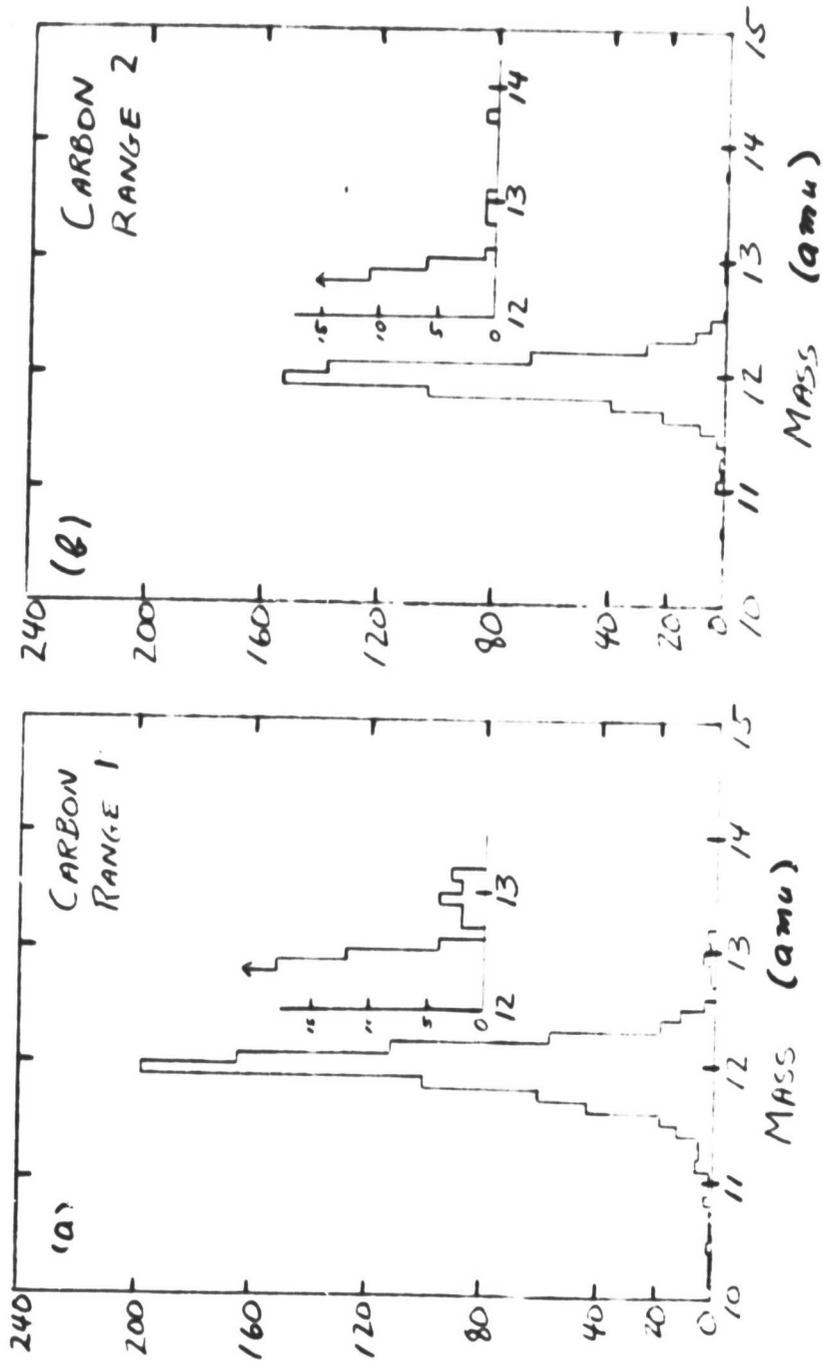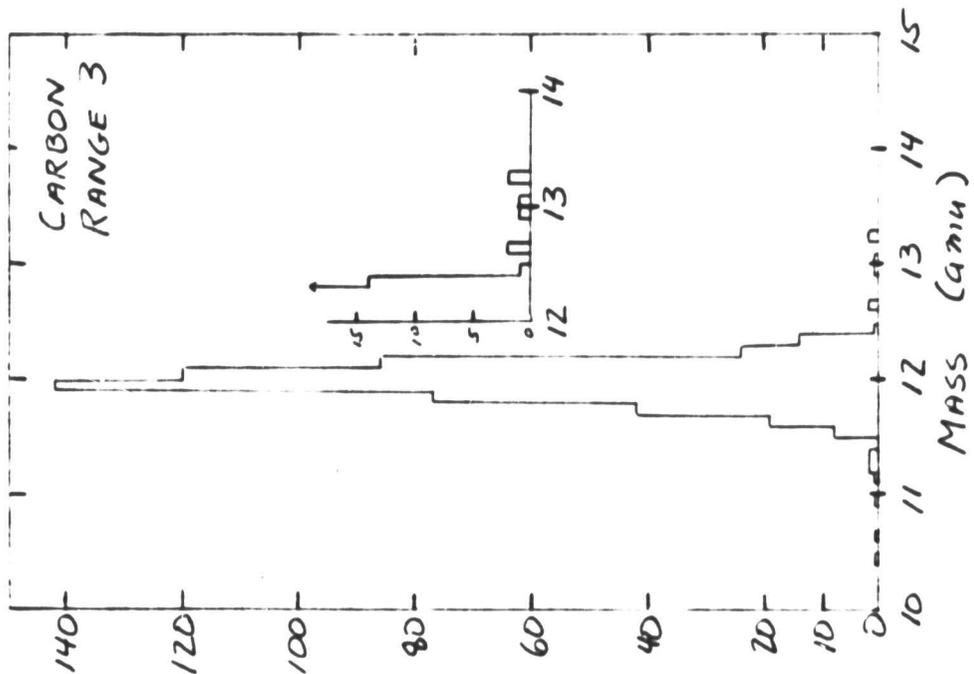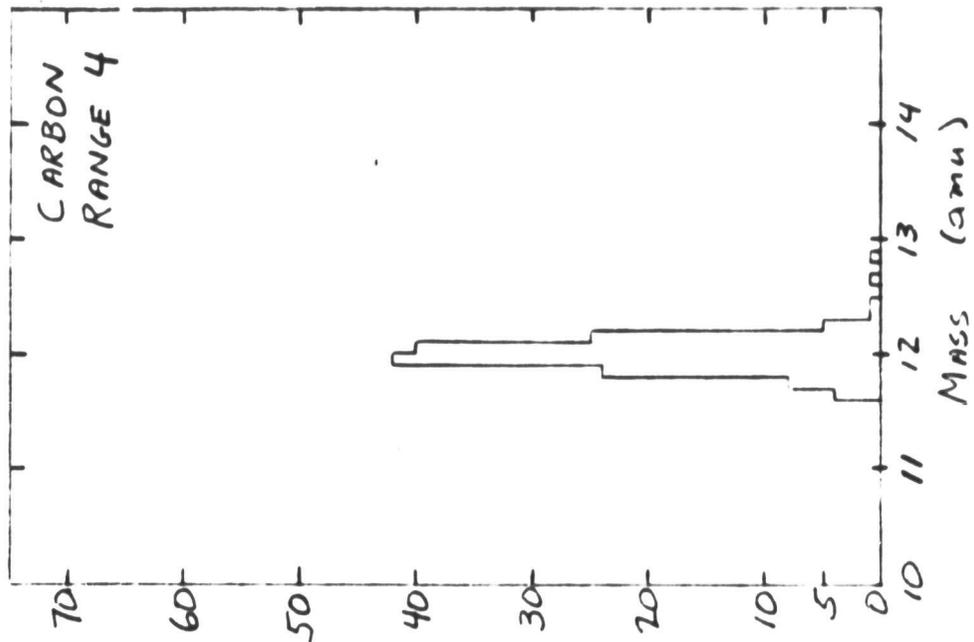
figure 3.4.2c-d - Mass histograms of the weighted sum mass estimator for carbon, for the time interval 78:266:10 to 78:272:00. Figure 3.4.2c is for RANGE 3 and figure 3.4.2d is for RANGE 4.
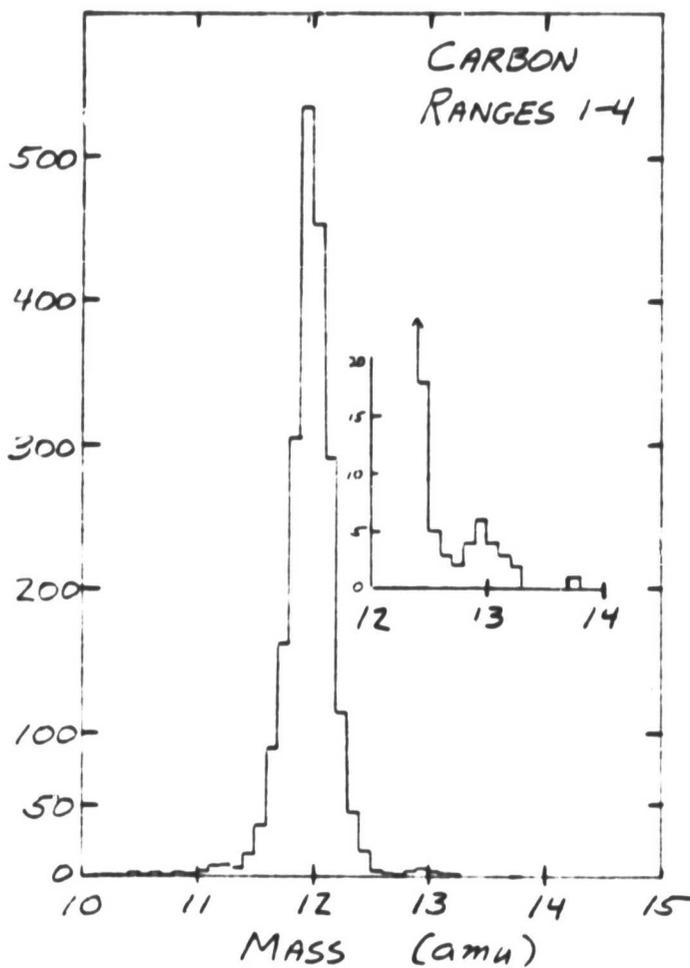
figure 3.4.2e - A mass histogram of the weighted sum mass estimator for
carbon, for RANGEs 1-4 and for the time interval 78:266:10 to 78:272:00.

Oxygen

The RANGE 1 cross plot for oxygen in the 78:266 flare is shown in figure 3.4.3. For ^{16}O the background situation is much better than for ^{12}C, the ^{16}O area is further from the source of the high mass M_{B_1} background source. Figure 3.4.4 shows the weighted sum mass histogram for RANGEs 1-4.

For an upper limit to the $^{17}O/^{16}O$ abundance ratio, we noticed that the region $16.5 \leq W_j \leq 17.0$ has 56 events and the region $17.0 \leq W_j \leq 17.5$ has only one event. Then to measure the $^{17}O/^{16}O$ ratio, we used the interval $17.0 \leq W_j \leq 17.5$ for the ^{17}O event sample and the interval $16.0 \leq W_j \leq 16.5$ for the ^{16}O event sample.

For the $^{18}O/^{16}O$ ratio, we counted ^{16}O events in the interval $15.5 \leq W_j \leq 16.5$, and ^{18}O events in the interval $17.5 \leq W_j \leq 18.5$. For a background estimate, there is one event in the interval $18.5 \leq W_j \leq 19.5$, so we inferred a maximum number of 6, a minimum number of 5 events, and a "best" estimate of 5.5 events due to ^{18}O in the interval $17.5 \leq W_j \leq 18.5$.

Table 3.4.2 -

Oxygen Mass Assignments

RANGE	^{17}O	^{18}O	^{16}O sampling interval	^{16}O
1-4	1	---	$16.0 \leq W_j \leq 16.5$	1448
1-4	---	5-6	$15.5 \leq W_j \leq 16.5$	3142

figure 3.4.3 - A M_{B1} vs. M_{A1} cross plot for RANGE 1 oxygen events in the time interval 78:266:10 to 78:272:00 The dashed lines show the mass consistency requirements adopted.
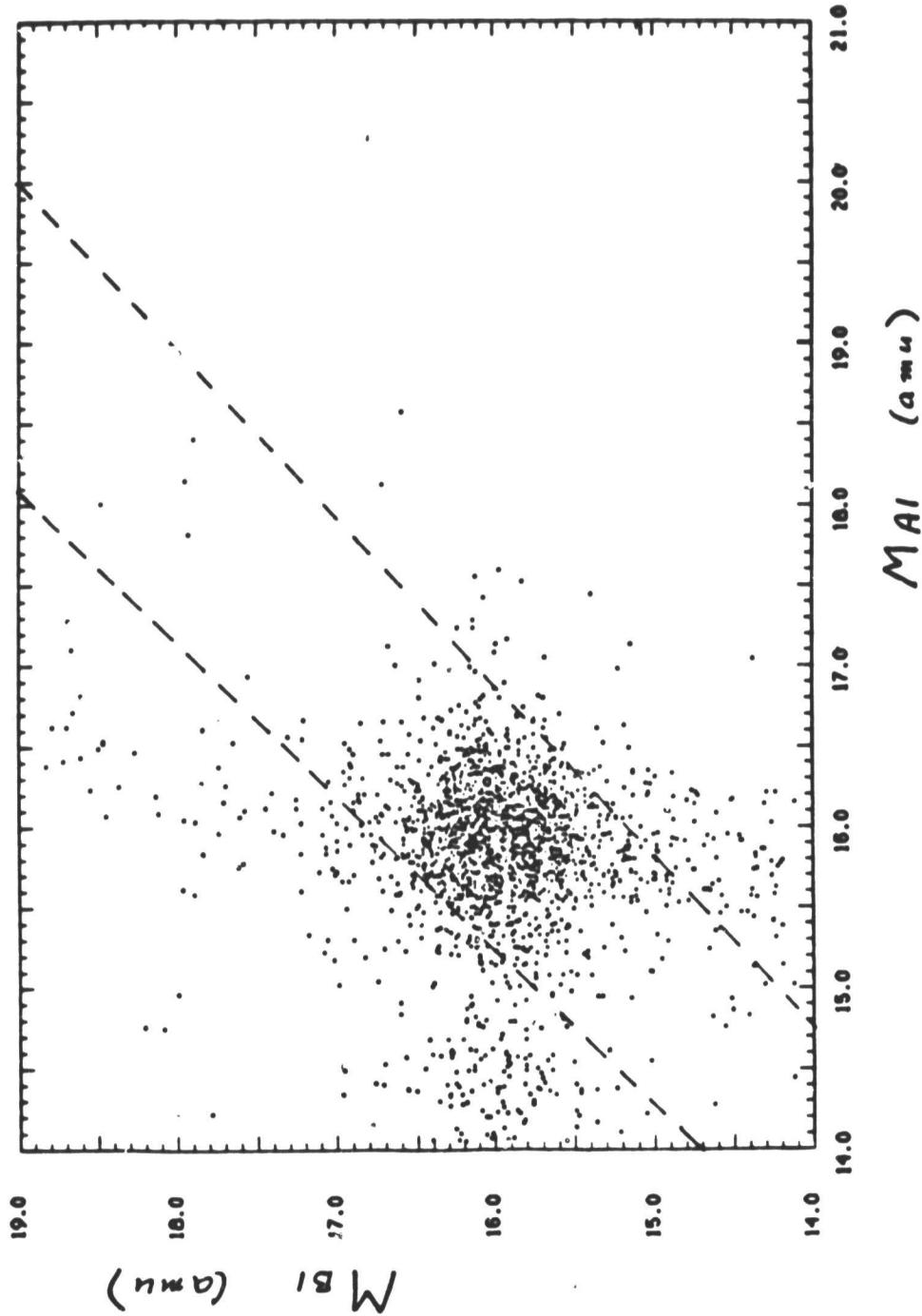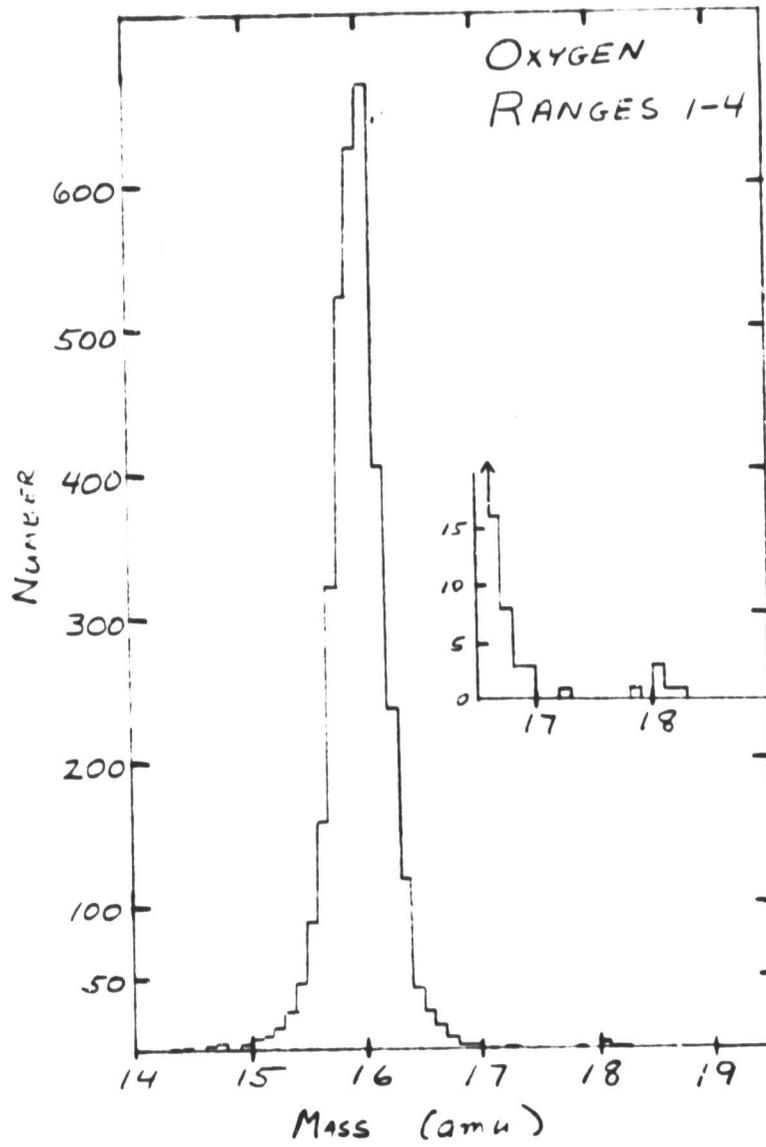
figure 3.4.4 - A histogram of the weighted sum mass estimator for oxygen in RANGEs 1-4 for the time interval 78:266:10 to 78:272:00.

Nitrogen

The nitrogen weighted sum histogram for the 78:266 flare for RANGEs 1-4 is shown in figure 3.4.5. A smooth continuation of the ^{14}N peak may result in up to two events in the interval $14.5 \leq W_j \leq 15.5$ due to ^{14}N, giving a maximum number of 4, a minimum number of 2, and a best estimate of 3 ^{15}N events. There are 360 events in the interval $13.5 \leq W_j \leq 14.5$.

figure 3.4.5 - A mass histogram of the weighted sum mass estimator for nitrogen in the time interval 78:266:10 to 78:272:00, for RANGEs 1-4.


NITROGEN RANGES 1-4

MASS (amu)
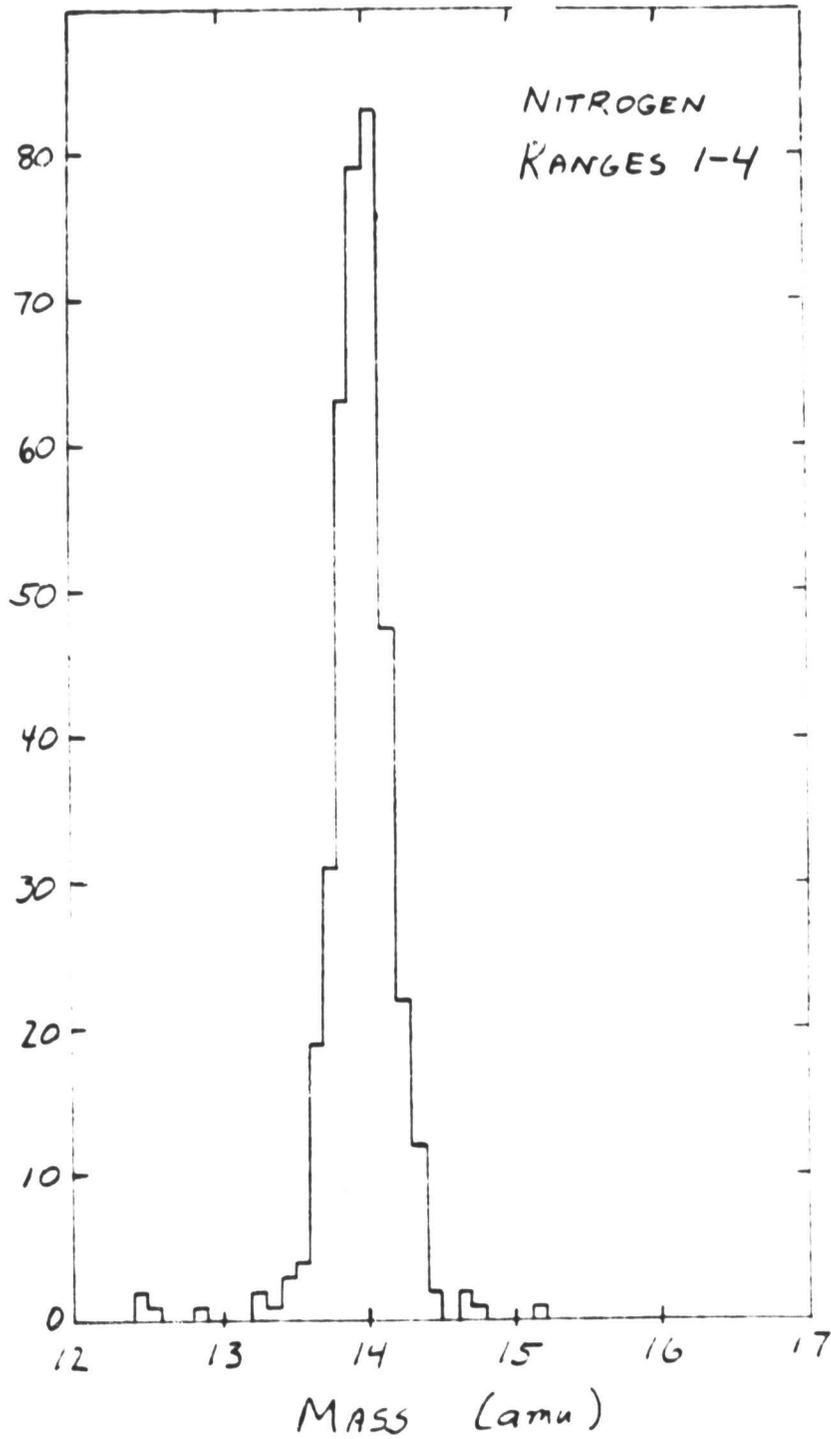
Neon

The neon measurements for the 78:266 flare are shown in figures 3.4.6a-b. To calculate the $^{22}Ne/^{20}Ne$ abundance ratio we used data from RANGEs 1-4. The ^{22}Ne measurements are not influenced as much as carbon and oxygen, by the high mass shape of the main isotope peak, and we estimate that the background at ^{22}Ne due to ^{20}Ne is negligible. To calculate the $^{21}Ne/^{20}Ne$ abundance ratio we will use only RANGEs 2-4, to avoid making any guesses about the RANGE 1 ^{20}Ne peak shape.

Table 3.4.3 -

| RANGE	^{21}Ne	^{22}Ne	^{20}Ne sampling interval	^{20}Ne
1	0-6	12	$19.5 \leq W_1 \leq 20.5$	103
2	0	12	$19.5 \leq W_2 \leq 20.5$	62
3	0	7	$19.5 \leq W_3 \leq 20.5$	77
4	0	0	$19.5 \leq W_4 \leq 20.5$	6
total R2-4	0	19	$19.5 \leq W_j \leq 20.5$	145
total R1-4	0-6	31	$19.5 \leq W_j \leq 20.5$	248

figure 3.4.6a-b - Neon weighted sum mass estimators for the time interval 78:266:10 to 78:272:00. Figure a is for RANGE 1 and figure b is the sum of RANGEs 2-4.
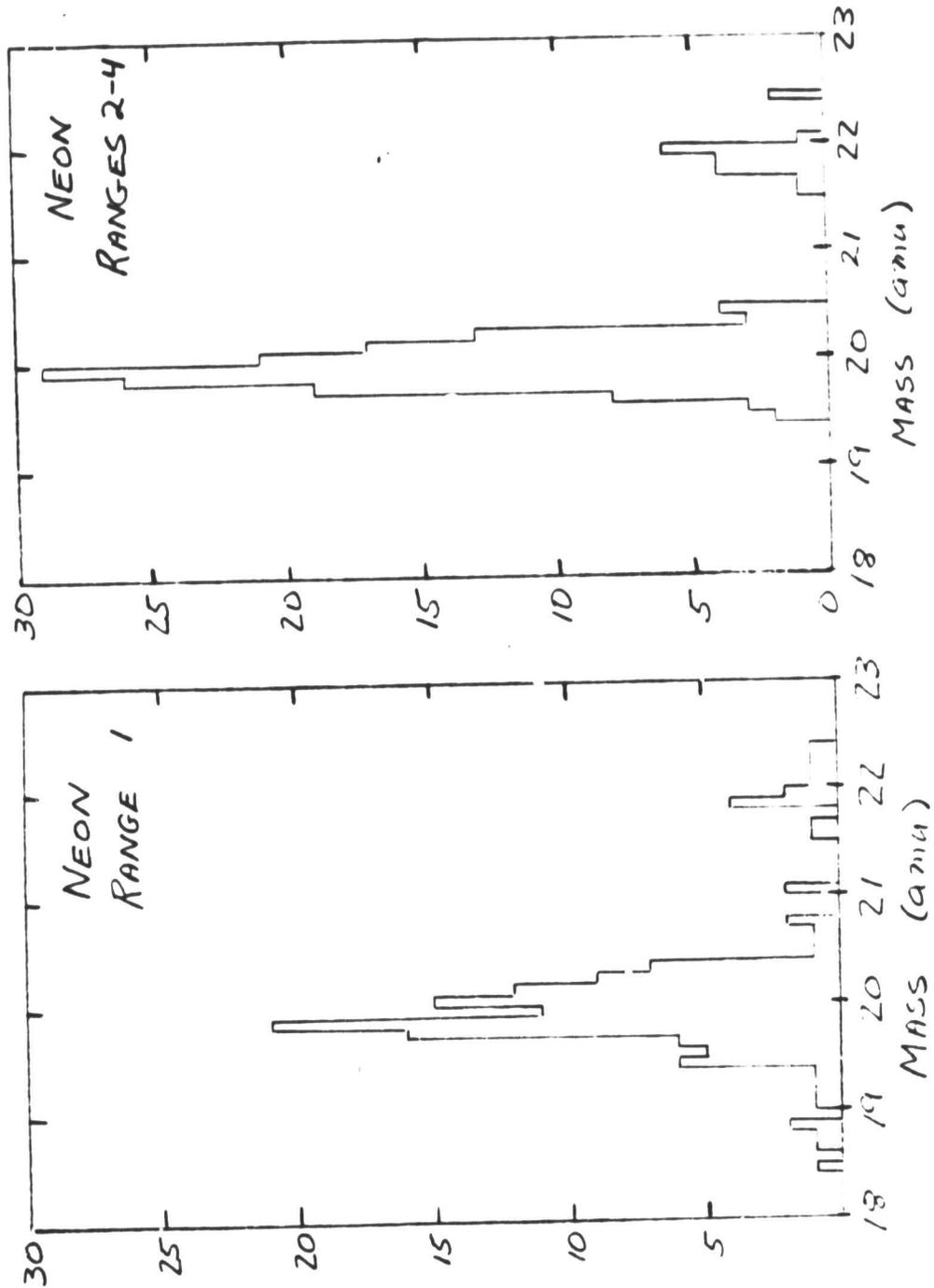
Magnesium

A histogram of the weighted sum mass estimator for magnesium is shown in figure 3.4.7. To estimate the $^{25}Mg/^{24}Mg$ and $^{26}Mg/^{24}Mg$ abundance ratios we will assume that the single isotope peak shape is a Gaussian. ^{25}Mg and ^{26}Mg are abundant enough that the shape of the tails of the mass estimator distribution function is not very important. In section 3.5 we will describe the method used to obtain values and uncertainties for the Mg abundance ratios.

figure 3.4.7 - Magnesium weighted sum mass estimator in the time interval 78:266:10 to 78:272:00, for RANGEs 2-4.
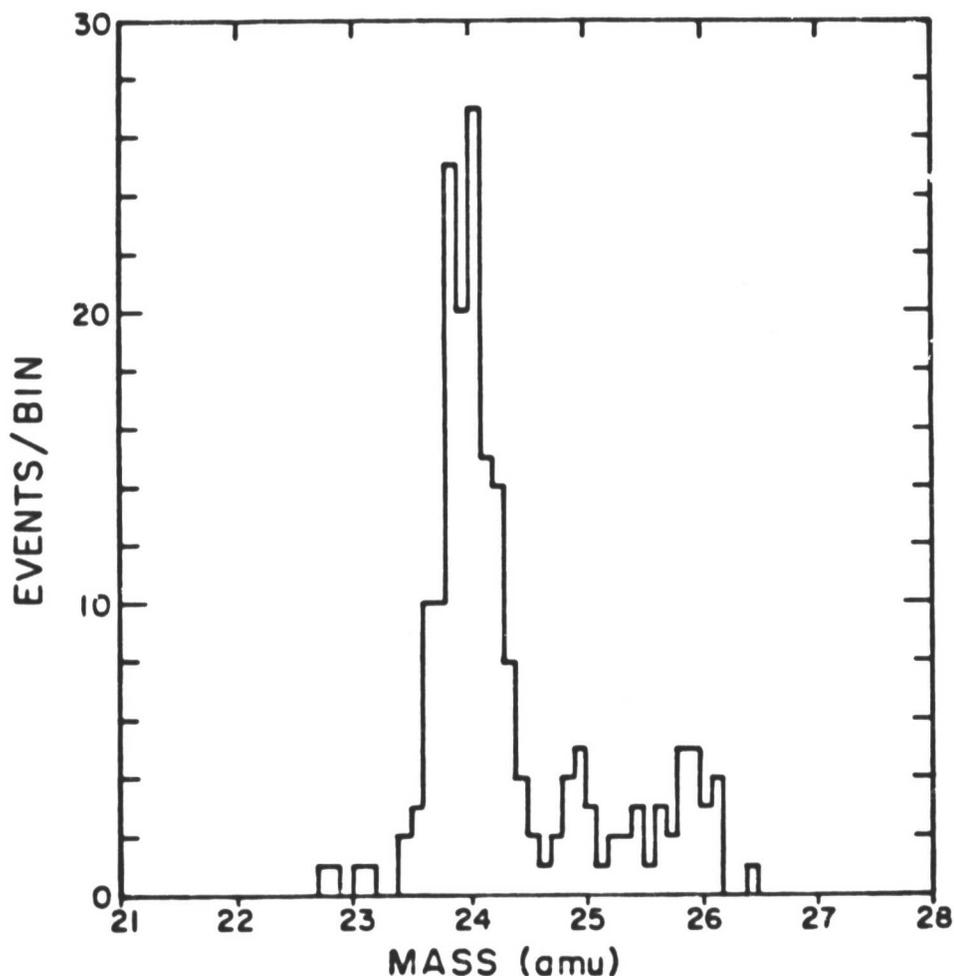
Helium

For helium we analyzed the data in two parts, RANGE 1 and RANGEs 2-5. The data for the weighted sum results for RANGEs 2-5, in the time interval 78:266:10 to 78:272:00, are shown in figure 3.4.8b. We chose mass sampling intervals of $2.5 \leq W_j \leq 3.4$ for ^{3}He and $3.5 \leq W_j \leq 4.4$ for ^{4}He because we felt that it was likely that events in the mass interval $3.4 \leq W_j \leq 3.5$ were due to ^{4}He. For RANGEs 2-5 we found no ^{3}He events and 1020 ^{4}He events.

The weighted sum results for helium RANGE 1 events in the same time interval are shown in figure 3.4.8a. Figure 3.4.9 is a plot of weighted sum RANGE 1 data for the ^{3}He-rich time periods 78:296:09 to 78:297:09 and 78:307:00 to 78:308:00, for comparison and to establish the accuracy of the mass scale. Using the same mass sampling intervals as for RANGEs 2-5, we find 4 ^{3}He events and 512 ^{4}He events in the data from the 78:266 flare.

The RANGE 1 data set is of poorer quality than the RANGEs 2-5 He data set. We would like to consider the possibility that the events in the ^{3}He RANGE 1 mass sampling interval are caused by ^{4}He particles. If the ^{4}He particles may have experienced simultaneous "signal defects" in the measurements of the energies deposited in detectors M1 and M2, they might have mimicked ^{3}He particles with no "signal defects". Figure 3.4.10 shows a cross plot of M_{B1} vs. M_{A1} for the RANGE 1 data, with the consistency requirements drawn in as dashed lines. There is a group of three events near the position (3,3), which may be the result of simultaneous signal losses in detectors M1 and M2.

If we assume that the probability of a signal defect in M2 is independent of the probability of a signal defect in M1, a rough estimate of the background due to ^{4}He around the position (3,3) can be made. If we restrict M_{B1} to the interval $3.5 \leq M_{B1} \leq 4.5$, then the ratio of events with $3.5 \leq M_{A1} \leq 4.5$ to events with $2.5 \leq M_{A1} \leq 3.5$ is $0.075 \pm .012$. For the background estimate we restrict M_{B1} to

$2.5 \leq M_{B1} \leq 3.5$. There is a small correlation between a signal defect in detector M2 and the mass estimator M_{A1}. We expect the main peak of the M_{A1} histogram to shift slightly, under the requirement for a signal defect in M2, which is represented by the equation $2.5 \leq M_{B1} \leq 3.5$. Then there are 40 events with $2.5 \leq M_{B1} \leq 3.5$ and $3.4 \leq M_{A1} \leq 4.4$, with a mean mass of $3.89 \pm .03$. The number of events predicted in the region $2.4 \leq M_{A1} \leq 3.4$ and $2.5 \leq M_{B1} \leq 3.5$ is then 3.0 (+3.0, −1.7), which is consistent with the observed number of events. Thus we will evaluate helium observations as placing an upper limit on the amount of ^{3}He observed. Table 3.4.4 displays the observed numbers of He events.

Table 3.4.4 -

RANGE	^{3}He	^{4}He	^{4}He sampling interval
1	4	512	$3.5 \leq W_1 \leq 4.4$
2-5	0	1020	$3.5 \leq W_j \leq 4.4$

figure 3.4.8a-b - Helium weighted sum mass estimator in the time interval 78:266:10 to 78:272:00. Figure 3.4.8a is data from RANGE 1, and figure 3.4.8b is data from RANGEs 2-5.
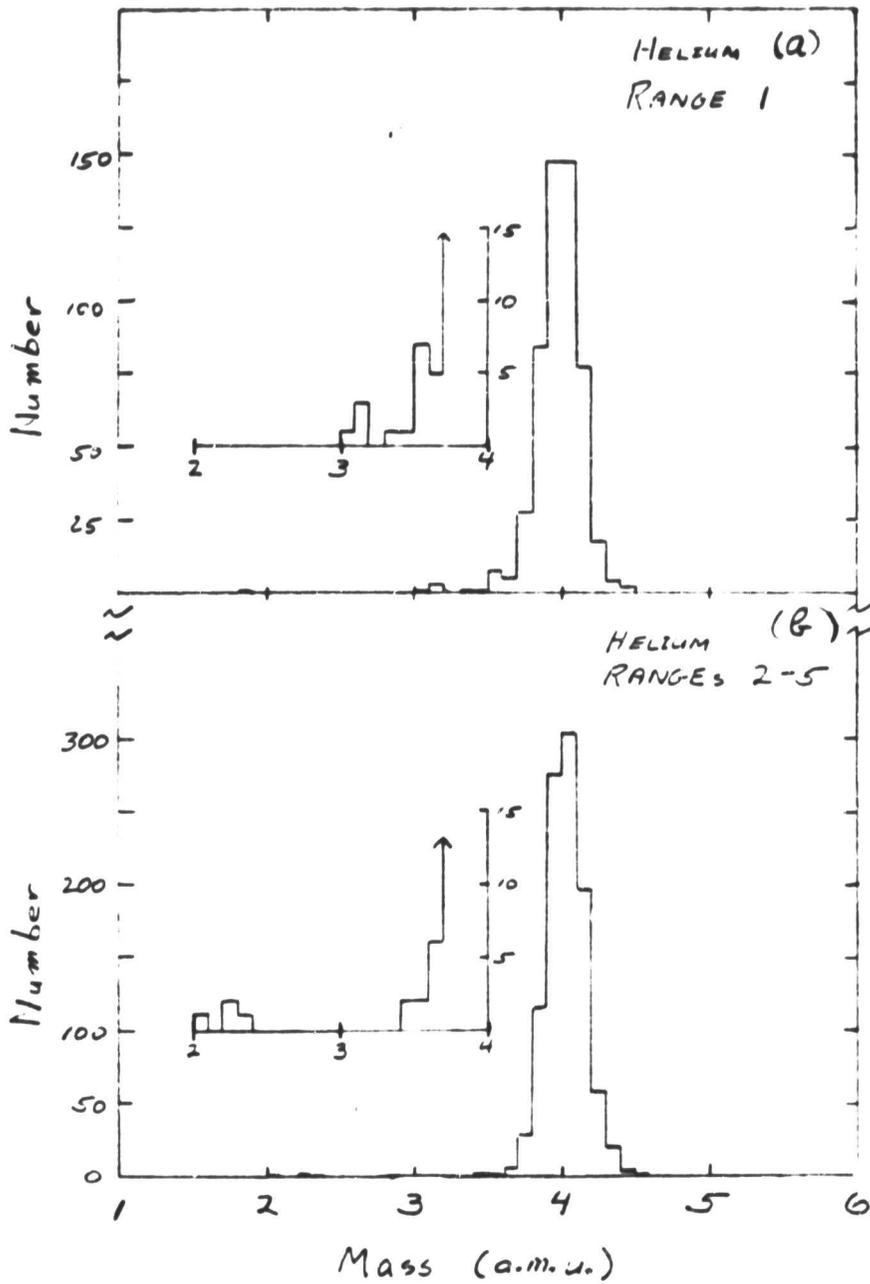
figure 3.4.9 - Helium weighted sum mass estimator for RANGE 1. The time intervals are from 78:296:09 to 78:297:09 and 307:00 to 308:00, and include two [3]He-rich flares.
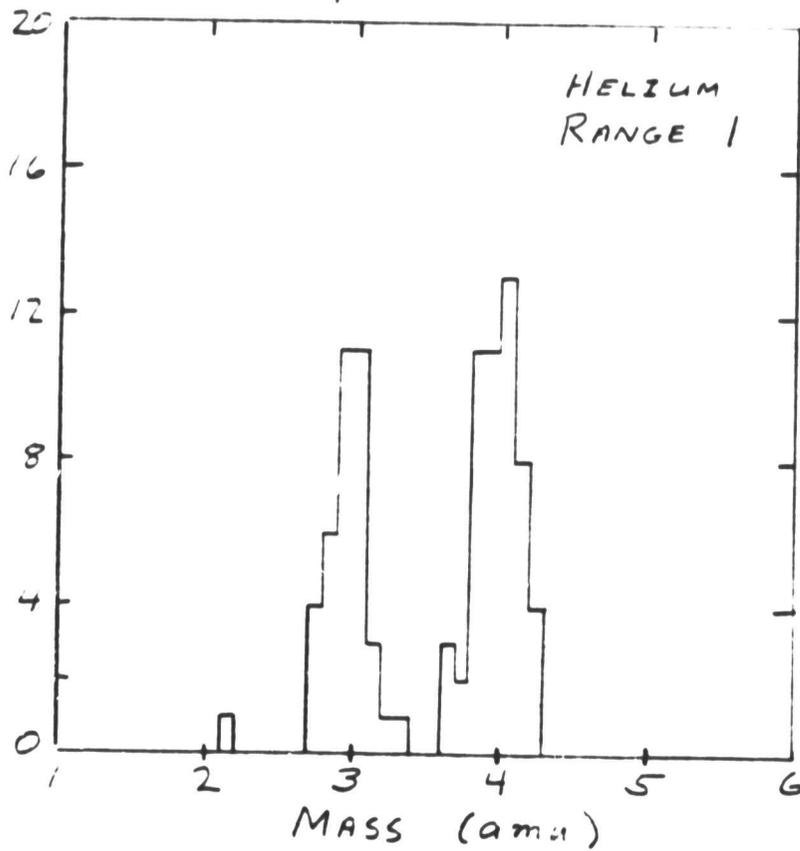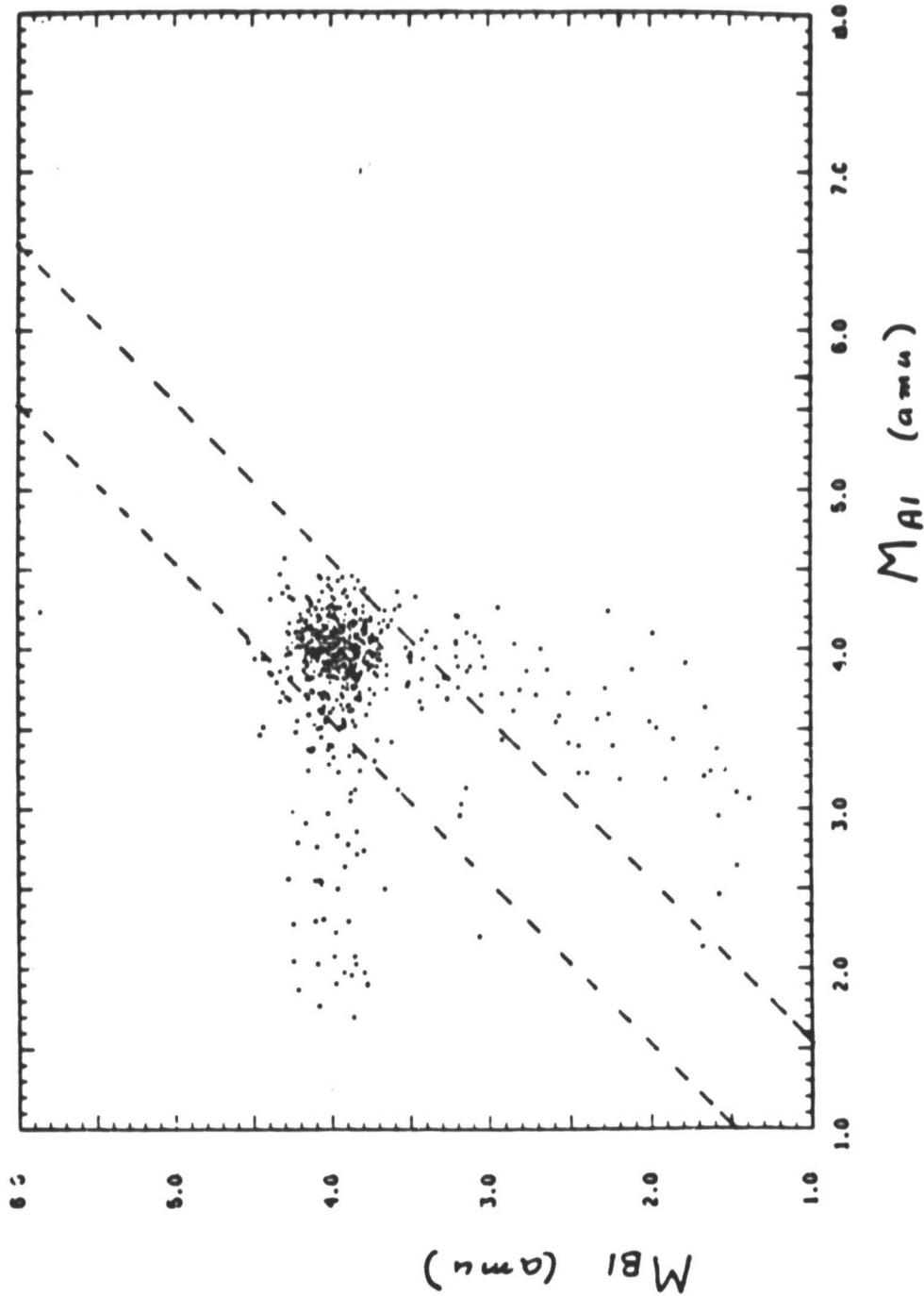
figure 3.4.10 - M_{B1} vs. M_{A1} for RANGE 1 helium events in the time interval 78:266:10 to 78:272:00. The dashed lines show the mass consistency requirements adopted.

3.5. Isotope Abundance Ratios and Uncertainties

For each element, the results of the mass measurements were expressed as the ratio of the abundance of a rarer isotope to that of the most abundant isotope for that element. For nitrogen, the result labeled as "$^{15}N/^{14}N$" is the ratio of the observed abundance of ^{15}N to the abundance of ^{14}N. The maximum likelihood technique was used to determine the most likely value for the abundance ratios, and to calculate the statistical uncertainties in the abundance ratios.

For the element magnesium, the weighted sum histogram for each RANGE had been fit by the chisquare technique, with Gaussian peak shapes. This determined the rms. width, σ_M, and the location of the mass peaks. Fixing σ_M and the location of the mass peaks for each RANGE, the likelihood function had two free parameters, $\alpha = {}^{25}Mg/{}^{24}Mg$ and $\beta = {}^{26}Mg/{}^{24}Mg$. The free parameters were allowed to vary to find the maximum likelihood solution, fitting all RANGEs simultaneously. The statistical uncertainties in the two parameters were found by numerically integrating the likelihood function. Let

$$I_L(x) = \frac{\int\limits_0^x \int\limits_0^\infty L(\alpha,\beta)\,d\alpha d\beta}{\int\limits_0^\infty \int\limits_0^\infty L(\alpha,\beta)\,d\alpha d\beta} \quad . \tag{3.5.1}$$

Then the confidence interval for the parameter α at a level of confidence C is $[y_1, y_2]$ where

$$\frac{1-C}{2} = I_a(y_1) \tag{3.5.2}$$

and

$$1 - \left(\frac{1-C}{2}\right) = I_a(y_2) \quad . \tag{3.5.3}$$

The probability that α will be found within the confidence interval is C, if the "a *priori*" probability distribution for α is uniform on the real axis.

For magnesium the form of the likelihood function chosen was

$$L(\alpha,\beta) = \prod_{i=1}^{N} p_i(M_i,\alpha,\beta) \tag{3.5.4}$$

with

$$p_i = \sum_{\gamma=24}^{26} \frac{A_\gamma}{\sigma_M\sqrt{2\pi}} \exp\left[-(M_i - M_\gamma^o)^2/2\sigma_M^2\right] \tag{3.5.5}$$

where

$$A_{24} = \frac{1}{\alpha+\beta+1} \quad ; \quad A_{25} = \frac{\alpha}{\alpha+\beta+1} \quad ; \quad A_{26} = \frac{\beta}{\alpha+\beta+1} \quad ; \tag{3.5.6}$$

and

$$\alpha = {}^{25}Mg/{}^{24}Mg \quad ; \quad \beta = {}^{26}Mg/{}^{24}Mg \quad ;$$
$$M_\gamma^o = mass\ of\ isotope\ \gamma \quad ;$$
$$M_i = weighted\ sum\ mass\ estimator\ for\ particle\ i \quad .$$

For carbon, the uncertainties in the abundance ratios were dominated by uncertainties in the shape of the mass peak for ^{12}C. We then made plausible assumptions about the mass peak shape, as detailed in section 3.4, and obtained maximum and minimum abundances for the isotope ^{13}C. The likelihood function chosen was

$$L(\alpha,\beta) = (A_{12})^{N-n_{13}-n_{14}} (A_{13})^{n_{13}} (A_{14})^{n_{14}} \quad . \tag{3.5.7}$$
$$\alpha = {}^{13}C/{}^{12}C \quad ; \quad \beta = {}^{14}C/{}^{12}C \quad ;$$
$$A_{12} = \frac{1}{\alpha+\beta+1} \quad ; \quad A_{13} = \frac{\alpha}{\alpha+\beta+1} \quad ; \quad A_{14} = \frac{\beta}{\alpha+\beta+1} \quad ;$$

where N is the total number of events observed and n_{13} is the number of ^{13}C events. The upper limit to the abundance ratio $^{13}C/^{12}C$ was obtained by solving equation 3.5.3 with the above likelihood function, with n_{13} set equal to the maximum number (24) of ^{13}C events from section 3.4. The lower limit to the abundance ratio was found by setting n_{13} to the minimum number (18) of ^{13}C events, and solving equation 3.5.2. We used the mean of the maximum and minimum number of ^{13}C events as our best estimate of the ^{13}C abundance.

The elements nitrogen and helium used a likelihood function of the type 3.5.7, but with only one variable, as these elements have only two long-lived isotopes.

Oxygen $^{16}O/^{18}O$ and $^{17}O/^{18}O$ abundance ratios and uncertainties were calculated separately, with one variable likelihood functions of the type 3.5.7 and using the data in table 3.4.2.

The neon $^{21}Ne/^{20}Ne$ abundance ratio was estimated using the data from RANGEs 2-4, with a likelihood function similar to equation 3.5.7. The $^{22}Ne/^{20}Ne$ abundance ratio and uncertainties were calculated with the data from RANGEs 1-4 and a likelihood function similar to equation 3.5.7.

The results of the confidence interval calculations for all elements analyzed appear in table 4.1.

3.6. Isotope Sampling Corrections

Different isotopes of the same charge, that stop in a given RANGE, sample energy intervals that differ slightly. If we approximate the range energy relation by a power law, we then find that the isotopes A_1 and A_2, which each stop in a distance R_0, and have energies per nucleon X_{A1} and X_{A2}, are related by the equation

$$\frac{X_{A1}}{X_{A2}} = \left[\frac{A_2}{A_1}\right]^{\frac{1}{\lambda}} \quad . \tag{3.6.1}$$

Thus the heavier isotope has a lower energy per nucleon to travel the same distance. This effect introduces a bias into any isotope abundance ratio measurement obtained by integrating measurements made over one RANGE.

We can compute the bias in the isotope abundance ratio introduced by integrating the observations by RANGE, if we assume that the isotopes in the abundance ratio have the same spectral "shape". Suppose that the flux of isotope j, per $cm^2 - sec - sr - MeV/nuc$, at an energy/nuc, e, is

$$\frac{dJ_j}{de} = K_j \, f(e), \tag{3.6.1}$$

and that the flux for isotope i is

$C-2$

$$\frac{dJ_i}{de} = K_i \, f'(e). \tag{3.6.2}$$

For element X, the ratio of the abundance of isotope i to the abundance of isotope j, is

$$\frac{X_j}{X_i} = \frac{K_j}{K_i} , \tag{3.6.3}$$

and the spectra of isotopes i and j are considered to have the same spectral shape as a function of energy/nuc.

Let $< X_j >$ be the number of events of isotope j, measured in a given RANGE, an interval in pathlength from $R(L)$ to $R(U)$. Let $e_j(U)$ be the energy/nuc, such that isotope j is stopped by a thickness $R(U)$ of silicon. Then

$$< X_j > = \int_{e_j(L)}^{e_j(U)} K_j \, f(e) \, de \equiv K_j \, C_j \tag{3.6.4}$$

and

$$\frac{K_j}{K_i} = \frac{< X_j >}{< X_i >} \left[\frac{C_i}{C_j} \right] . \tag{3.6.5}$$

Thus we must multiply the observed ratio of $< X_j >/< X_i >$ in a RANGE by the correction factor C_i / C_j. Suppose that ^{20}Ne and ^{22}Ne have the same spectral shape as a function of energy/nuc, and that $f(e) = (\frac{1}{e})^3$. If $R(L)$ is equal to the range of ^{20}Ne at 25 MeV/nuc, and $R(U) = \infty$, then

$$\frac{K_{22}}{K_{20}} = \frac{< ^{22}Ne >}{< ^{20}Ne >} \, 0.897 . \tag{3.6.6}$$

We can measure the spectra of the more abundant isotope as a function of energy/nuc, $K_j \, f(e)$. If we assume that the spectra of the less abundant isotope has the same shape as a function of energy/nuc, we can compute the correction factor C_j / C_i. That assumption is equivalent to the assumption that the isotopes' spectra have the same shape as some arbitrary function of the isotopes' velocity.

The diffusive propagation of solar energetic particles from Sun to Earth in

the interplanetary medium is thought to depend on the particles' rigidity, or momentum per charge. Thus two isotopes of the same element might have spectra which were the same shape as a function of rigidity. We can also compute the corrections to the isotope abundance ratios for this case. If the two isotopes carry the same number of electrons, then they also have the same spectral shape as a function of their total momentum.

Suppose that the flux of isotope j, per $cm^2 - sec - sr - MeV/c$ is

$$\frac{dJ_j}{dP} = K_j \, g(P) \tag{3.6.7}$$

and the flux of isotope i is

$$\frac{dJ_i}{dP} = K_i \, g(P) \, . \tag{3.6.8}$$

Let $P_j(U)$ be the total momentum, such that isotope j is stopped by a thickness $R(U)$ of silicon. Then

$$<X_j> = \int_{P_j(L)}^{P_j(U)} K_j \, g(P) \, dP \, . \tag{3.6.9}$$

If p is equal to the momentum per nucleon, $p_j = \dfrac{P_j}{A_j}$.

$$<X_j> = A_j \int_{P_j(L)}^{P_j(U)} K_j \, g(A_j p) \, dp \equiv K_j \, A_j \, D_{j\,j} \, . \tag{3.6.10}$$

For isotope i,

$$<X_i> = \int_{P_i(L)}^{P_i(U)} K_i \, g(P) \, dP \tag{3.6.11}$$

$$= A_i \int_{p_i(L)}^{p_i(U)} K_i \, g(A_i p) \, dp$$

$$= A_j \int_{(A_i/A_j) \, p_i(L)}^{(A_i/A_j) \, p_i(U)} K_i \, g(A_j p) \, dp$$

$$\equiv A_j \, K_i \, D_{i\,j} \, .$$

Thus we have

$$\frac{K_j}{K_i} = \frac{<X_j>}{<X_i>} \left[\frac{D_{i\,j}}{D_{j\,j}} \right] \, . \tag{3.6.12}$$

We can measure the spectra of isotope j, as a function of momentum per nucleon,

$$\frac{dJ_j}{dp} = A_j \, K_j \, g(A_j p) \, . \tag{3.6.13}$$

If we assume that $\frac{dJ_i}{dP}$ has the same spectral shape as a function of total momentum or rigidity, then we can calculate $\frac{D_{j\,i}}{D_{i\,j}}$, and correct for the RANGE sampling effect, as follows. Let

$$\int_{p_j(L)}^{p_j(U)} \frac{dJ_j}{dp} \, dp \; = \; A_j \, K_j \, D_{j\,j} \; = \; D^{\bullet}_j \; , \tag{3.6.14}$$

and

$$\int_{(A_i/A_j)\,p_i(L)}^{(A_i/A_j)\,p_i(U)} \frac{dJ_j}{dp} \, dp \; = \; A_j \, K_j \, D_{i\,j} \; = \; D^{\bullet}_{i\,j} \; . \tag{3.6.15}$$

then

$$\frac{D^{\bullet}_{i\,j}}{D^{\bullet}_{j\,j}} \; = \; \frac{D_{i\,j}}{D_{j\,j}} \; . \tag{3.6.16}$$

Suppose that ^{20}Ne and ^{22}Ne have the same spectral shape as a function of total momentum, and that

$$\frac{dJ_{20}}{dp} = (\frac{1}{e})^3 \, \frac{de\,(p)}{dp} \; . \tag{3.6.17}$$

For $R(L)$ equal to the range of ^{20}Ne at 25 MeV/nuc, and $R(U) = \infty$,

$$\frac{K_{22}}{K_{20}} = \frac{<\,^{22}Ne>}{<\,^{20}Ne>} \, 1.306. \tag{3.6.18}$$

Note that these two assumptions about the spectral shape have produced correction factors that operate in different directions upon the data.

The isotope abundance correction factors were calculated for each range and isotope ratio, using both of the above assumptions about the functional dependence of the spectra. The spectral shape chosen for elements C, N, O, Ne, and Mg, for the most abundant isotope, was the six element spectral fit of section 3.9. For helium, we used the helium spectral fit, also from section 3.8. The

integrals of equation 3.6.2 were done numerically.

To obtain the isotope abundance factors for measurements that integrated data over several RANGEs, we computed a weighted mean of the correction factors for each RANGE, using for weights the number of events of the given element observed in each RANGE.

The isotope abundance correction factors are listed in table 3.6.1.

Table 3.6.1 -

Ratio	RANGE	E/nuc functional dependence	Momentum functional dependence
$^{13}C/^{12}C$	1	0.942	1.131
	2	0.918	1.243
	3	0.883	1.371
	4	0.824	1.673
	1-4	0.911	1.266
$^{14}C/^{12}C$	1	0.892	1.292
	2	0.852	1.568
	3	0.790	1.871
	4	0.694	2.846
	1-4	0.839	1.638
$^{15}N/^{14}N$	1	0.935	1.120
	2	0.919	1.232
	3	0.891	1.327
	4	0.834	1.625
	1-4	0.913	1.238
$^{17}O/^{16}O$	1	0.950	1.121
	2	0.919	1.214
	3	0.899	1.299
	4	0.836	1.537
	1-4	0.928	1.195
$^{18}O/^{16}O$	1	0.907	1.264
	2	0.852	1.470
	3	0.813	1.695
	4	0.713	2.178
	1-4	0.867	1.436
$^{21}Ne/^{20}Ne$	1	0.948	1.116
	2	0.929	1.180
	3	0.908	1.263
	4	0.879	1.319
	2-4	0.918	1.228
$^{22}Ne/^{20}Ne$	1	0.902	1.252
	2	0.866	1.391
	3	0.914	1.605
	4	0.773	1.829
	1-4	0.869	1.400

**Table 3.6.1 -
(cont.)**

Ratio	RANGE	E/nuc functional dependence	Momentum functional dependence
$^{25}Mg/^{24}Mg$	2	0.935	1.158
	3	0.914	1.241
	4	0.921	1.182
	1-4	0.923	1.202
$^{26}Mg/^{24}Mg$	2	0.877	1.342
	3	0.840	1.540
	4	0.846	1.335
	1-4	0.856	1.444
$^{3}He/^{4}He$	1	1.247	0.873
	2	1.310	0.597
	3	1.404	0.504
	4	1.470	0.360
	5	1.874	0.259
	1-5	1.346	0.566
	2-5	1.398	0.510

3.7. Low Resolution Data Set

We defined a low resolution data set for the purpose of measuring the energy spectra of various elements measured by HIST. We relaxed the requirements of the high resolution data set to obtain more events and more coverage of lower energies (primarily through the acceptance of RANGE 0 events).

Element identification was through two parameter analysis. In RANGEs 0 and 1, we required that the mass computed using the two deepest detectors triggered be within 3 amu of the principal isotope of the element. In RANGE 1, carbon events thus had to have $9 \le M_{B1} \le 15$ to be included in the low resolution data set. For RANGEs 2-5, the two parameter mass had to be equal to the principal mass plus 3 or minus 2 amu. Single strip triggers were required in matrix detectors used for the mass estimators (M1 and M2 for RANGE 0, and M2 for RANGE 1). No energy limits were placed on E1, the energy deposited in the stopping detector. The radius limits were the nominal detector radii from the

detector specifications.

For the element helium, the mass limits were 1 and 6 amu for all RANGEs. For helium in RANGE 1, retriggering in detector M2 (see Spalding 1983) made some protons have mass measurement errors which made the protons indistinguishable from RANGE 1 helium ions, using the M_{B1} mass estimator. The protons and helium ions were then separated by requiring that $1.0 \leq M_{A1} \leq 6.0$ also hold for RANGE 1 helium.

For iron we could not require single strip triggers in the matrix detectors used for mass estimators and be able to use the hodoscope efficiency calibration of appendix A. The hodoscope efficiency calibration was not extended up to the energies characteristic of iron ions stopping in a matrix detector. Fortunately, signal defects in the matrix detectors for iron events do not lower the mass estimators enough to make it impossible to differentiate between iron and calcium. An iron event in RANGE 0 or RANGE 1 with a signal defect in M1 or M2, still lies above the "track" for calcium events. We then chose mass consistency requirements for "iron" events that excluded calcium events but summed over the charge interval $21 \leq Z \leq 28$. If the SEP abundances were similar to Cameron's 1981 abundance table in this charge region, then this procedure would result in an 8% overestimate of the SEP iron abundance, much less than our experimental errors.

3.8. Element Spectra

Using data from the low resolution data set we computed the spectra of elements He,C,N,O,Ne,Mg,Si, and Fe. During the highest rate time periods, a number of anomalies in the operation of HIST occurred, which are described in Spalding 1983. HIST was operating at counting rates very near to the maximum rates at which it was designed to function correctly, and the causes of all of the high rate anomalies are not completely understood. However, we believe that

we have been able to interpret the data correctly and extract the physically interesting information from the data.

We compute fluxes for time periods that are an integral number of 3 hour time periods. Let the 3 hour time periods be labeled by l. We compute a flux, F_{ijk}, of a given element k, in an energy interval i, and for a time interval j, consisting of 3 hour time intervals from $l = lmin(j)$ to $l = lmax(j)$,

$$F_{ijk} = \frac{\sum_{l=lmin(j)}^{l=lmax(j)} N_{ilk}}{\sum_{l=lmin(j)}^{l=lmax(j)} Denom_{ilk}} . \tag{3.8.1}$$

with

$$Denom_{ilk} = (\Delta E_i)(A\Omega_I)(CORR_{Ilk})(RLT_l)(ERO_{Il}) \tag{3.8.2}$$

where

N_{ilk} = number of events, of element k, in the low resolution data set, in the energy interval i, and the 3 hour time interval l.

ΔE_i = the width of energy interval i, in MeV/nuc.

$A\Omega_I$ = area solid angle geometry factor for RANGE I.

(calculated in Mewaldt (1980))

$I(i)$ = RANGE of energy interval i.

RLT_l = rate live time is seconds, 3 hour time interval l.

For HIZ events, the event read out efficiency is given by,

$$ERO_{Il} = \frac{number\ of\ HIZ\ events\ of\ RANGE\ I}{number\ of\ HIZ\ rate\ counts\ of\ RANGE\ I} .$$

LOZ rate events are not accumulated continuously by RANGE, so for LOZ events,

$$ERO_l = \frac{number\ of\ LOZ\ events}{number\ of\ LOZ\ rate\ counts} .$$

Suppose that the events in interval ilk are labeled by q, then the hodoscope sampling correction for RANGE 0, $CORR_{Ilk}$, is

$$CORR_{Ilk} = \frac{1}{N_{ilk}} \sum_{q=1}^{N_{ilk}} \left[(1 - P_{hodo}(M1,E_{M1}(q)))(1 - P_{hodo}(M2,E_{M2}(q))) \right]^{-1}$$

For RANGE 1,

$$CORR_{j\,i\,k} = \frac{1}{N_{uk}} \sum_{q=1}^{N_{uk}} \left[1 - P_{hodo}(M2, E_{M2}(q)) \right]^{-1}$$

and for RANGEs 2-5,

$$CORR_{j\,i\,k} = 1.0$$

For "iron" events CORR = 1.0.

Here, $P_{hodo}(M1, E_{M1}(q))$ is the probability of a double strip trigger in detector M1, for a particle q that deposited an energy $E_{M1}(q)$ in detector M1. The P_{hodo} function is described in appendix A.

3.9. Fits to the Element Spectra

To determine a spectral form, $f(z)$, with which to compute isotope abundance ratio corrections, we averaged data over the 78:266 flare. For the time period 78:266:10 to 78:272:00 and for elements C, N, O, Ne, Mg, and Si, average fluxes were computed in two energy bins per RANGE, for RANGEs 0 to 4. All six sets of data were fit to a common spectral form by the chisquare technique.

The average flux for element j, between v_{ij} and v_{i+1j} energy/nuc is F_{ij}. The spectral form, $f(z)$, was defined by ten free parameters. The parameters were the value of f, $\{y_i\}$, at 10 points, $\{z_i\}$, equally spaced in log energy from 4 to 60 MeV/nuc. f was interpolated log-linearly between the energy points; if

$$k = integer\ part\ of\ \left[log(z) - log(4) \right]/logdel \qquad (3.9.1)$$

with

$$logdel = (log(60) - log(4))/9 \qquad (3.9.2)$$

then

$$log(f(z)) = \frac{(log(z) - k\ logdel - log(4))}{logdel} (log(y_{k+1}) - log(y_k)) \qquad (3.9.3)$$
$$+ log(y_k)\ .$$

The abundance of each element was normalized to silicon. The fit flux of element j, at energy/nuc z, was given by $\beta_j f(z)$, with $\beta_{Si} = 1.0$. The 15 free parameters, $\{y_i\}$ and $\{\beta_j\}$, were found by minimizing the χ^2 function,

$$\chi^2 = \sum_{j=C}^{Si} \sum_{i=1}^{10} \left(\beta_j g_{ij} - F_{ij}\right)^2 / \sigma_{ij}^2 \quad . \tag{3.9.4}$$

where

$$g_{ij} = \int_{v_{ij}}^{v_{i+1,j}} f(z)\, dz \, / \, (v_{i+1,j} - v_{ij}) \quad . \tag{3.9.5}$$

and σ_{ij} is the statistical uncertainty in the flux F_{ij}.

The data and the resulting fits for all the elements fit are shown in figures 3.9.1a-f. $\beta_j f(z)$ is plotted as a solid line, $\beta_j g_{ij}$ is plotted as a dotted line, and the fluxes F_{ij} are plotted as error bars. The data support the hypothesis of a common spectral form. The main systematic deviations from the fit are the higher energy points of the element silicon, which show higher fluxes than the common spectral form would allow. Figure 3.9.2 shows the data points super-posed, we plotted F_{ij}/β_j vs. energy/nuc to show the common spectral shape.

For the element helium, the fluxes averaged over the 78.266 flare were fit to a spectral form $f(p) = A\, exp(-p/p_o)$, where p is in units of momentum per nucleon, using two free parameters, A and p_o. We found $p_o = 25.54 \pm 0.43$. The fit and data are shown in figure 3.9.3.

These spectral fits were used in section 3.6 to compute isotope abundance correction factors. Fits to the element abundances on a daily basis are reported in section 4.3.

figure 3.9.1a-f - A plot of the average spectral flux, F_{ij}, pei $cm^2 - sr - sec - MeV/nuc$, for the time interval 78:266:10 to 78:272:00. The solid lines are the spectral form, $\beta_j f(E/n)$. The dotted lines are the fit integrated over the experimental energy bins, $\beta_{ji} \eta_{ij}$. The experimental points, F_{ij}, are plotted with error bars.
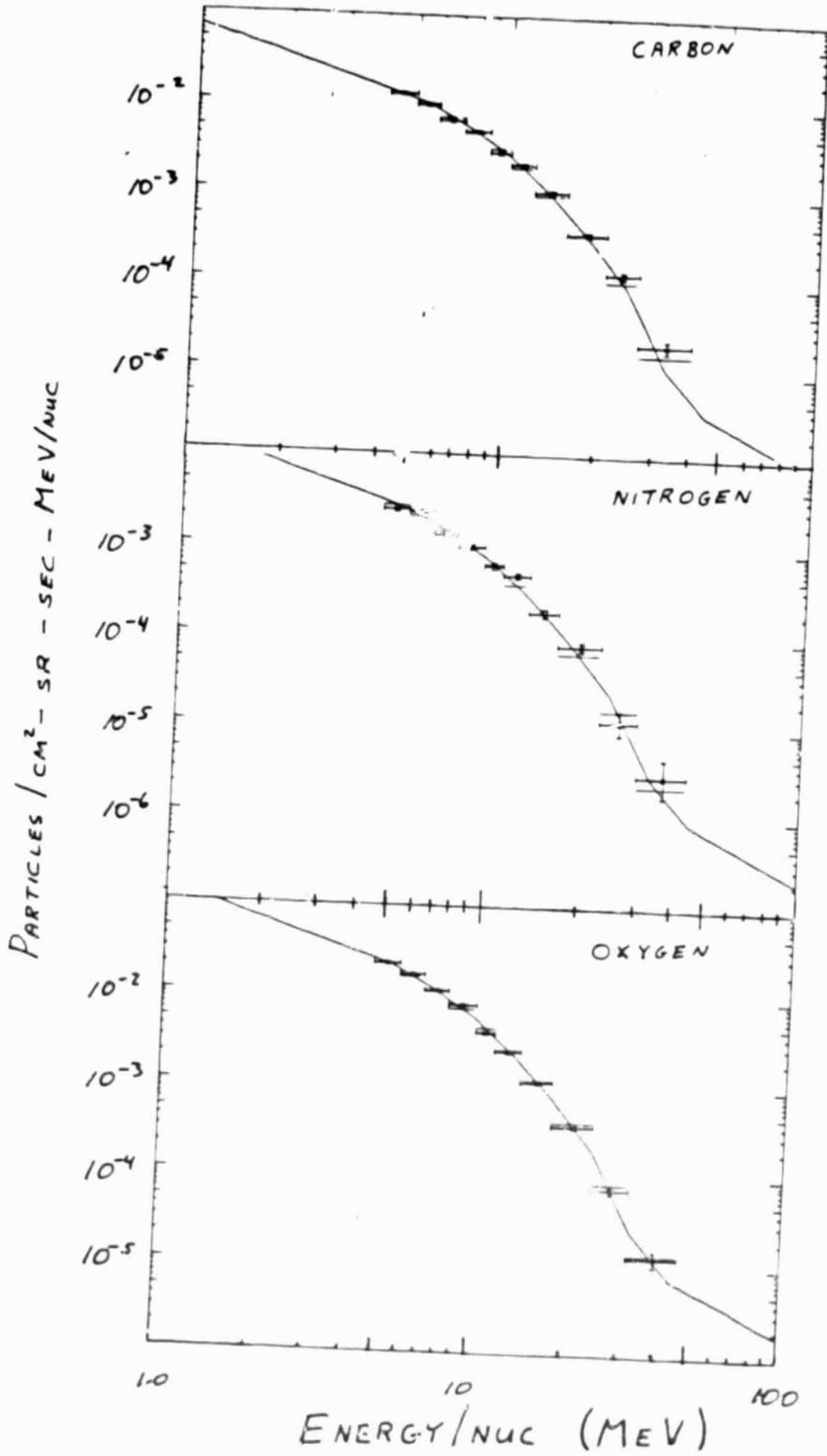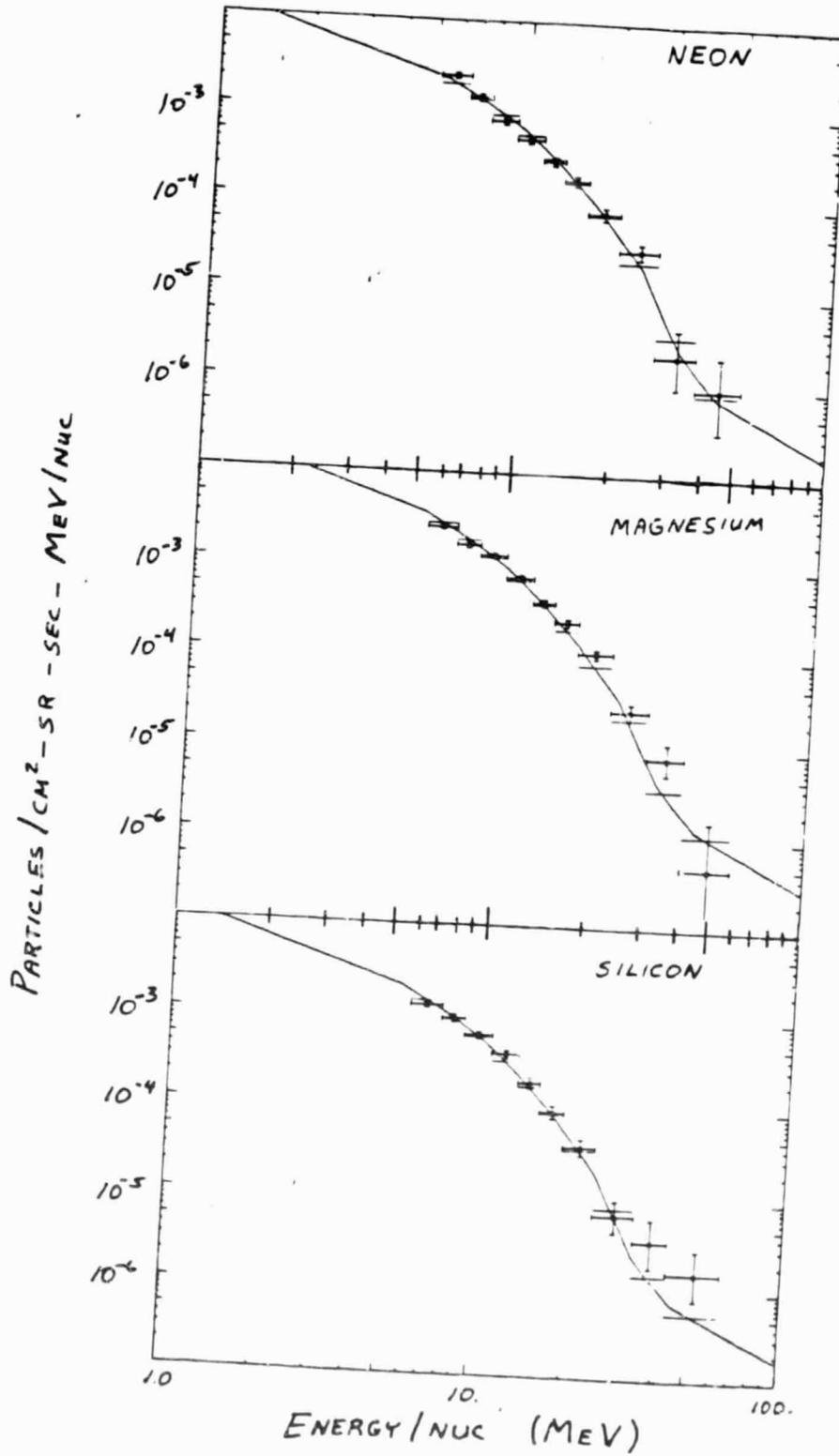
figure 3.9.2 - A plot of the average spectral flux for elements C, N, O, Ne, Mg, and Si, F_{ij}/β_j, for the time interval 78:266:10 to 78:272:00. The fluxes of elements C, N, O, Ne, and Mg are normalized to silicon.
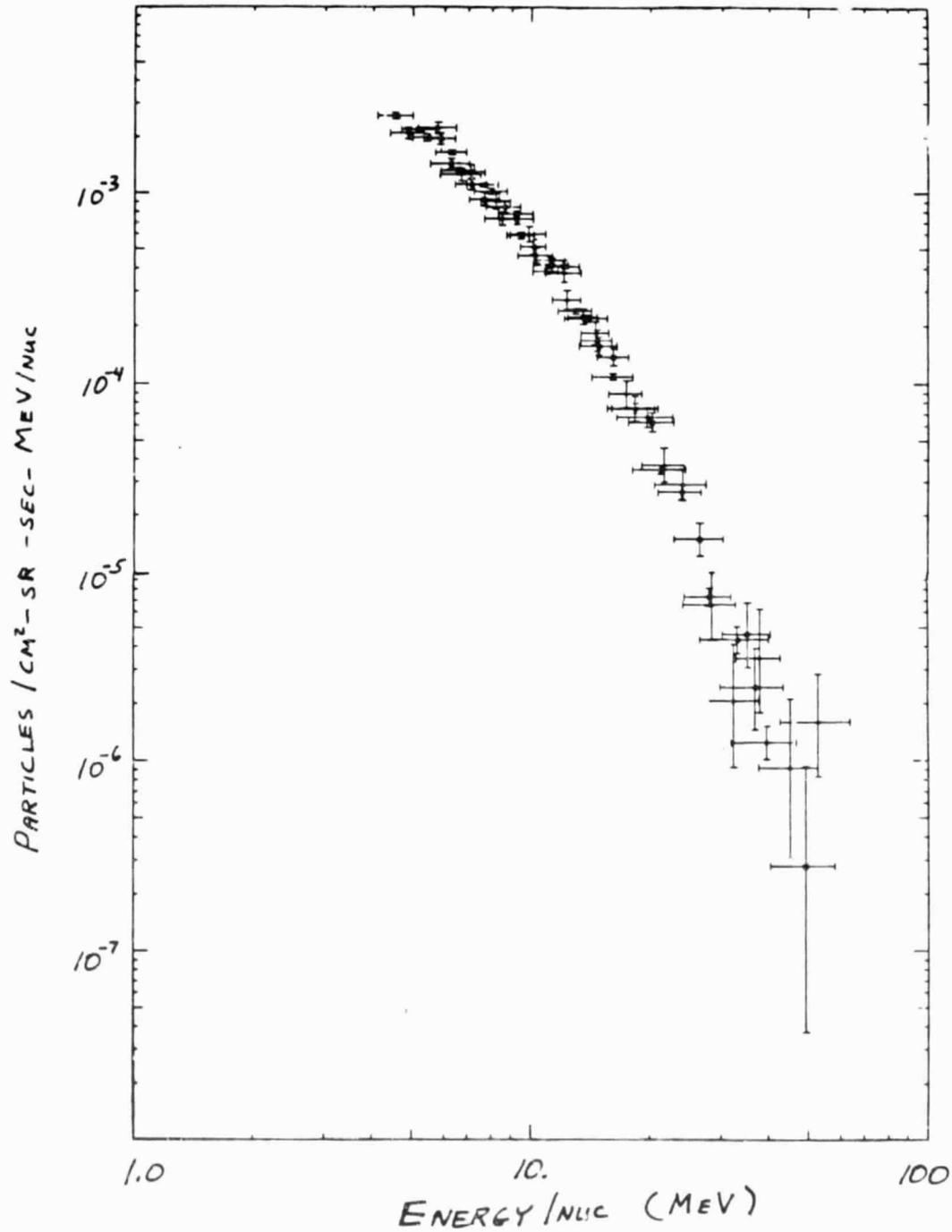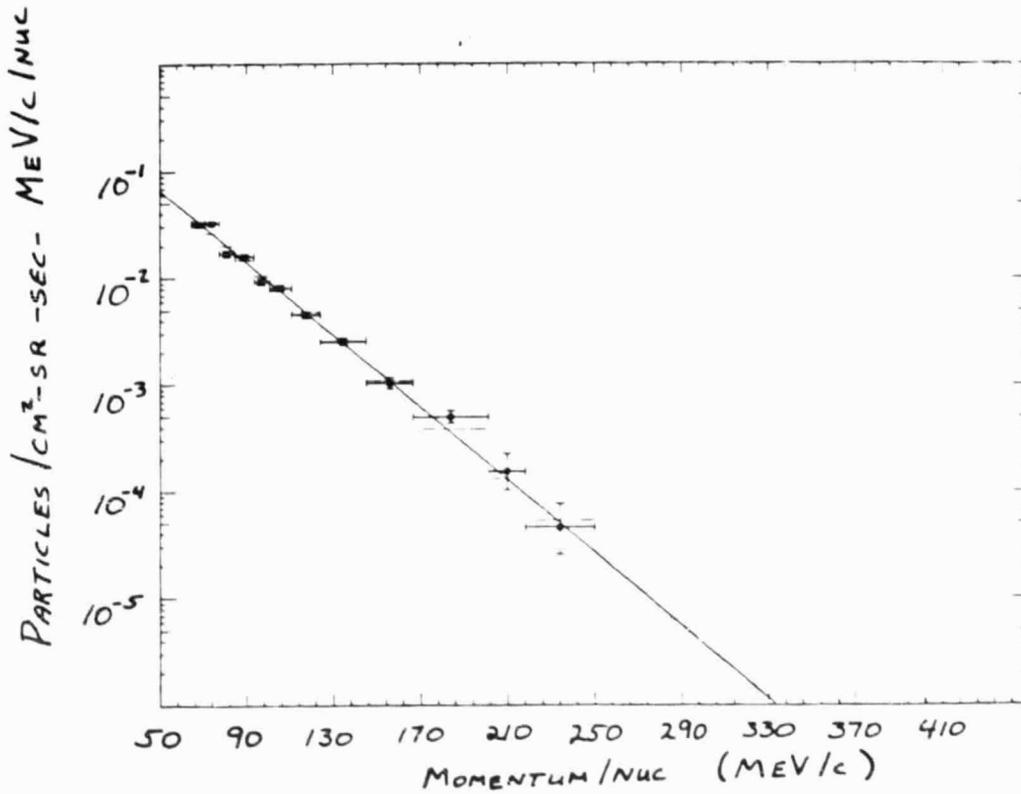
figure 3.9.3 - A plot of the average spectral flux per $cm^2 - sr - sec - (MeV/c)/nuc$, vs. momentum per nucleon for helium, in the time interval 78:266:10 to 78:272:00. The plot symbols are the same as for figure 3.9.1a-f.

Chapter 4 - Observations

4.1. Overview

The HIST instrument was operational from 1978:225 UT to 1978:335 UT. On 1978:335 UT a failure occurred in the digital electronics (see Mewaldt 1980) that read out events into the telemetry stream. The failure made HIST unusable as an isotope spectrometer after 1978:335, using the methods of this thesis. Breneman (1980) has analyzed a methodology that allows one to make measurements with the degraded HIST instrument, at reduced elemental and isotopic resolution, and over more limited energy ranges.

Figures 4.1.1a-c show the HIZ rate, corrected for live time, in RANGEs 0, 2, and 4, for the time interval 78:225 to 78:335. The HIZ rates primarily count C and O nuclei and table 4.1.1 lists the energy intervals for the HIZ rates, assuming that all of the particles incident are oxygen. The carbon energy intervals would be about 15% lower.

Table 4.1.1 -

| | (MeV/nuc) |
RANGE	Oxygen energy interval
0	4.8 - 6.9
1	6.9 - 10.1
2	10.1 - 14.2
3	14.2 - 24.3
4	24.3 - 45.3

In figures 4.1.1a-c there are several sharp increases in the counting rate, or particle events, superposed on a relatively constant background. There are two very small particle events that occur on days 78:278 and 78:283. Two larger events occur starting on days 78:266 and 78:314. All of the measurements reported in this thesis will be from the particle event that begins on day 78:266. The event on day 78:314 has too few particles in its high resolution data set to allow us to make meaningful conclusions about its isotopic composition. For example, for days 78:314 through 78:317, the high resolution data set contains

about 30 RANGE 1, 7 RANGE 2, and 5 RANGE 3 carbon events, compared to almost 900 RANGE 1, 600 RANGE 2, 600 RANGE 3 carbon events for the days 78:266 to 78:272.

Figures 4.1.2a-c show the HIZ rate in RANGEs 0, 2, and 4 for days 78:265 to 78:275. The event is characterized by a fast rise, an almost flat peak, and an exponential decrease. The shape of the particle event is approximately similar in each range, though the rate of decrease after day 78:268 is faster for the higher ranges. All of the isotope and element observations reported in chapter 4 are for the time interval from 78:266:10 to 78:272:00. For that time interval, the RANGE 0 HIZ rate is higher than the levels before and after the particle event by at least a factor of two.

Slightly before the particle event, a large solar flare of importance 3B in H_a was observed on the sun, from 78:266:09:44 to 78:266:12:15. (The data in this paragraph are from the Solar Geophysical Data Bulletin 1979, March, April.) The flaring activity was observed in the McMath plage group 15543, from which other smaller H_a flares were recorded in the time interval from 78:266:05 to 78:269:12. From 78:267:02:07 to 267:02:47 a flare of importance 1N was seen and from 78:267:06:23 to 78:267:06:29 a flare of importance 2B was seen in plage group 15543. The Deep River neutron monitor, with a 1.03 GV geomagnetic cutoff, recorded the onset of a ground level event at about 78:266:10:30. X-rays from 0.5 to 4 A show a sharp increase of a factor of about 600 at 78:266:10 and a smooth decline until 78:266:20. Electrons from 1 to 5 MeV increase from about $5 \times 10^{-3} / cm^2 \, sr \, sec \, MeV$ before the event to a peak of about $2 \times 10^{+1} / cm^2 \, sr \, sec \, MeV$. They remain over $1 \times 10^{+1} / cm^2 \, sr \, sec \, MeV$ until day 78:268, then decrease approximately exponentially to $1 \times 10^{-1} / cm^2 \, sr \, sec \, MeV$ on day 78:272. McMath 15543 was located at 35° N, 50° W on the sun on day 78:266, and at a solar wind speed at earth of

$\approx 350 \, km/sec$, it was well connected by a Parker spiral magnetic field to the Earth.

In figure 4.1.2, there is a sharp decrease in the particle counting rates in the hour before day 78:268, which may be associated with the arrival of a sudden storm commencement on 78:268:07:18 (Solar Geophysical Data Bulletin 1979, March, April). Sudden storm commencements are associated with the arrival at Earth of interplanetary shock waves in the solar wind plasma, travelling from the Sun (Svestka 1976). If the sudden commencement was associated with the 3B flare of 78:266:09:44, then the flare shock travelled at an average speed of 910 km/sec to reach the Earth, fairly typical for a flare shock.

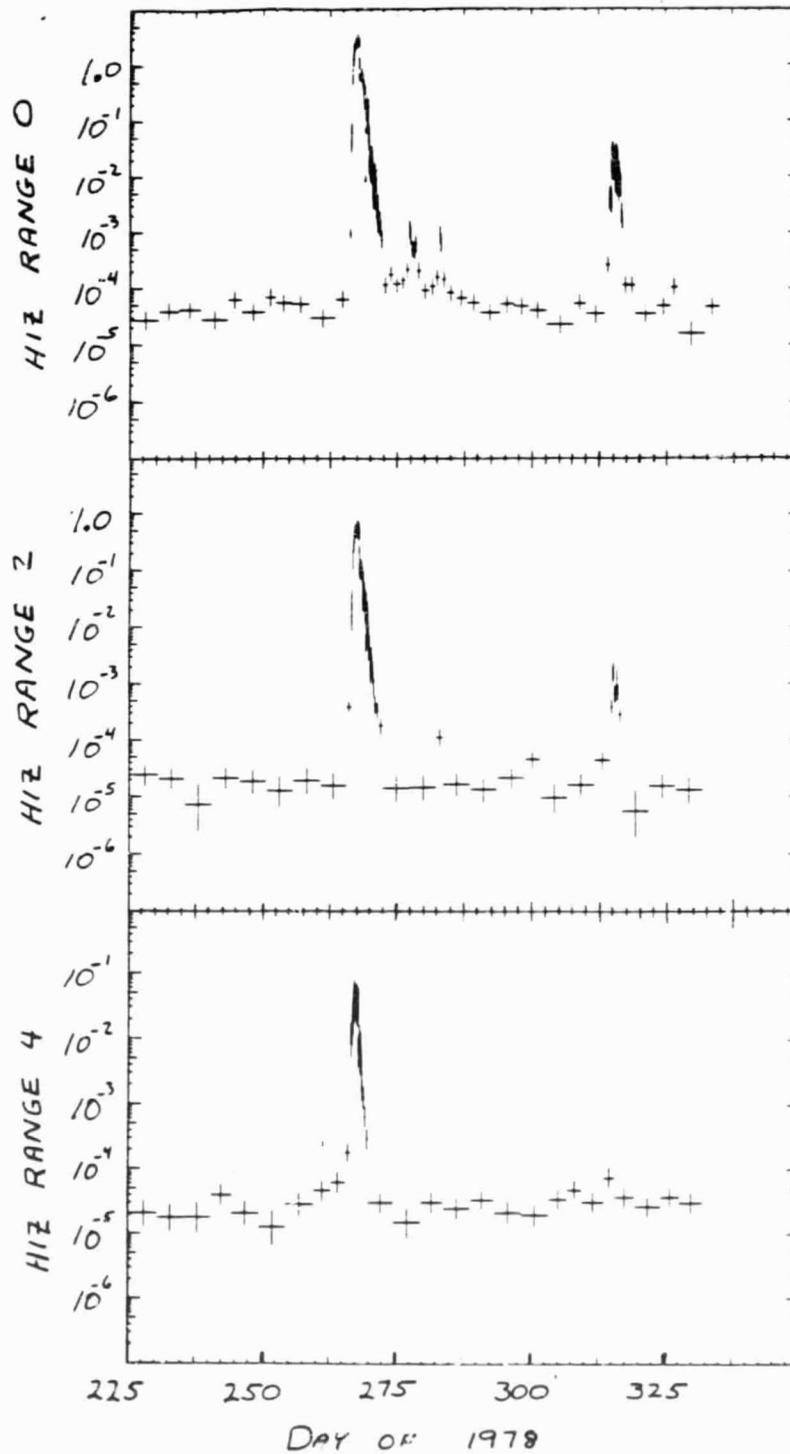All of the above data are consistent with the occurrence of a large solar flare on the Sun.

figure 4.1.1a-c - The HIZ rate for RANGEs 0,2, and 4, corrected for live time, is plotted as a function of time. Figures a,b, and c, correspond to RANGEs 0, 2, and 4, respectively.

figure 4.1.2a-c - The HIZ rate for RANGEs 0,2, and 4, corrected for live time, is plotted as a function of time. Figures a,b, and c, correspond to RANGEs 0, 2, and 4, respectively.
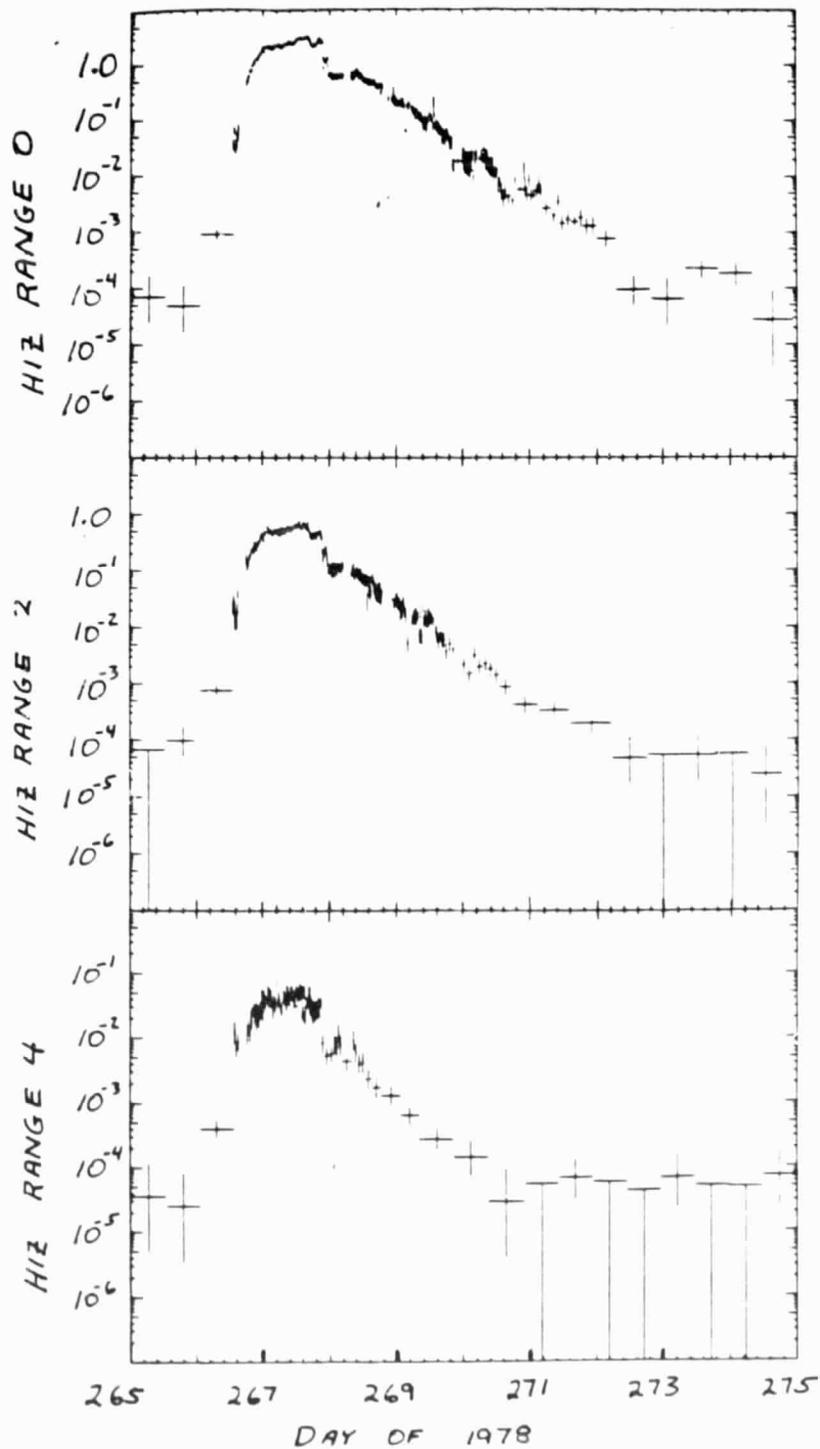
4.2. Isotope Observations

The mass measurements of section 3.4 and the confidence interval calcula-
tions of section 3.5 were corrected for energy per nucleon sampling effects with
the factors of table 3.6.1. The results, for the time interval 266:10 to 272:00, are
shown in table 4.2.1 and plotted in figure 4.2.1. The energy intervals listed in
table 4.2.1 were calculated for the most abundant isotope in the respective iso-
tope abundance ratio. We also list isotope abundance ratios computed from a
compilation of solar system isotope abundances (Cameron 1981). For all of the
isotope ratios for which we report a finite abundance ratio, we see no statisti-
cally significant disagreement with the Cameron compilation.

Table 4.2.1 -

HIST Isotope Ratio Results
(corrected for energy/nuc sampling effects)

Ratio	Observation	(MeV/nuc) Energy Interval	(1980) Cameron value	RANGEs
$^3He/^4He$	≤ 0.0026	4.8 - 32.5	0.00018	RANGEs 2-5
$^3He/^4He$	≤ 0.0175	3.3 - 4.8	0.00018	RANGEs 1
$^{13}C/^{12}C$	0.0095 + 0.0042 - 0.0029	6.2 - 38.7	0.0111	RANGEs 1-4
$^{14}C/^{12}C$	≤ 0.0014	6.2 - 38.7	-----	RANGEs 1-4
$^{15}N/^{14}N$	0.008 + 0.010 - 0.005	7.3 - 42.1	0.0037	RANGEs 1-4
$^{17}O/^{16}O$	≤ 0.0021	6.9 - 45.3	0.00038	RANGEs 1-4
$^{18}O/^{16}O$	0.0015 + 0.0011 -0.0007	6.9 - 45.3	0.0020	RANGEs 1-4
$^{21}Ne/^{20}Ne$	≤ 0.014	11.3 - 51.2	0.0030	RANGEs 2-4
$^{22}Ne/^{20}Ne$	0.109 + 0.026 - 0.019	8.2 - 51.2	0.122	RANGEs 1-4
$^{25}Mg/^{24}Mg$	0.148 + 0.046 - 0.026	12.1 - 55.3	0.128	RANGEs 2-4
$^{26}Mg/^{24}Mg$	0.148 + 0.043 - 0.025	12.1 - 55.3	0.141	RANGEs 2-4

figure 4.2.1 - Isotope abundance results for the 266 flare. Plotted as dashed lines are isotope ratios calculated from the Cameron (1981) compilation.

- 115
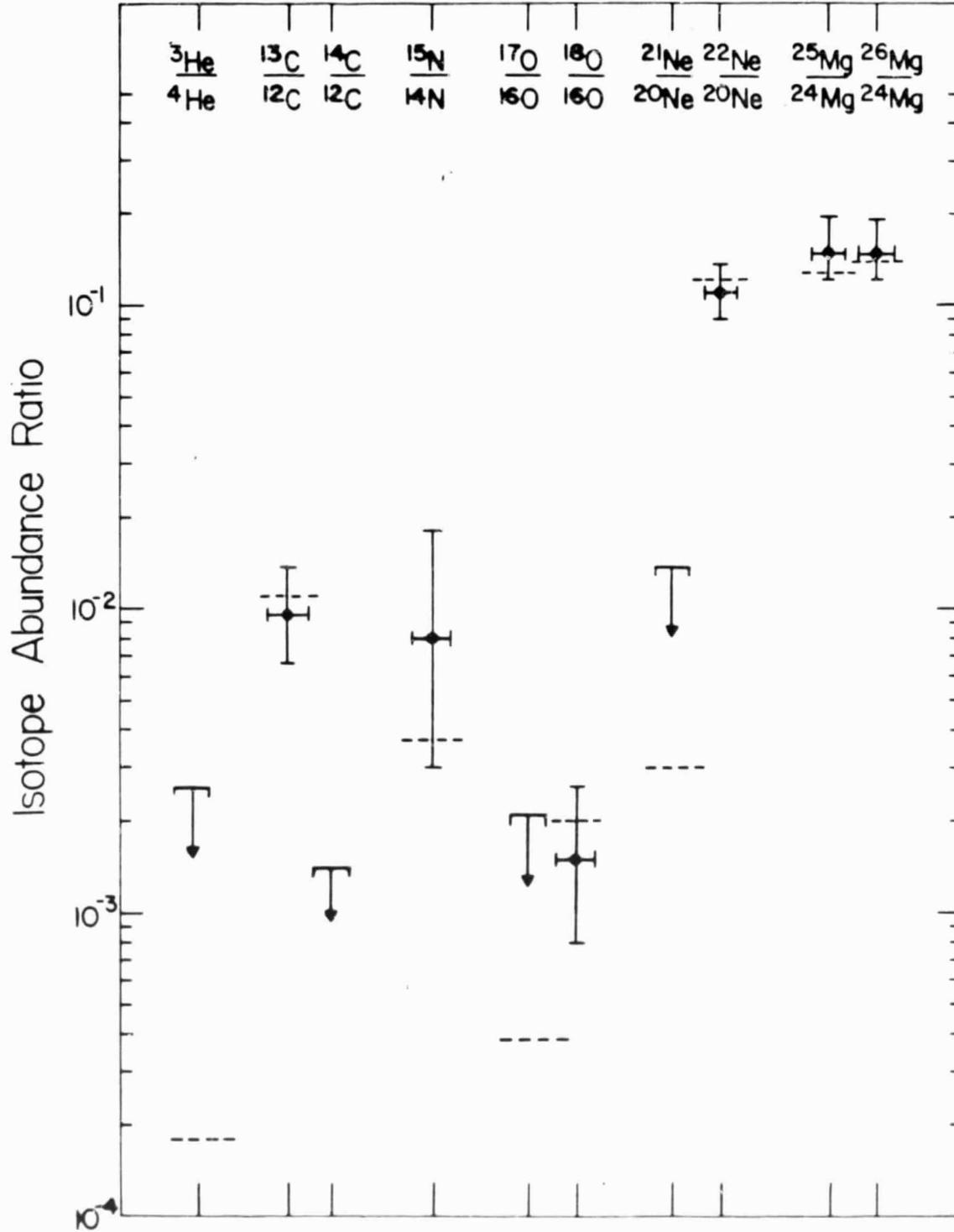
To derive the spectral corrections to the isotope ratios, we had to make the assumption that different isotopes of the same element had the same spectral shape. We can now check this assumption. For the isotope ratios $^{13}C/^{12}C$, $^{18}O/^{16}O$, $^{22}Ne/^{20}Ne$, $^{25}Mg/^{24}Mg$, and $^{26}Mg/^{24}Mg$, the isotope ratio for the time interval 266:10 to 272:00 was computed in each RANGE separately. We plotted the abundance ratio results vs. energy per nucleon in figures 4.2.2a-e. If each isotope, of a given element, had the same spectral shape, then the abundance ratio should stay constant as a function of energy. We see no evidence of a systematic variation with energy of the isotope abundance ratios reported here.

- 116 -

figure 4.2.2a - Isotope abundance ratios are plotted vs. energy per nucleon. Each plotted point corresponds to the results from one RANGE. The horizontal dashed lines and the arrow correspond, respectively, to the confidence limits and most likely values from table 4.2.1.
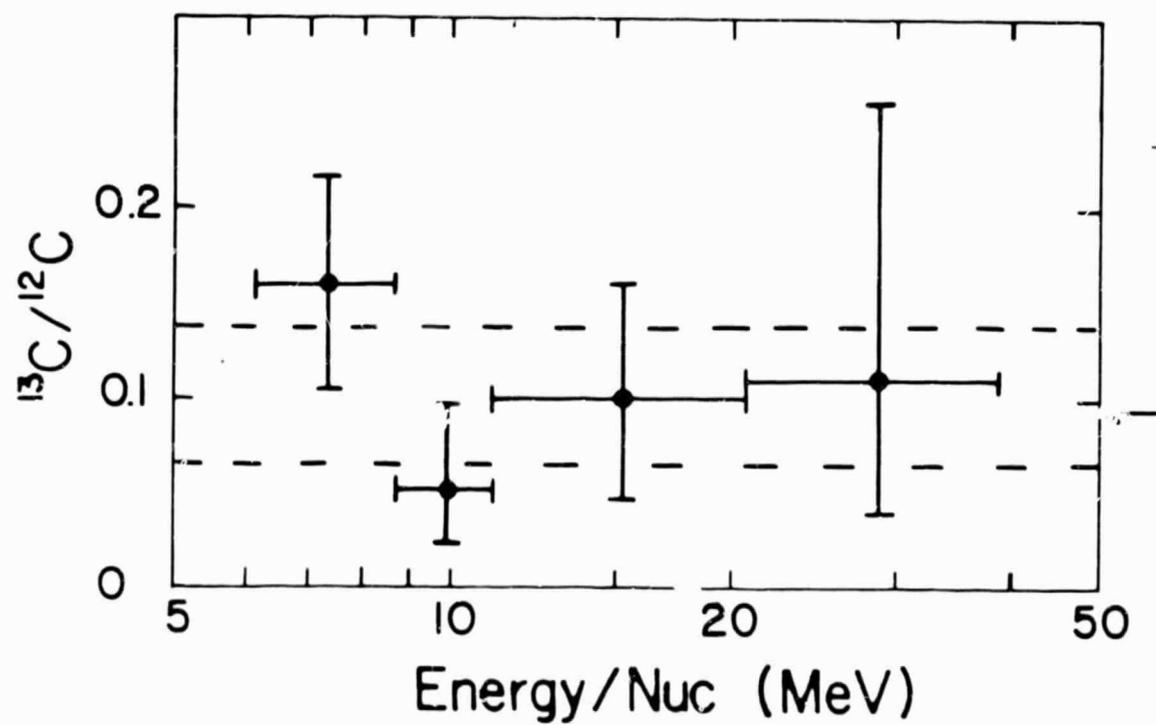
figure 4.2.2b - Isotope abundance ratios are plotted vs. energy per nucleon. Each plotted point corresponds to the results from one RANGE. The horizontal dashed lines and the arrow correspond, respectively, to the confidence limits and most likely values from table 4.2.1. The dashed extensions of the lower error bars for figure 4.2.2b are the "conservative error bars discussed in section 4.2.
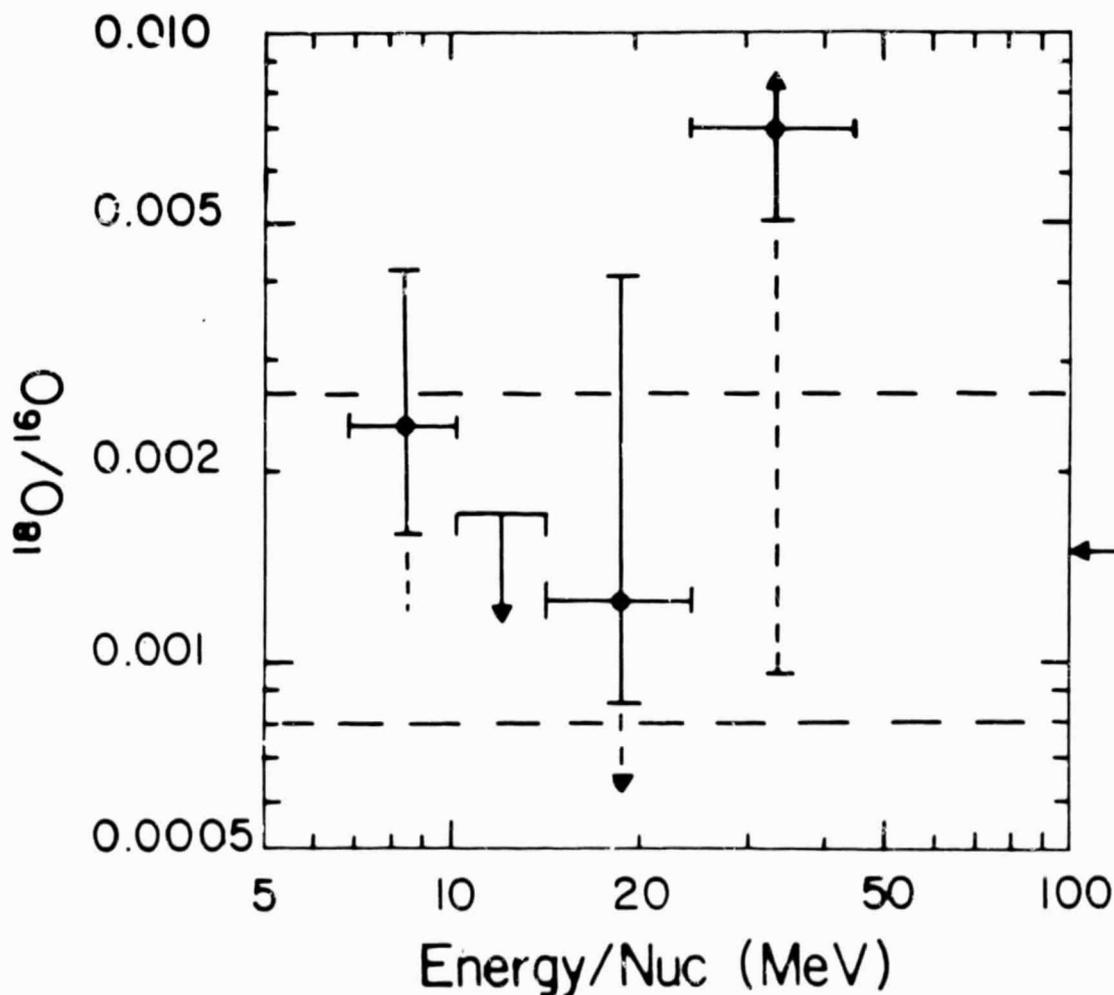
figure 4.2.2c - Isotope abundance ratios are plotted vs. energy per nucleon. Each plotted point corresponds to the results from one RANGE. The horizontal dashed lines and the arrow correspond, respectively, to the confidence limits and most likely values from table 4.2.1.
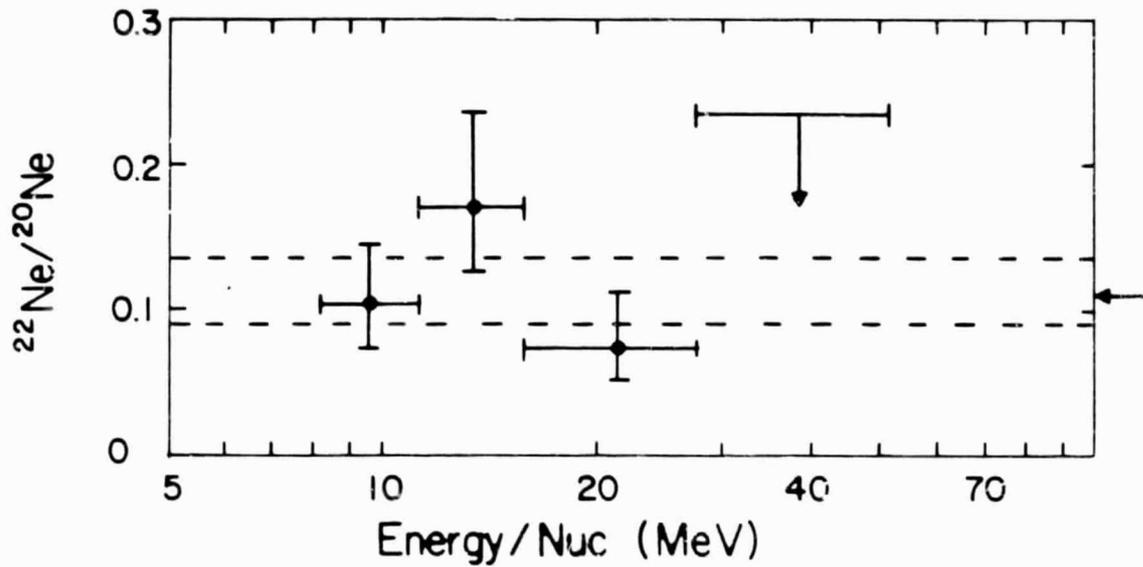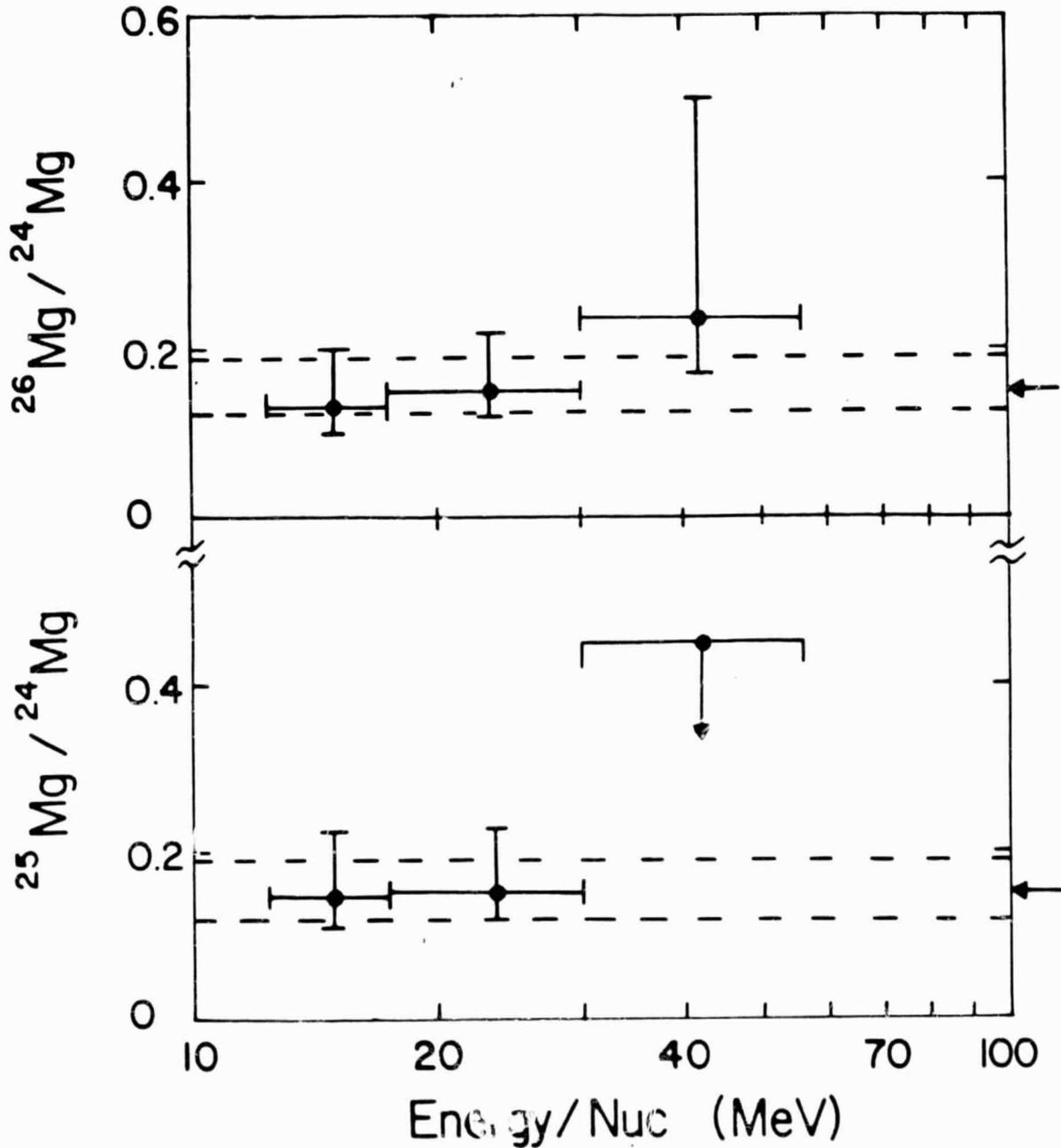
figure 4.2.2d-e - Isotope abundance ratios are plotted vs. energy per nucleon. Each plotted point corresponds to the results from one RANGE. The horizontal dashed lines and the arrow correspond, respectively, to the confidence limits and most likely values from table 4.2.1.

Another assumption of the above analysis was that the isotope abundance ratio is constant as a function of time. $^{13}C/^{12}C$, $^{18}O/^{16}O$, $^{22}Ne/^{20}Ne$, $^{25}Mg/^{24}Mg$, and $^{26}Mg/^{24}Mg$ abundance ratio observations were binned into one day time intervals and plotted vs. time, in figures 4.2.3a-e. Isotope abundance correction factors, calculated using the methods of section 3.6 for an energy/nuc functional dependence, were computed on a daily basis from the daily C-Si fits of section 4.3. If the abundance of one isotope of a given element had a different behavior as a function of time than the abundance of another isotope of the same element, we would see a systematic variation in the plotted isotope ratio as a function of time. If the propagation of the nuclei from sun to earth was rigidity dependent as discussed by Scholer *et al.* (1978) and Witte *et al.* (1979), then we might see all of the heavier isotopes simultaneously enhanced or depleted together at the beginning of the particle event. We see no evidence for time variations of the isotope abundance ratios.

figure 4.2.3a - Isotope ratios are plotted as a function of time. The horizontal dashed lines and the arrow correspond, respectively, to the confidence limits and most likely values from table 4.2.1.

figure 4.2.3b - Isotope ratios are plotted as a function of time. The horizontal dashed lines and the arrow correspond, respectively, to the confidence limits and most likely values from table 4.2.1. The dashed extensions of the lower error bars for figure 4.2.3b are the "conservative error bars discussed in section 4.2.

figure 4.2.3c - Isotope ratios are plotted as a function of time. The horizontal dashed lines and the arrow correspond, respectively, to the confidence limits and most likely values from table 4.2.1.
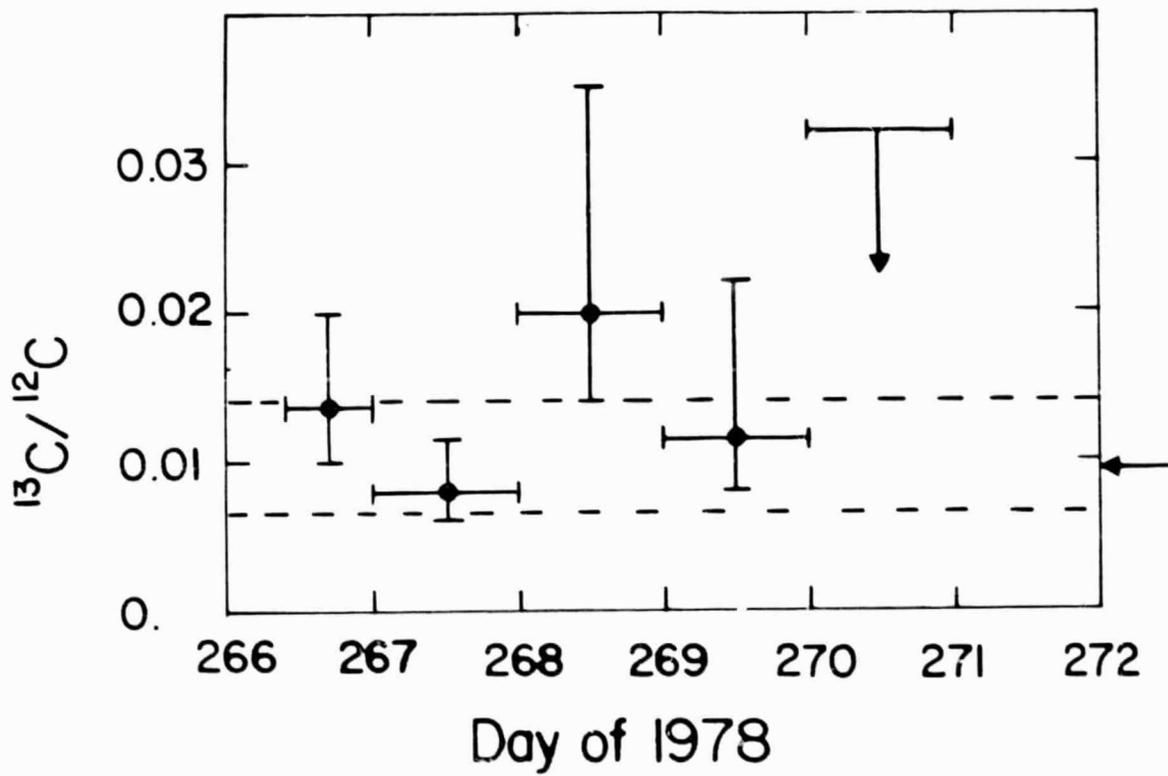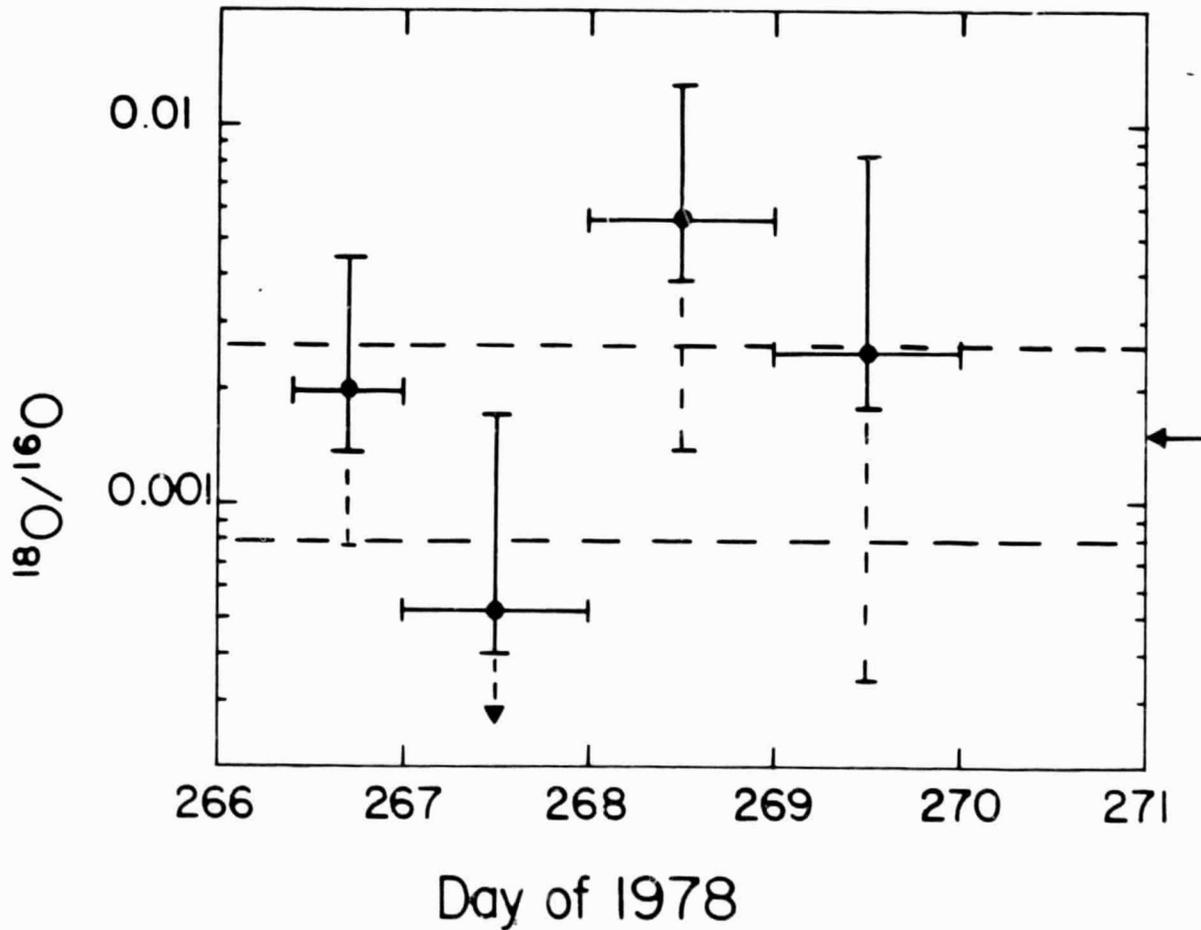
figure 4.2.3d - Isotope ratios are plotted as a function of time. The horizontal dashed lines and the arrow correspond, respectively, to the confidence limits and most likely values from table 4.2.1.

figure 4.2.3e - Isotope ratios are plotted as a function of time. The horizontal dashed lines and the arrow correspond, respectively, to the confidence limits and most likely values from table 4.2.1.
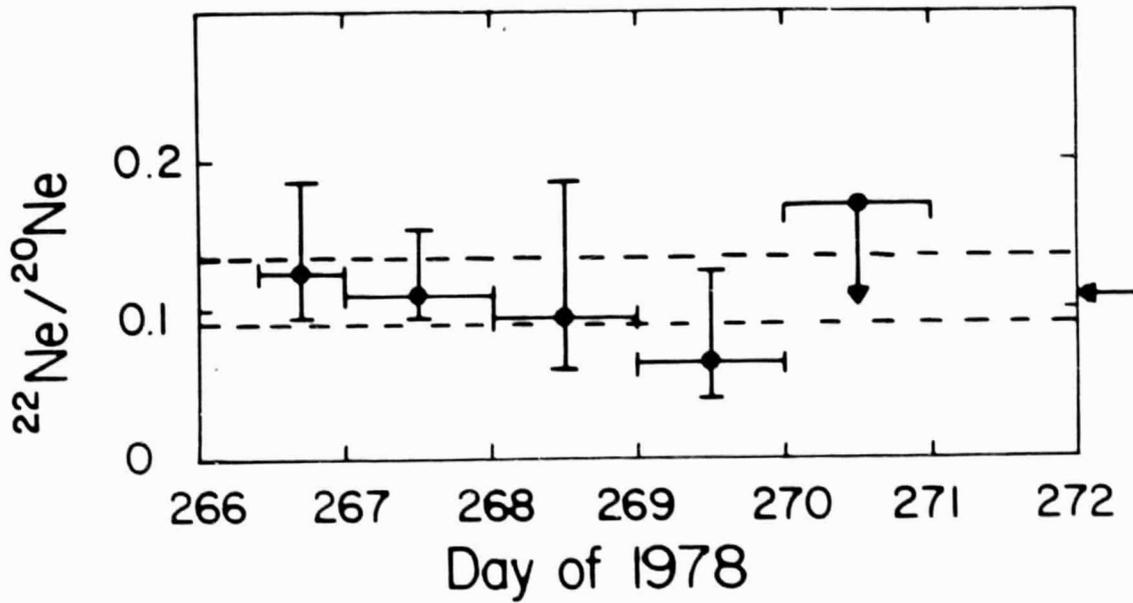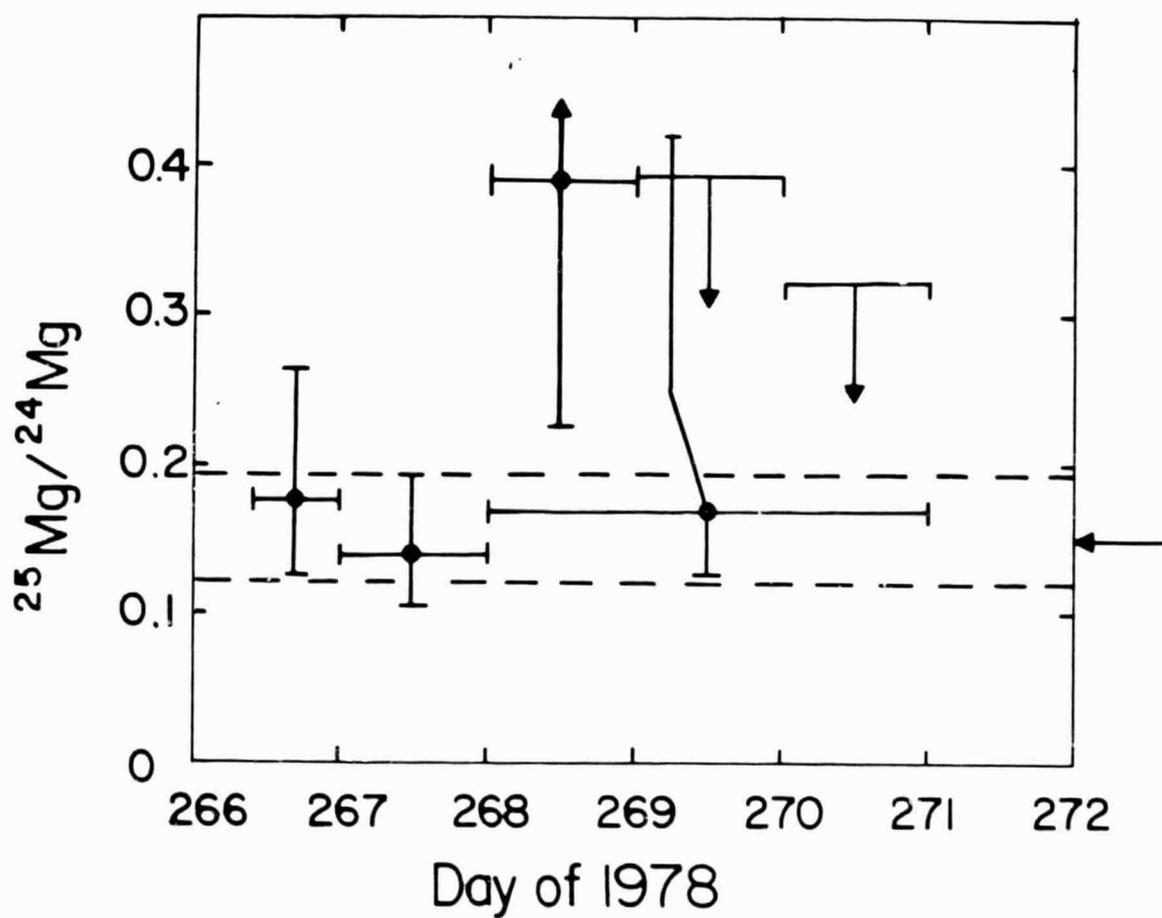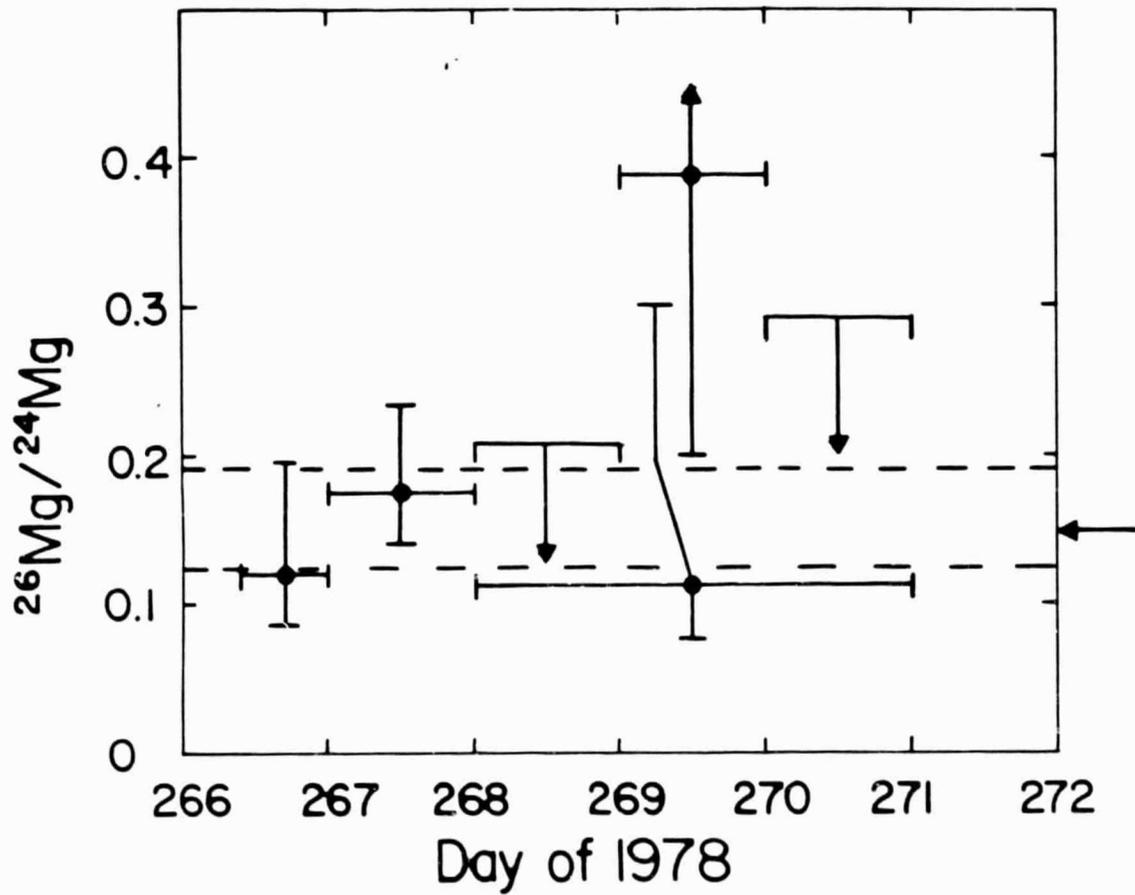
In figures 4.2.2 and 4.2.3 some of the lower error bars are extended by
dashed lines. This is to show the effect of the assumption made in section 3.5
that the abundance ratio is "a *priori*" equally distributed along the real axis.
For a very small number of events ($\leq$ 3) in the numerator of the abundance
ratio, this assumption causes the likelihood confidence integral for the abun-
dance ratio, equation 3.5.2, to be concentrated above the mean value. For
example, on day 266, 2 ^{18}O and 881 ^{16}O nuclei were observed. The value for
$I_a(x)$, where the parameter α is equal to the abundance ratio ^{18}O/^{16}O and for x
equal to 2/881 is $I_a(2/881) = 0.324$.

A more conservative assumption states that the lower error bar for a
parameter α, calculated for a given confidence level C, is the value of α such
that the probability of obtaining more events than are observed is $(1-C)/2$.
The "conservative" upper error bars calculated by this technique are very
nearly equal to the upper error bars calculated by the likelihood technique of
section 3.5. The difference between the two methods for the lower error bars is
largest for a very small number of events in the numerator of the abundance
ratio, and we have only plotted the "conservative" error bars for the oxygen
plots, figures 4.2.2b and 4.2.3b.

4.3. Element Abundance Ratios

The low resolution data set was binned into time intervals of one day and
average fluxes were computed for each day, for the elements C, N, O, Ne, Mg,
and Si. The elements were simultaneously fit to a common spectral form,
$J(p) = \beta_j exp(-p/p_o)$, where p is momentum per nucleon and p_o is a constant,
which is the same for all elements. Table 4.3.1 lists the values of p_o obtained.
The fits were computed by the chi-square technique of section 3.8. Table 4.3.2
shows chi-squared per degree of freedom as computed each day. The results
for day 268 and afterwards show that the hypothesis of a common spectral form

for elements C, N, O, Ne, Mg, and Si produces a good fit to the actual spectral form. Figure 4.3.1 shows the data and the fit for day 268. The error bars for the element fluxes were computed using only statistical considerations. Figure 4.3.2 shows the abundances relative to oxygen obtained by the daily fits as a function of time. The abundances, β_j, on and after day 268 were weighted using the statistical errors obtained in the fit program, and averaged to give a best estimate of the flare element abundance ratios. These values are plotted in figure 4.3.2 as dashed lines and listed in table 4.3.3.

Table 4.3.1 -

Day	p_o (MeV/c)/nuc
78:266	29.22 ± 0.30
78:267	26.25 ± 0.19
78:268	22.44 ± 0.42
78:269	20.09 ± 0.12
78:270	19.36 ± 0.96
78:271	22.13 ± 2.92

Table 4.3.2 -

Day	χ^2	no. points	no. free parameters	χ_ν^2	elements
266	222.2	57	7	4.44	C,N,O,Ne,Mg,Si
267	341.2	56	7	8.98	"
268	43.9	52	7	0.98	"
269	49.4	46	7	1.27	"
270	21.0	35	6	0.73	C,N,O,Ne,Mg
271	4.8	14	3	0.44	C,O

Table 4.3.3 -

Abundance Ratio	Average	Comment
C/O	0.470 ± 0.018	average of C-Si fits, 78:268-272
N/O	0.125 ± 0.009	" 78:268-271
Ne/O	0.132 ± 0.012	" 78:268-271
Mg/O	0.198 ± 0.017	" 78:268-271
Si/O	0.129 ± 0.016	" 78:268-270
He/O	52.8 ± 2.1	average of He/O for RANGEs 2-5, 78:269-272
Fe/O	0.137 ± 0.030	78:268-272 RANGE 0 iron, 8.0-10.4 MeV/nuc
Fe/O	0.073 ± 0.033	RANGE 1 iron, 11.8-16.5 MeV/nuc
Fe/O	0.034 ± 0.033	RANGE 2 iron, 16.5-24.3 MeV/nuc

figure 4.3.1 - C, N, O, Ne, Mg, and Si spectra observed on day 268. The fit to the data, $\beta_j f(p)$, is plotted as a straight line. The fit integrated over the energy limits of the data points, $\beta_j g_{ij}$, is plotted as a dotted line. The data points are plotted as error bars. The flux is in units of $(cm^2 \, sr \cdot sec \, (MeV/c)/ nuc)^{-1}$.
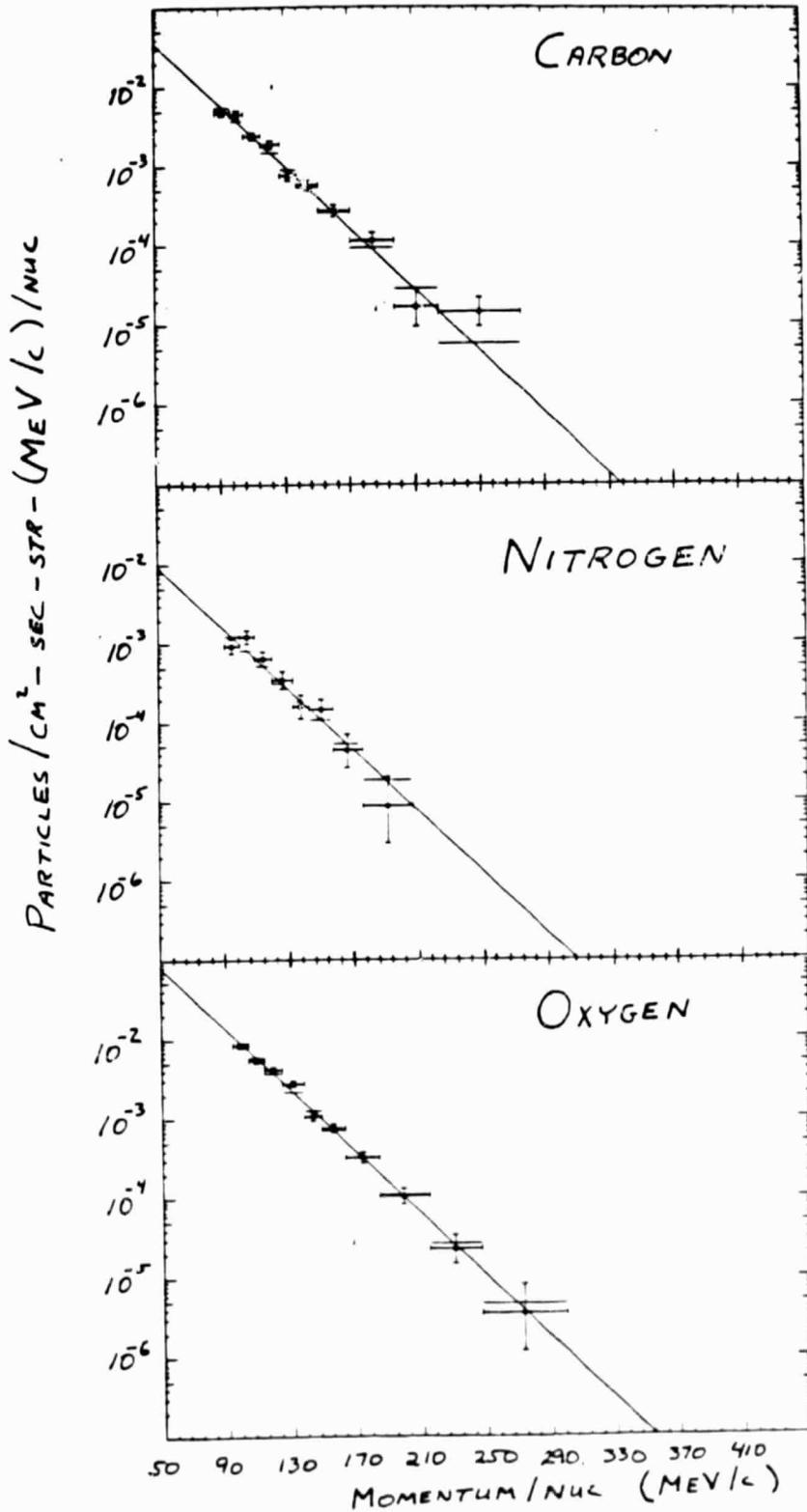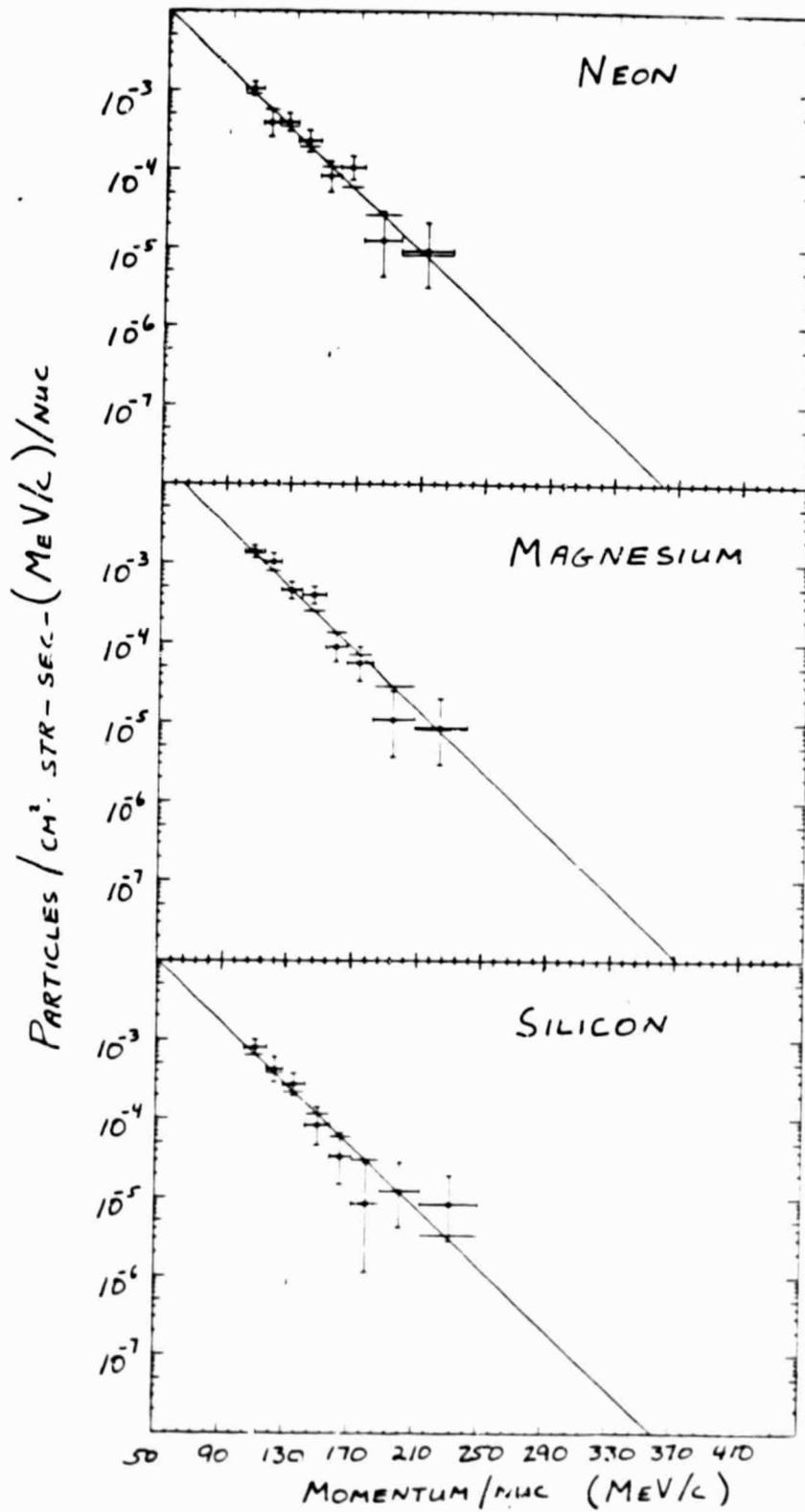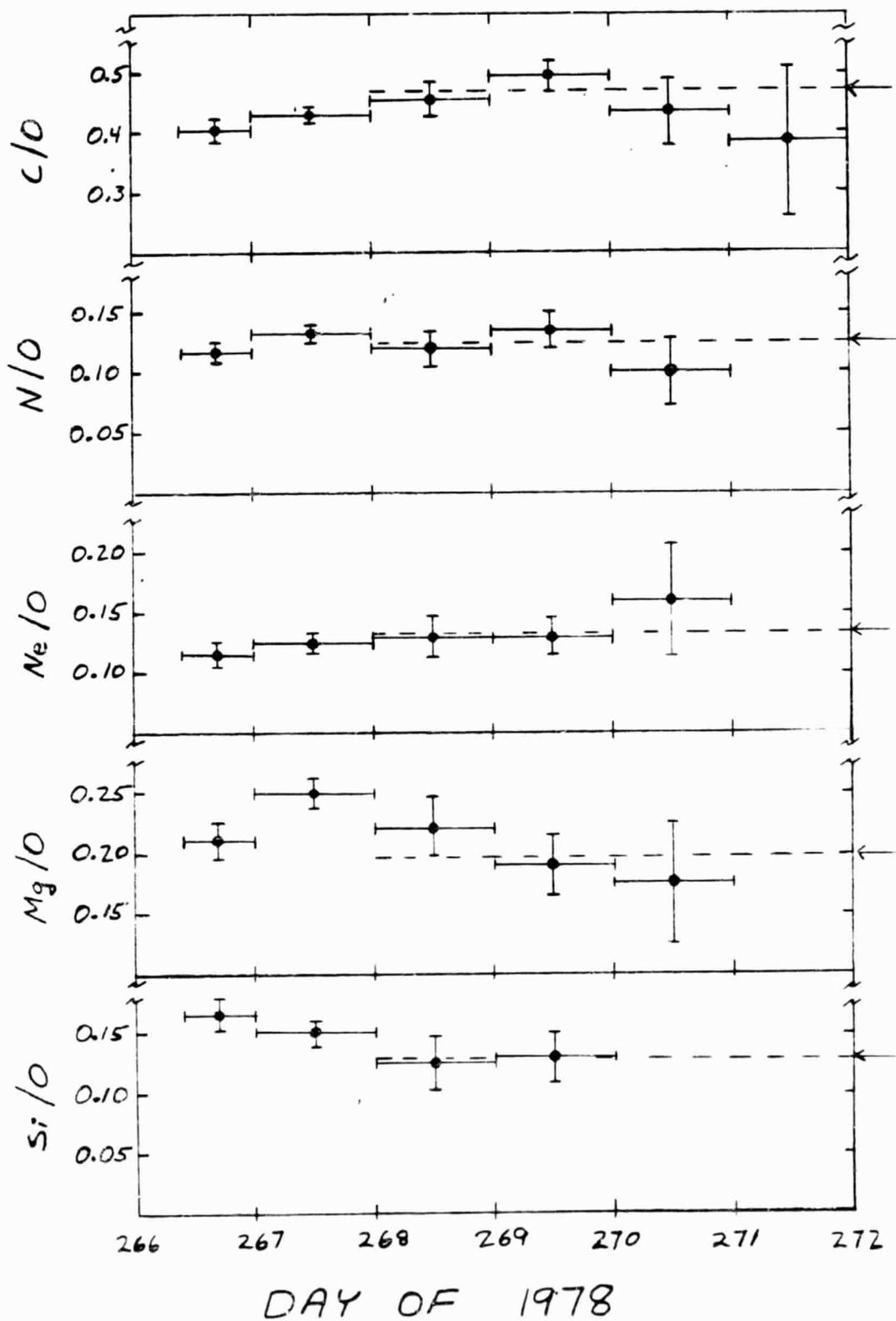
figure 4.2.2 - Abundances relative to oxygen from the C-Si fit, β_j, plotted as a function of time. The dashed lines are averages of the plotted points on and after day 268.

DAY OF 1978

Helium, especially for days 266 and 267, did not show the same spectral shape as the elements carbon through silicon. To obtain a value for the He/O abundance ratio, we integrated the oxygen spectra obtained in the C-Si analysis over the energy intervals corresponding to each RANGE for helium. Thus we obtained an "oxygen" fit flux in each RANGE and for each day that could be directly compared to the helium flux. For greater statistical accuracy, pairs of RANGEs were combined to obtain energy intervals of $2.3 - 4.8$ MeV/nuc for RANGEs 0-1, $4.8 - 11.3$ MeV/nuc for RANGEs 2-3, and $11.3 - 32.5$ MeV/nuc for RANGEs 4-5. The data in the C-Si fits do not extend below about 4.5 MeV/nuc for oxygen, so the RANGEs 0-1 He/O abundance ratios are based on an extrapolation of the C-Si fit to lower energies.

The results obtained are plotted vs. time in figure 4.3.3. The He/O abundance ratio varies at the beginning of the particle event and is relatively constant after day 269. For a best estimate of the He/O abundance ratio we averaged the abundance ratios in RANGEs 2-5 and for days 269-271 to obtain a value of $He/O = 52.8 \pm 2.1$. This value is plotted in figure 4.3.3 as a dashed line and listed in table 4.3.3.

figure 4.3.3 - He/O abundance ratios are plotted vs. time in three energy intervals.
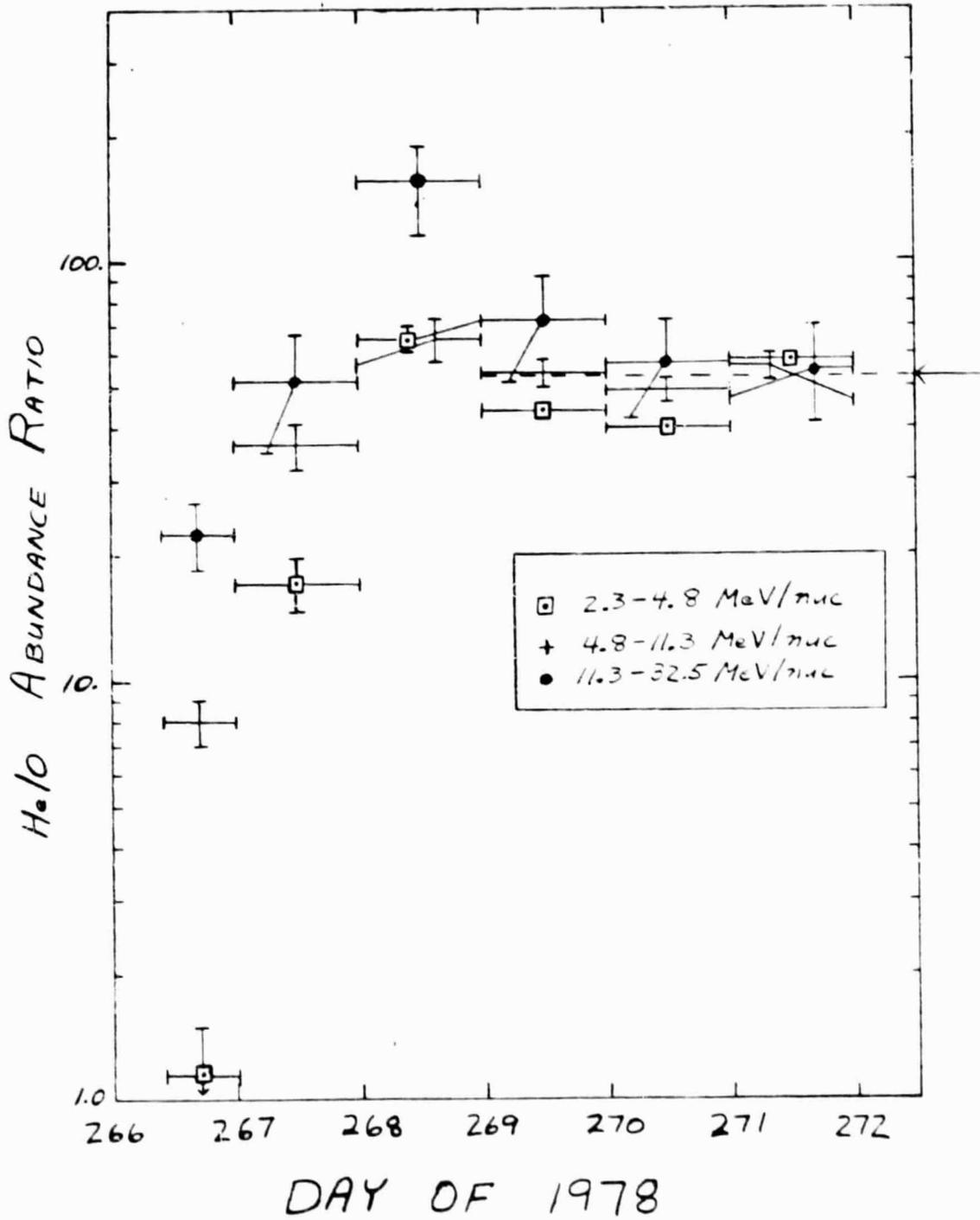
Iron does not show the same spectral shape as the C-Si elements. Cook (1981) has also observed large flares in which the iron spectral shape was significantly different than for the C-Si elements. For each RANGE and each day, iron fluxes were divided by the "O" fluxes from the C-Si fits, to form Fe/O abundance ratios. The Fe/O abundance ratios are plotted vs. time in figure 4.3.4. The points for day 266 have a higher value for Fe/O than does the rest of the data set. We averaged the Fe/O abundance ratio results on and after day 268 in RANGEs 0-2. We find that for RANGE 0, $Fe/O = 0.137 \pm 0.030$, RANGE 1 has $Fe/O = 0.073 \pm 0.033$, and RANGE 2 has $Fe/O = 0.034 \pm 0.033$. These results are not statistically consistent with a common value for the Fe/O abundance ratio. The Fe/O values are listed in table 4.3.3.

figure 4.3.4 - Fe/O abundance ratios in each RANGE are plotted vs. time. The data points shown as crosses are from RANGE 0, 8 – 10.4 *MeV/nuc*, and the points shown as solid circles are from RANGE 1, 11.8 – 16.5 *MeV/nuc*. The points shown as Xs are from RANGE 2, 16.5 – 24.3 *MeV/nuc*, and the points shown as open squares are from RANGE 3, 24.3 – 43.5 *MeV/nuc*.
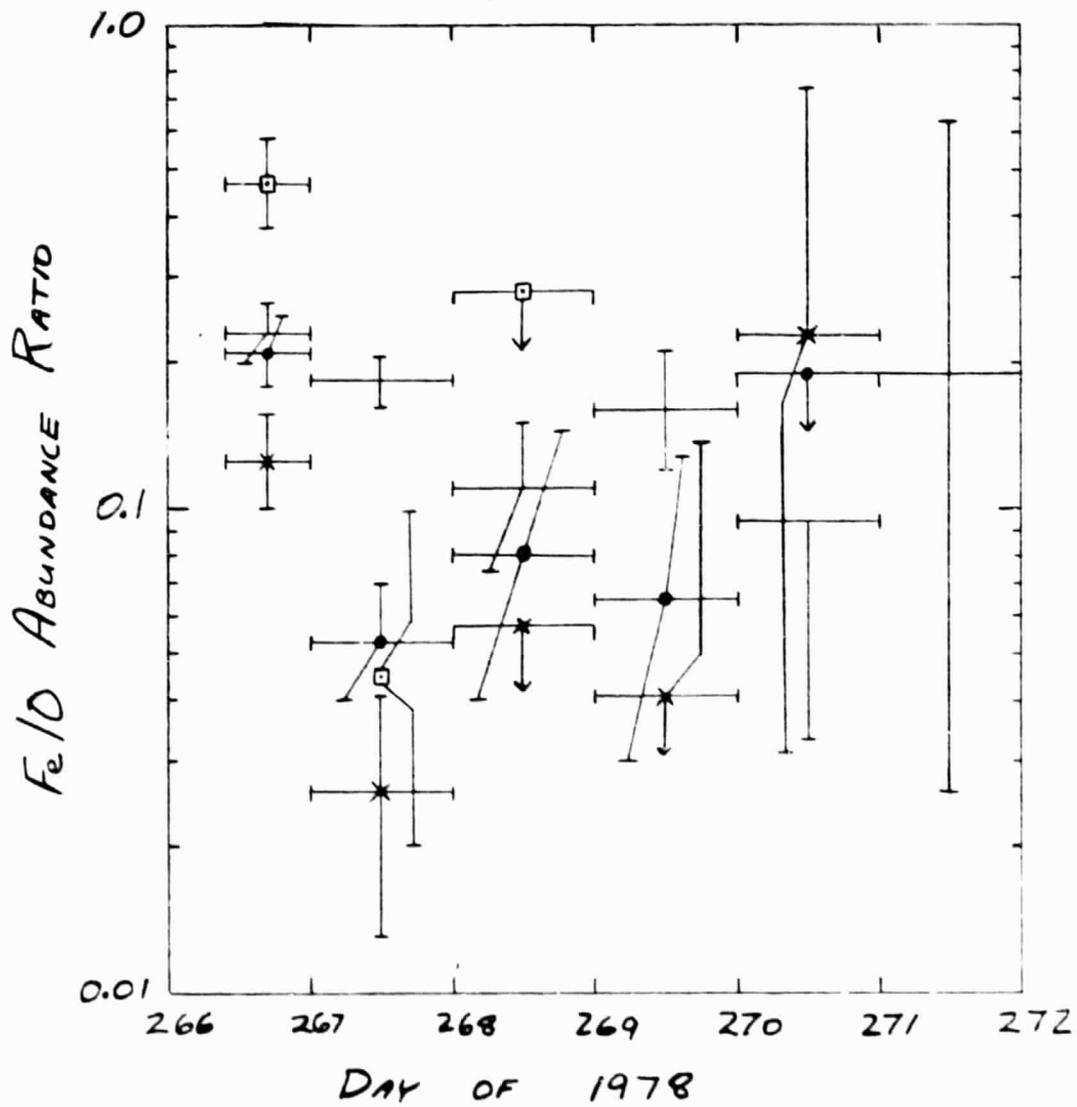
Chapter 5 - Discussion

5.1. Overview

In the following section we will review the observations of element abundances in SEP events. We will show that the 78:266 SEP event has an elemental composition that is similar to other large SEP events. We will review the element abundance variations and average values observed in large SEP events and speculate about plausible consequences for isotope abundance ratios.

In the third through fifth sections we will review the evidence about the Sun's composition that comes from the observation of solar electromagnetic and particle emissions, for the elements He, C, N, O, Ne, and Mg. In the sixth section we will review noble gas meteoritic composition and summarize the data from sections 3 through 5, in order to compare SEP and solar isotope abundances. In section seven we will present our conclusions about the spectral corrections to the isotope abundance ratios.

5.2. Solar Energetic Particle Elemental Composition

The elemental composition of large SEP events has been observed to vary from flare to flare. Since our measurements in this work are limited to one large solar flare, we must use other reported solar flare energetic particle measurements to establish a context for our observations of the isotopic composition of solar energetic particles. The elemental composition and size of the 78:266 flare and its location on the sun, well connected to the earth by Parker magnetic field lines, place it into a well studied class of the largest solar energetic particle events. The study of a sample of the largest SEP events may provide the best estimate of SEP abundances. Mason et al. (1980) measured a number of element abundance ratios in a large data set consisting of daily averages for the period Oct. 30, 1973 to Dec. 1, 1977, in the energy ranges 0.6-

1.6 MeV/nuc for H, He, C, and O, and 1-4.6 MeV/nuc for O, Ne, Mg, Si, S-Ca, and Fe. They find that the abundance ratio variation increases with decreasing flux levels.

Cook (1981) and Cook *et al.* (1980) have studied seven large solar energetic particle events. For four events for which the composition and spectral shape are relatively constant with time, Cook (1981) constructed a four flare SEP (solar energetic particle) abundance average, SEP(Cook), quoted in table 5.2.1. Figure 5.2.1, from Cook (1981), shows the element abundances measured in each of the four flares used in the four flare average, relative to the SEP(Cook) average. The deviation of the element abundances for each individual flare about the four flare SEP(Cook) average, for elements with $6 \leq Z \leq 28$, was systematic and monotonic. For element abundances normalized to silicon, the abundance of the element group C, N, and O, was observed to be anticorrelated with the abundance of the element group Fe and Ni. McGuire *et al.* (1979) observed a similar pattern of elemental abundances when comparing SEP event abundances with a set of average abundances constructed from SEP events with low (iron group)/O abundances. Meyer (1981a,b) has attempted to use all available data on SEP composition between 1 and 20 MeV/nuc to obtain a "mass unbiased baseline". Meyer parametrized the data by the Fe/O abundance observed, and then selected a particular value of Fe/O so that the abundance ratio, SEP/photosphere, for Fe, was approximately equal to the SEP/photosphere abundance ratio for Mg and Si. Fe, Mg, and Si all have similar first ionization potentials. The average element abundances of 5 event classes,

figure 5.2.1 - (from Cook (1981)) The elemental abundances for four solar
flares divided by the average abundance for the four flares, SEP(Cook), is
plotted vs. atomic number. The elemental abundances are given relative to
the abundance of silicon.
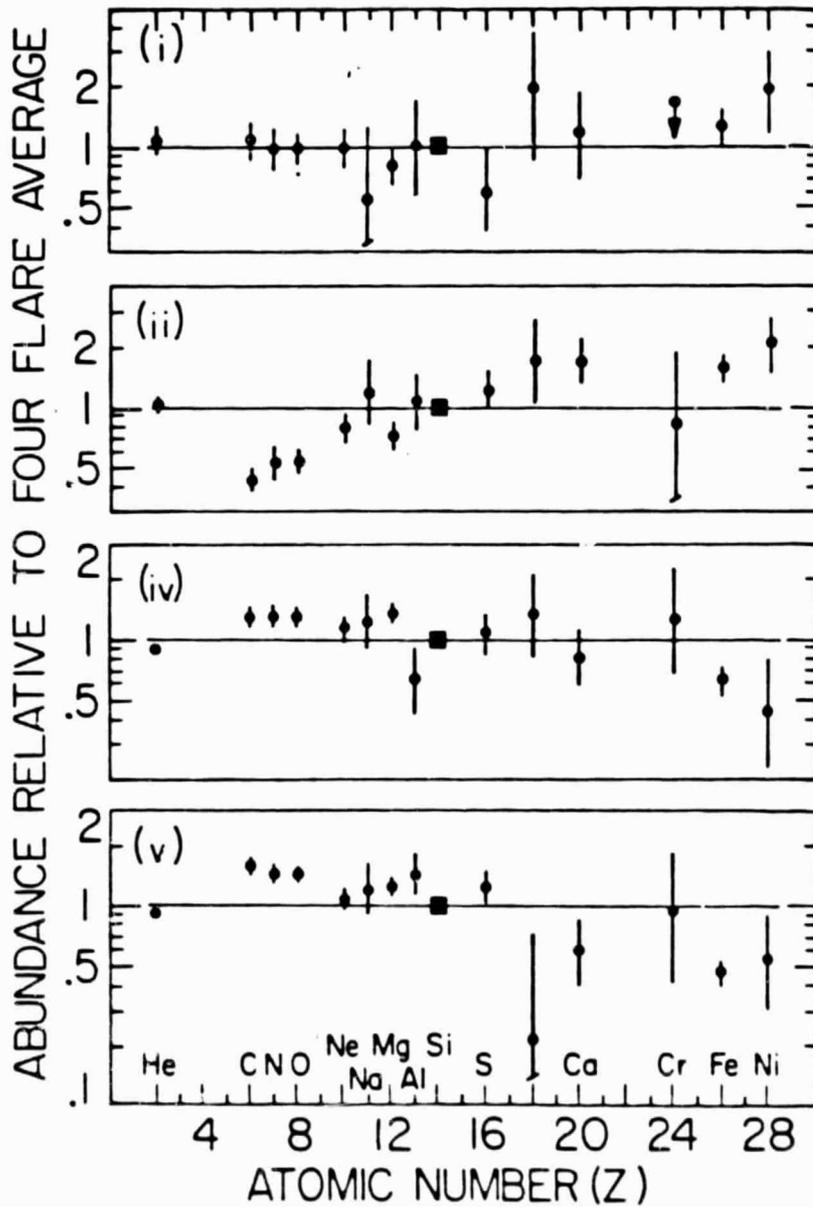
ordered by their Fe/O abundance ratio, deviate in a smooth monotonic fashion from the "mass unbiased baseline" element abundances.

Webber (1975) first noticed a systematic difference between SEP element abundances and the elemental abundances of the solar photosphere. Webber showe. that the element abundance ratio SEP/photosphere was correlated with the element's first ionization potential. Cook and Meyer have confirmed this behavior with their SEP abundance averages. Figure 5.2.2 from Cook (1981) shows the element abundance ratio SEP/photosphere plotted vs. first ionization potential. The SEP(Cook)/photosphere ratio is of the order of 1 or larger, for elements with first ionization potential, I, less than 10 eV (including Ni, Fe, Ms, Si). The SEP/photosphere ratio is less than one half for elements with I > 10eV (including C, N, O, He, Ne, Ar). McGuire et $al.$ have noticed a similar behavior for their sample of flares which have low Fe/O abundances. Another possibility that has been suggested for the correlation between the SEP/photosphere abundance ratio and the first ionization potential, is a systematic error in the photospheric abundances, organized by I (see eg. Mcguire et $al.$ 1979).

Cook (1981) in analysis confirmed by Meyer (1981b) has shown that the SEP element abundance pattern is more similar to the element abundances observed for the solar corona and solar wind than to the photosphere. Figure 5.2.3, from Cook (1981), shows the ratios of the SEP(Cook) element abundances to the element abundances in the photosphere, corona and solar wind Cook has stated the hypothesis that the reason solar wind, coronal and SEP average abundances are similar, is that the solar wind and SEPs are accelerated coronal material and that coronal elemental abundances are significantly different from element abundances in the photosphere. Further evidence supporting this hypothesis consists of the charge states of heavy ions observed in the solar wind (Bame et $al.$ 1979), the charge states c. low energy SEPs of $\approx$ 10 to 600

KeV/nuc (Sciambi *et al.* 1977 and Gloekler *et al.* 1976),

figure 5.2.2 - (from Cook (1981)) SEP elemental abundances divided by solar photospheric or "Local Galactic" abundances of Meyer (1979) are plotted vs. the first ionization potential.
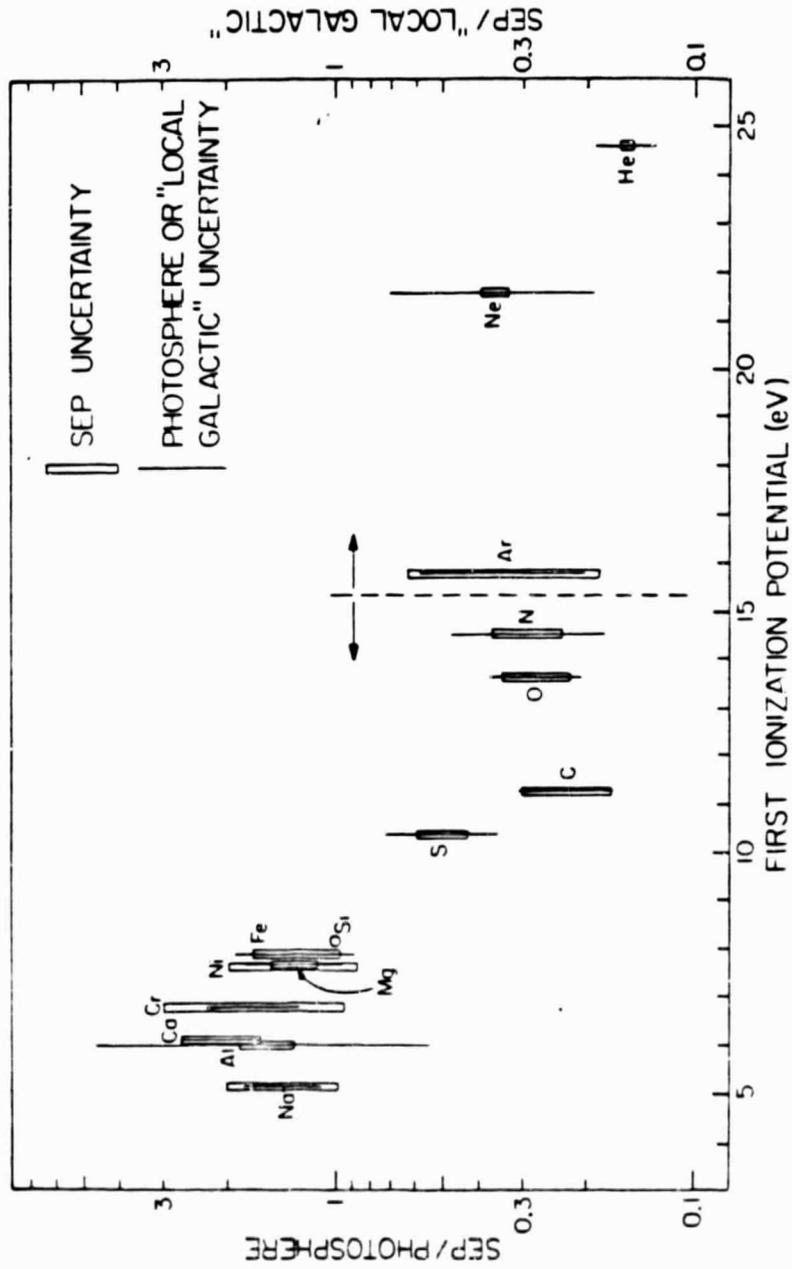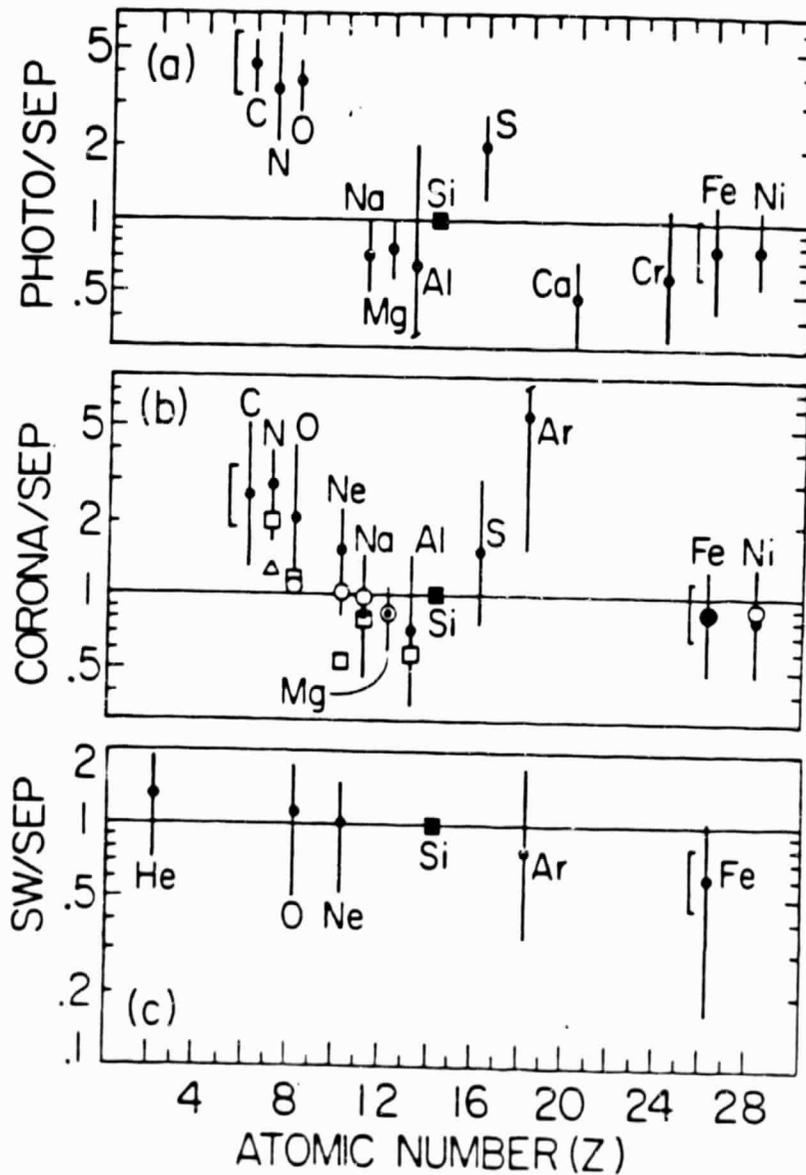
figure 5.2.3 - (from Cook(1981)) The four flare SEP elemental abundances
SEP(Cook) are compared to photospheric, coronal, and solar wind elemen-
tal compositions.

and the charge states indirectly inferred for SEPs of 0.5 to 5 MeV/nuc (O'Gallagher *et al.* 1976). The most consistent explanation of the charge states observed is that matter accelerated to solar wind or solar energetic particle energies was once in collisional equilibrium with a gas that had a temperature of about $1-2 \times 10^6$ °K. This temperature is about the same as observed in the corona (Athay 1976), and different from the temperature of the photospheric minimum, which is about 5×10^3 °K.

The pathlength of material that SEPs have traversed from acceleration to observation, as revealed by nuclear fragmentation, is consistent with the suggestion that the corona is the SEP particle source. McGuire *et al.* (1979) set a limit of 0.06 g/cm^2 from observations of the SEP $^2H/H$ abundance ratio and Cook(1981) reports upper limits to B and F abundances that are consistent with the grammage reported in McGuire *et al.* (1979)

If the corona is the source of SEPs and the solar wind, what conclusions might we draw for isotope observations? Since the difference between the photosphere and corona or SEP abundance averages seem to be organized by first ionization potential, the process that differentiates the elemental abundances of the corona from those of the photosphere may be influenced primarily by whether a given ion is neutral or singly charged in the environment where the differentiation takes place. A way to explain the correlation of SEP/photosphere with I, is to assume that elements with $I > 10eV$ are neutral and elements with $I < 10eV$ are singly charged, which might imply that the efficiency of transport from photosphere to corona for neutral atoms is 25% to 40% of the transport efficiency for ions (Meyer 1981b).

Ni, Fe, Mg, and Si all have $I \approx 8eV$ and thus might be singly charged in Meyer's picture of the transport process from photosphere to corona. Ni, Fe, Mg, and Si, all have about the same ratio of SEP/photosphere elemental abun-

dances. If the mass of the ion was important to the transport process from photosphere to corona, then we might expect to see a different ratio of SEP/photosphere for Ni and Fe than for Mg and Si. Cook(1981) observes about the same ratio of SEP/photosphere for Ni and Fe and for Mg and Si. Thus, a model that ties the differences in SEP/photosphere abundance to first ionization potential would have the isotopic composition of the corona and any SEP isotopic abundance average be the same as the isotopic composition of the photosphere.

Table 5.2.1 lists the SEP(Cook) abundances and the abundance results obtained in section 4.3. Also listed are abundance measurements by McGuire et al. (1979) in the energy range 6.7-15 MeV/nuc, for the time interval 78:266:20 - 78:270:00, and a measurement by von Rosenvinge and Reames (1979) for day 78:267, in the energy range 6.7-12.4 MeV/nuc. Note that data from the flare onset is included in the von Rosenvinge and Reames, and McGuire et al. abundances. Cook (1981) has systematically excluded data in flare onsets from his SEP(Cook) averages. Von Rosenvinge and Reames (1979) report a large abundance ratio variation for Fe/O as a function of energy on day 78.267. They report Fe/O abundance ratios of 0.37 ± 0.02, 0.13 ± 0.01, and 0.067 ± 0.007 for energy ranges of 2.0-3.1 MeV/nuc, 3.9-6.7 MeV/nuc, and 6.7-12.4 MeV/nuc, respectively. Figure 5.2.4 is a plot of the ratio of the abundances observed in the 78:266 flare to the SEP(Cook) average. The 78:266 flare element abundances show a relative depletion in the elements Ne,Si,S,Ca, and Fe, relative to SEP(Cook). The magnitude of the depletion is consistent with the flare to flare variations seen by Cook. The disagreement between our measurement of Ne/O and He/O and those of McGuire et al., and von Rosenvinge and Reames is greater than would be expected from a statistical fluctuation. Some of the disagreement for He, Ne, and Fe may be due to the fact that McGuire et al., and

von Rosenvinge and Reames included the flare onset in their abundance measurements. We conclude that the abundance pattern of the 78:266 flare is consistent with that measured for other large flares.

In figure 5.2.4 neon seems to be more depleted than might be expected from the smooth flare to flare behavior of figure 5.2.3. To investigate whether neon was especially depleted in the 78:266 flare, for figure 5.2.5, we plotted Ne/O vs. Mg/O for the seven flares in Cook (1981) and two other flares in McGuire *et al.* (1979) not reported in Cook (1981). Relative to the other large SEP events, the 78:266 flare has a typical value for Ne/O and for Mg/O.

SEP Element Abundances

(relative to the oxygen abundance)

Table 5.2.1 -

Element	(1981) SEP(Cook)	(1979) von Rosenvinge, Reames	(1979) McGuire et al.	this work
He	72 ± 3.3	---	40 ± 3	53 ± 2[a]
C	0.47 ± 0.03	0.40 ± 0.03	0.49 ± 0.03	0.47 ± 0.03
N	0.12 ± 0.01	0.10 ± 0.01	0.12 ± 0.02	0.13 ± 0.01
O	= 1.0	= 1.0	= 1.0	= 1.0
Ne	0.17 ± 0.01	0.09 ± 0.01	0.09 ± 0.01	0.13 ± 0.01
Mg	0.21 ± 0.02	0.21 ± 0.02	0.18 ± 0.02	0.20 ± 0.02
Si	0.17 ± 0.01	0.15 ± 0.02	0.16 ± 0.02	0.13 ± 0.02
Fe	0.20 ± 0.01	0.067 ± 0.007	0.06 ± 0.01	0.14 ± 0.03[b]
				0.07 ± 0.03[c]
				0.03 ± 0.03[d]
				0.08 ± 0.02[e]
Energy	5-15 Mev/nuc	6.7-12.4 MeV/nuc	6.7-15 MeV/nuc	fits 5-50 MeV/nuc
Time	4 flare average 1977-1978	78:267	78:266:20 - 78:270:00	78:268:00 - 78:272:00

[a] 78:269-78:272
[b] RANGE 0, 8-10.4 MeV/nuc
[c] RANGE 1, 11.8-16.5 MeV/nuc
[d] RANGE 2, 16.5-24.3 MeV/nuc
[e] Average RANGEs 0-2

figure 5.2.4 - A plot of the ratio of the elemental abundances observed in the 78:266 flare to the SEP(Cook) element abundance average. The open triangles are measurements by McGuire *et al.* (1979), the crosses are by von Rosenvinge and Reames (1979), and the open squares are for this work.

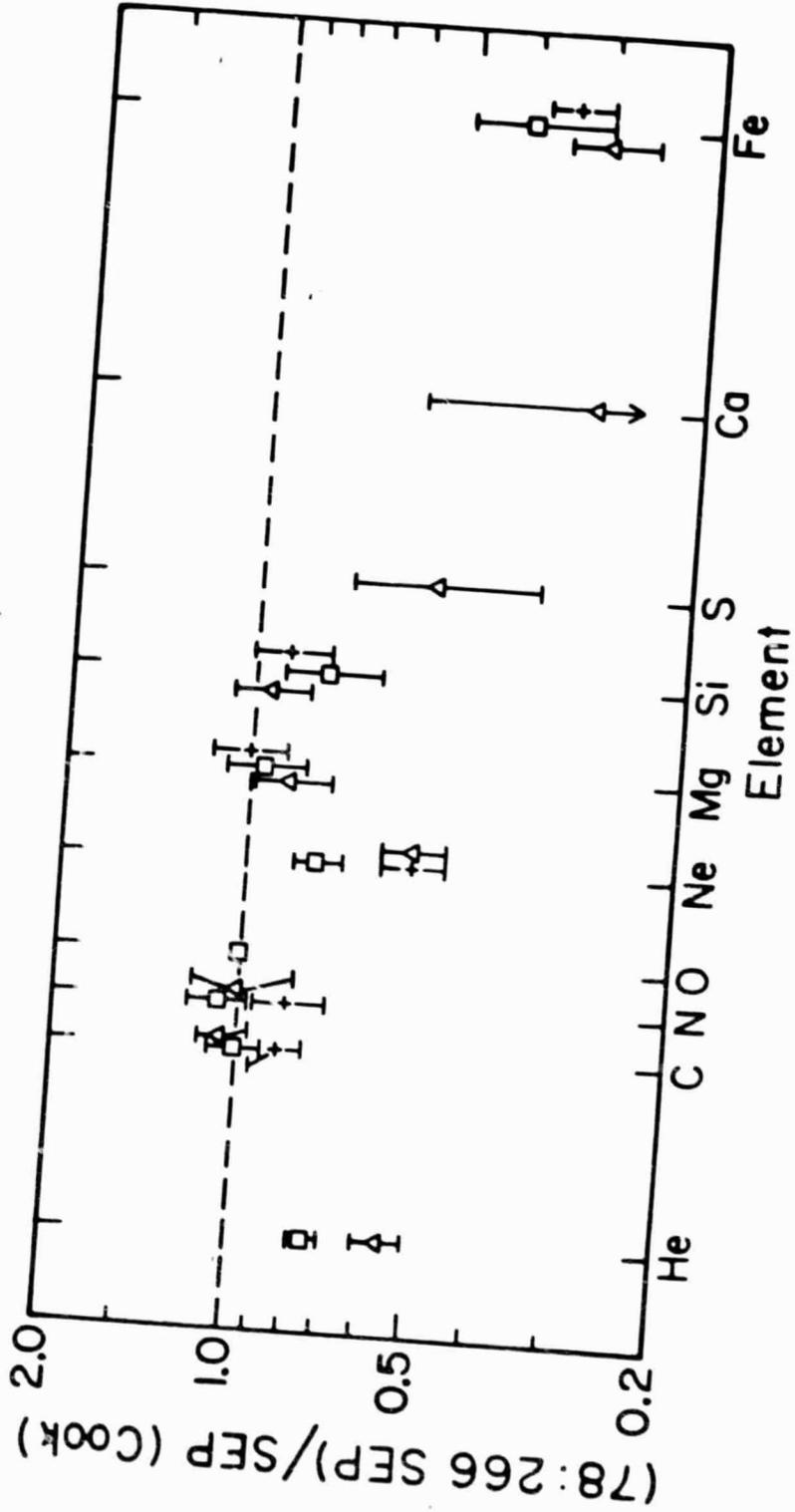ORIGINAL PAGE IS
OF POOR QUALITY

figure 5.2.5 - A plot of the element abundance ratio Ne/O vs. the ratio Mg/O for several flares. The open and filled circles are from Cook (1981). The flares used in the SEP(Cook) average are drawn as filled circles. The SEP(Cook) average is an open circle with a dot inside. The open triangles are from McGuire *et al.* (1979). The open square is from this work.
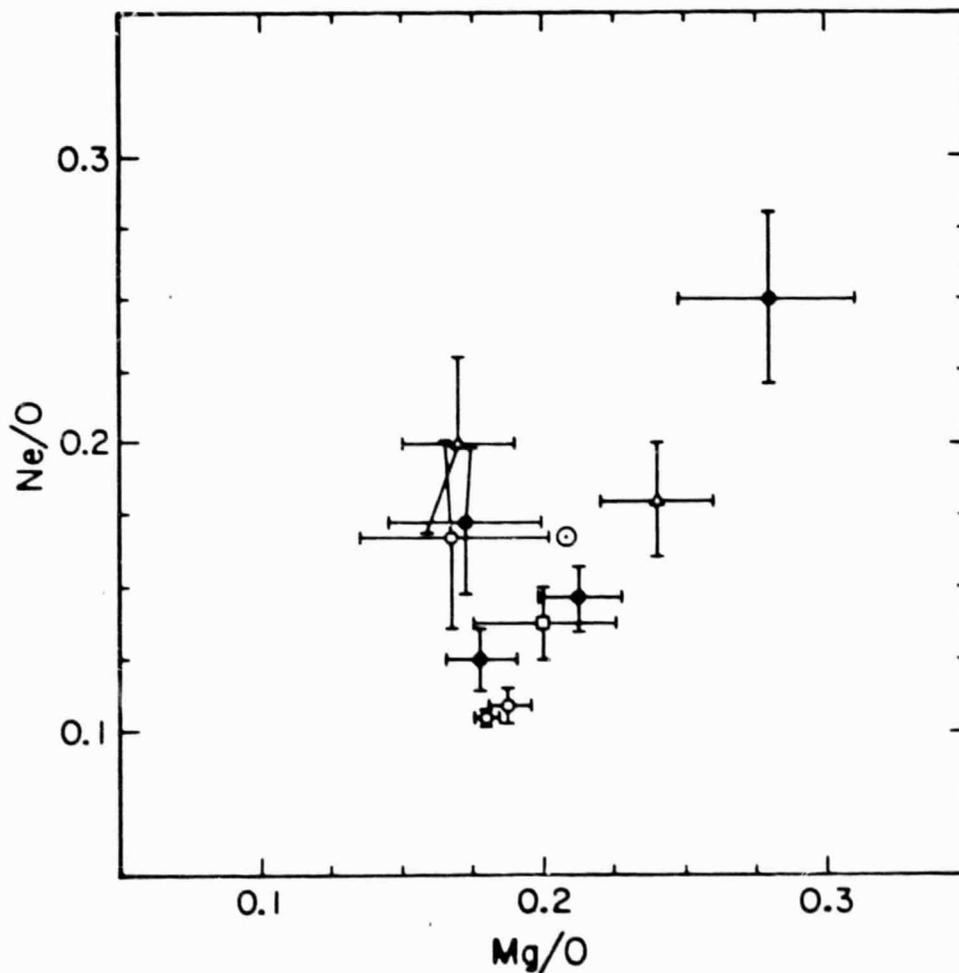
The flare to flare element abundance variations are a relatively smooth monotonic function of charge, about the SEP average. The maximal variation of the Fe/O abundance ratio in the Cook(1981) flare sample is from 0.045 to 0.67, a factor of about 15. Suppose that Fe and O had charges characteristic of a temperature of $1.5 \times 10^6 \, °K$, $Fe^{+10.5}$ and O^{+6}, as calculated by Jordan (1969). Suppose that the enhancement of the Fe/O abundance ratio, $\zeta(Fe/O)$, was related to the charge to mass ratios of Fe and O by the relation, with α varying from flare to flare,

$$\log \zeta(Fe/O) = \alpha \log \left| \frac{q/m(Fe)}{q/m(O)} \right| . \qquad (5.2.1)$$

Then for $\zeta(Fe/O) = 15$, $\alpha = -3.91$. Then the enhancement of the $^{22}Ne/^{20}Ne$ ratio, predicted by equation $5.2.1$ is $\zeta(^{22}Ne/^{20}Ne) = 1.45$. A relation of this type predicts that the $^{22}Ne/^{20}Ne$ abundance ratio variations are correlated with the Fe/O abundance ratio variations. The sign of the effect is such that $^{22}Ne/^{20}Ne$ would be enhanced if Fe/O was enhanced. In the 78:266 SEP event, the Fe/O abundance ratio is not enhanced, so we would not expect the $^{22}Ne/^{20}Ne$ abundance ratio to be enhanced by this mechanism.

5.3. Solar Energetic Particle Isotopic Composition

The isotopic composition of SEPs has been measured directly by instrumentation on spacecraft and indirectly by analysis of moon rocks. Direct measurements of the isotopic composition of SEP events for elements heavier than helium, have also been reported by the University of Chicago charged particle telescope on IMP-8. The Chicago group has achieved a r.m.s. mass resolution of ≈ 0.42 amu for neon events and ≈ 0.56 amu for magnesium events. The IMP-8 instrument has a 750 μ thick front detector, and thus has an energy threshold for two parameter analysis approximately equal to the HIST threshold for RANGE 4 events.

To make an isotope abundance measurement of moderate statistical accuracy, with such a high energy threshold, the Chicago group summed over a group of large solar flares. Dietrich and Simpson (1979) report $^{20}Ne/^{22}Ne = 7.7 +2.3 -1.5$, (equivalent to $^{22}Ne/^{20}Ne = 0.13 \pm 0.03$), for a group of 7 flares, from July 3, 1974 to September 14, 1977. Dietrich and Simpson (1979) divide the seven flares into two groups, 3 are iron-rich, with $Fe/O = 0.80-1.14$, and 4 are iron-poor, with $Fe/O = 0.031 - 0.22$. For the set of iron-poor flares, they measure $^{22}Ne/^{20}Ne = 0.11 \pm 0.04$, and for the set of Fe rich flares, $^{22}Ne/^{20}Ne = 0.15 \pm 0.06$. They find no statistically significant disagreement between the $^{22}Ne/^{20}Ne$ abundances that they report for the two groups of flares. The Dietrich and Simpson (1979) measurements would still be consistent with the predictions of equation 5.2.1, which would predict an enhancement of $\approx 35\%$ for the $^{22}Ne/^{20}Ne$ abundance ratio in the Fe-rich flares, relative to the Fe-poor flares. Our measurement of Fe/O in the 78:266 flare would classify the 78:266 flare as an Fe-poor flare.

There is a need for more measurements of SEP isotope abundances to determine whether the flare to flare isotope abundances also vary in a manner analogous to the SEP elemental abundance variations.

Dietrich and Simpson (1981) report $^{26}Mg/^{24}Mg = 0.13 \pm 0.04$, for a group of 10 flares, from July 3, 1974 to April 28, 1978. They do not report results for the $^{21}Ne/^{20}Ne$ and $^{25}Mg/^{24}Mg$ abundance ratios, because those isotopes were not resolved in their data.

Indirect measurements of SEP isotope abundance ratios have been reported, using moon rocks as collectors for the SEPs. Black (1972a,b) has presented evidence for the existence of a neon component in lunar soils and meteorites that was implanted by solar energetic particles of 1-10 MeV/nuc. Black finds isotope abundance ratios for the component, neon-C, of

^{3}He/^{4}He = 4.1 ± 1.0 x 10^{-4}, ^{22}Ne/^{20}Ne = 0.094 ± 0.003, and ^{36}Ar/^{38}Ar = 4.1 ± 0.8. Venkatesan *et al.* (1981) studied etched feldspar separates of lunar soils and conclude that the long term average solar flare Ne composition is about ^{22}Ne/^{20}Ne ≈ 0.083. Yaniv and Marti (1981) find ^{22}Ne/^{20}Ne = 0.082 ± 0.001 in the near surface layers of a lunar rock and conclude that ^{20}Ne may be depleted in solar flares. Etique *et al.* (1981) find ^{22}Ne/^{20}Ne ≥ 0.089 for solar flares, by etching lunar plagioclase samples. All experimenters measure a ^{22}Ne/^{20}Ne abundance that is lower than the solar wind values reported by Eberhardt *et al.* (1970), but higher than the direct measurements in this work and by the Chicago group.

The ^{3}He/^{4}He abundance ratio has been measured by a number of groups of experimenters. Anglin (1975) measures ^{3}He/^{4}He = 0.027 ± 0.005 in a 1969-1972 flare sum. Hurford (1975) has ^{3}He/^{4}He = 0.009 ± 0.004 in an October 1972 to November 1973 flare sum. For the large SEP events analyzed by McGuire *et al.* (1979), only upper limits, ranging from 0.008 to 0.06, for the ^{3}He/^{4}He abundance ratio were reported. For the large August 1972 series of events, Webber *et al.* (1975) report finite ^{3}He/^{4}He abundance ratios that vary with energy, ranging from about 0.001 at ≈ 10 MeV/nuc, to about 0.015 at ≈ 60 MeV/nuc. They interpret their result as due to spallation in the solar atmosphere.

For another class of SEP event, higher values of ^{3}He/^{4}He have been reported. ^{3}He-rich (Garrard *et al.* 1973) events are SEP events in which ^{3}He/^{4}He is noticeably enhanced (^{3}He/^{4}He ≥ 0.1) over average values measured in large SEP events, discussed in the above paragraph. The high abundance of ^{3}He/^{4}He coupled with the low observed abundances for D/H and T/H, means that high energy nuclear spallation reactions cannot have caused the high ^{3}He/^{4}He abundances (Garrard *et al.* 1973). Relative to the average SEP abundances measured in large events, ^{3}He-rich events have lower H fluxes, higher

^{4}He/H ratios and higher ratios of elements with charges $Z \geq 6$ to ^{4}He. ^{3}He-rich events have generally been observed as small SEP events (Hurford et $al.$ 1975, Hovestadt et $al.$ 1975, Mason et $al.$ 1980). In two small ^{3}He-rich events, mentioned in section 3.4, $\approx$ 300 He events were observed, while for the 78:266 flare, over 10^6 He events were seen.

^{3}He-rich events are of interest here because of the large isotope enhancements observed; Hurford et $al.$ (1975) report ^{3}He/^{4}He ~ 8 for one event, or 2×10^4 times the value reported for the solar wind. It is possible that a ^{3}He-rich event could occur simultaneously with a large SEP event, or be triggered by it. Despite the low flux levels of ^{3}He-rich events, the extremely large isotope enhancements might bias the isotope measurements in large SEP events, if a ^{3}He-rich event occurred at the same time as a large SEP event.

According to a model by Fisk (1978), selected ions can be preheated at the flare site, prior to the flare, when the ions satisfy an electrostatic ion cyclotron wave resonance condition. The conditions necessary for the Fisk model to apply are that $n_{He}/n_H \geq 0.2$, $T_e/T_i \geq 5$, and that β, the ratio of thermal energy to magnetic field energy, satisfies $\beta \leq 10^{-3}$, at the flare site. The resonance frequency lies between the H and He gyrofrequencies, and only the ^{3}He gyrofrequency satisfies the resonance condition with its first harmonic.

Ions other than ^{3}He can also be preheated in this model if the second harmonic of the ion gyrofrequency Ω_i satisfies the equation (Mason et $al.$ 1980)

$$1.05 < 2\Omega_i/\Omega_{He} < 1.19 + 0.13(m_{He}/m_i)^{\frac{1}{2}} \ . \tag{5.3.1}$$

Figure 5.3.1, modified from figure 10 in Mason et $al.$ (1980), is a plot of the frequency of the second harmonic of the ion gyrofrequency for the various charge states of abundant solar isotopes. Selective isotope enhancements for heavy elements in the Fisk model may not be plausible. First, the equation 5.3.1 resonance condition selects a wide band of frequencies,

figure 5.3.1 - (adapted from Mason *et al.* (1980)) A plot of one half of the second harmonic of the gyrofrequency for various charge states of several ions, as a function of Ω_i / Ω_{He}.
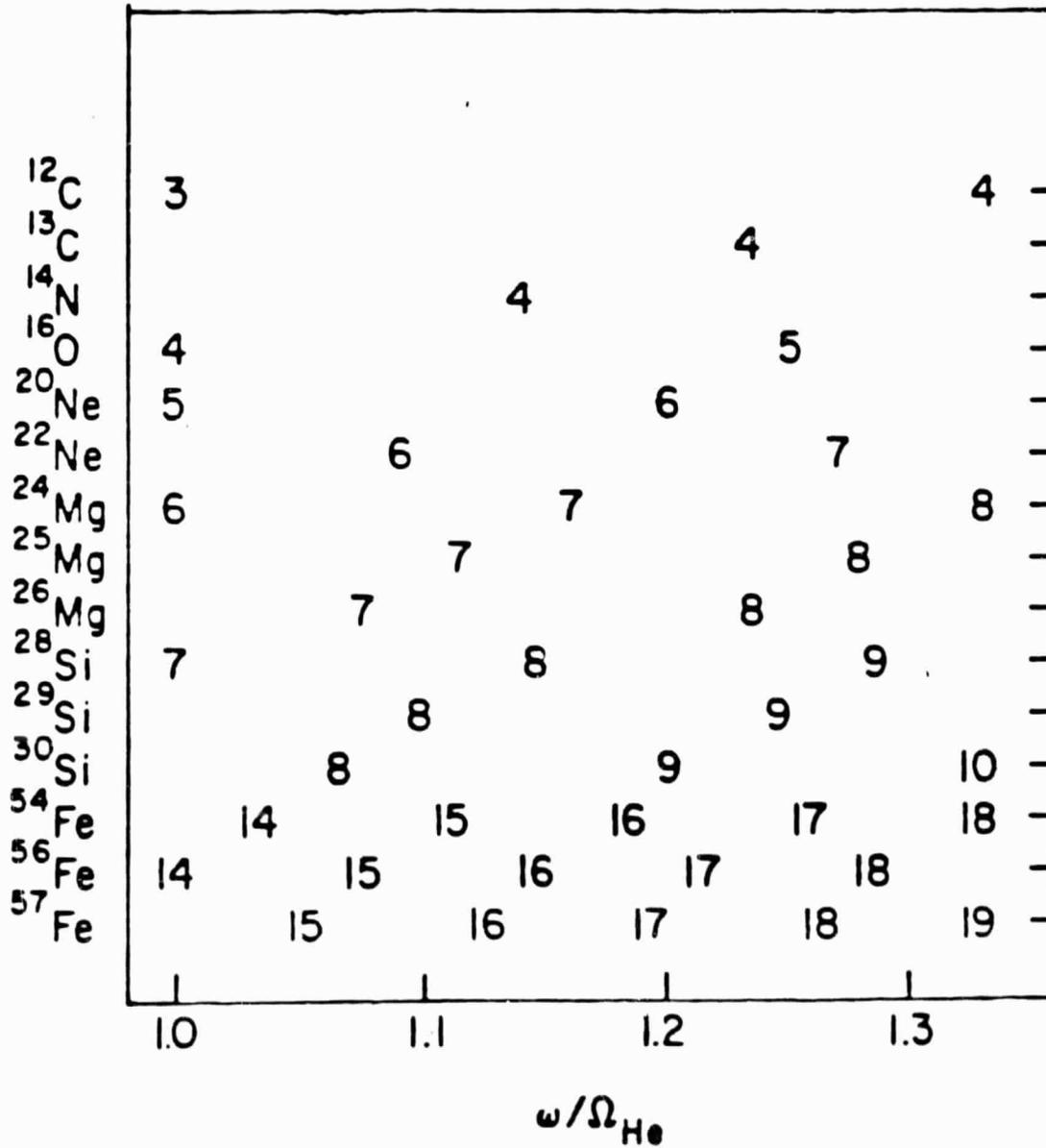
and different isotopes of the same element are separated by much less than the width of the allowed frequency band. Secondly, in a realistic model of the flare site, the charge state distribution for the heavy ions would be spread over several charge states due to inhomogeneities in temperature at the flare site. For neon the primary charge state varies from +6 to +10 as the temperature varies from $\approx 5 \times 10^5$ °K to $\approx 5 \times 10^6$ °K, according to the charge state calculations of Jordan (1969). In particular, a large $^{22}Ne/^{20}Ne$ enhancement could only be produced if most of the neon was in charge state $+7$, at a temperature of $\approx 5.6 \times 10^5$ °K, and very little neon was in charge state +6, and if the upper limit to the enhanced gyrofrequencies was about $2\Omega_4/\Omega_{H_4} = 1.3$. Our upper limit for the $^3He/^4He$ abundance ratio in the 78:266 SEP event is $^3He/^4He \le 0.0026$, measured in RANGES 2-5.

Thus we believe that the 78:266 flare is not described by this type of flare model. The narrow range of flare site temperatures required to produce a $^{22}Ne/^{20}Ne$ enhancement and the absence of any measurable enhancement in the $^3He/^4He$ abundance ratio argue against the Fisk (1978) model for flare site preheating in this flare.

5.4. Solar Isotope Measurements

Direct measurements of the solar isotopic composition are rare. Some studies have looked at the spectra of molecules in sunspots, which are a cooler environment than the photosphere. Hall (1973) and Hall, Noyes, and Ayres (1972) have investigated the infrared spectra of the molecule CO. The abundance of $^{13}C/^{12}C$ was found to be 0.94 ± 0.1 of the "terrestrial" value. $^{18}O/^{16}O$ was measured as 1.06 ± 0.35 of the terrestrial value. With Cameron's (1981) values for the the above terrestrial abundance ratios, then $^{13}C/^{12}C = 0.0104 \pm 0.0011$ and $^{18}O/^{16}O = 0.0021 \pm 0.0007$.

Boyer, Henoux, and Sotirovski (1971) observed absorption lines due to the molecule MgH in sunspot spectra and obtained $^{25}Mg/^{24}Mg = 0.125 \pm 0.038$ and $^{26}Mg/^{24}Mg = 0.125 \pm 0.038$. Their results conflict with Branch (1970) who obtained $^{24}Mg:^{25}Mg:^{26}Mg$ of 60:20:20. Branch's work was criticized in Lambert, Mallia, and Petford (1971), who set limits for the abundance ratios $^{25}Mg/^{24}Mg$ and $^{26}Mg/^{24}Mg$, that they believe are consistent with the terrestrial abundance ratios of $^{24}Mg:^{25}Mg:^{26}Mg$ of 80:10:10.

Hall (1975) has measured solar $^{3}He/^{4}He$ abundance by fitting the shape of a helium spectral line feature at 10830 A, observed in emission in a prominence. Hall obtains $4 \pm 2 \times 10^{-4}$ for the $^{3}He/^{4}He$ abundance ratio.

5.5. Solar Wind Isotopic Composition

The solar wind provides a sample of material from the sun. The isotopic composition of the solar wind has been measured by instrumentation flown on satellites, and by mass spectroscopic means, after collection on the surface of moon rocks, or on special foils deployed by the Apollo astronauts. For selected isotope ratios, the composition of the solar wind has been experimentally measured to an accuracy of a few per cent. The major problem is to relate the isotopic composition of the solar wind to the isotopic composition of the sun.

The elemental and isotopic composition of the solar wind is not constant as a function of time. The He/H abundance ratio in the solar wind can vary on time scales from years to minutes, the magnitude of the He/H values reported have ranged from 8.1×10^{-4} to 0.42 (Neugebauer 1981). The $^{3}He/^{4}He$ abundance ratio is also observed to vary. Ogilvie et al. (1980) find that $^{3}He/^{4}He$ is correlated with ^{4}He bulk velocity and varies from greater than 5×10^{-3} to less than 2×10^{-6}. Thus time variable mass fractionation effects occur in the solar wind.

The long term average abundances of elements and isotopes in the solar wind do not show such a large range of variation. Ogilvie and H'rshberg (1974) find a solar cycle variation in the He/H ratio of only 0.01 ± 0.01, from 0.035 to 0.045. The abundance ratios, though relatively stable, may still be appreciably fractionated and different from the Sun's composition. The solar He/H abundance is not well known. Heasly and Milkey (1978) measure He/H = $0.1C \pm 0.025$ in quiescent solar prominences. Ross and Aller (1976) have He/H = 0.063 (+ 0.037 − 0.023), based on Lambert's (196?) analysis of the photospheric O/H abundance and the He/O abundance from SEPs.

If the He/H abundance in the outer parts of the sun has not been altered by nuclear processing, then it should be equal to the He/H abundance at the time that the sun formed. Geiss and Reeves (1972,1981) set an upper limit of 2×10^{-5} for the D/H ratio in the material out of which the sun was formed. This upper limit to D/H, according to a standard model of big-bang nucleosynthesis, (Wagoner 1973), sets a lower limit to the He/H abundance of He/H = 0.075, as the stellar destruction of He since the big bang is negligible.

A reliable value of He/H in the solar neighborhood is He/H = 0.101 ± 0.005 (Piembert 1975), obtained by analyzing H II regions of the Orion nebula. Thus, the sun probably has a value of He/H of about 0.1 and He/H is very likely to be greater than 0.075. The ratio of these estimates of the solar He/H value to the long term averages of solar wind He/H ratios is at least 0.075/0.045 = 1.67, and probably greater than 2. Further evidence for helium depletion in the solar wind may come from the helium enhancements observed in the post-shock solar wind plasma, after the passage of a flare associated shock wave (Bame et al. 1979, Hundhausen 1972).

Models of the solar wind are not yet very successful at explaining the reasons for the fluctuating abundance ratios. ^{3}He/^{4}He and He/H Geiss et al.

(1970) have considered a model of the solar wind in which a proton fluid expands out from the solar corona, dragging the ions by dynamical friction. In that model, ions are accelerated in the solar wind only if the proton fluid has a certain minimum flux, which is a function of the ion's charge and mass. For charge states characteristic of the solar corona, if ^{4}He is accelerated in the solar wind, then so are all other ions heavier than ^{1}H, with the exception of D.

Ogilvie *et al.* (1980) have searched for a correlation, predicted by the model of Geiss *et al.*, between the ^{3}He/^{4}He abundance in the solar wind and the H flux. They do not find such a correlation, but instead find a correlation between ^{3}He/^{4}He and ^{4}He flux. Schmidt *et al.* (1980) measure the speeds of H^+, He^{++}, and O^{6+} in the solar wind and find $v(He^{++}) - v(H^+)$ and $v(O^{6+}) - v(H^+)$ to be on average equal and in the range 0 to +60 km/sec. Ions with velocities greater than hydrogen require a means of acceleration in addition to dynamical friction (Schmidt *et al.* suggest solar wind plasma waves) which could change Geiss *et al.*'s (1970) conditions for fractionation effects.

We can conclude that a consistent theoretical and experimental framework to explain the helium element and isotope abundance variations in the solar wind does not yet exist. In particular whether or not there is a difference between the long term solar wind ^{3}He/^{4}He abundance and that of the sun is not known. Geiss *et al.* (1972) measure ^{3}He/^{4}He = $4.3 \pm 0.2 \times 10^{-4}$ in the solar wind and Hall (1975) obtains ^{3}He/^{4}He = $4 \pm 2 \times 10^{-4}$ for the spectra of a solar prominence. If the difference between solar wind and the sun's He/H abundances depended only on the charge to mass ratio, then the ^{3}He/^{4}He abundance might be $\approx 33\%$ larger than on the sun. We based this estimate on equation 5.2.1 and an assumed depletion of the He/H abundance ratio in the solar wind relative to the Sun of a factor of 2. The data do not exclude this possibility.

The solar wind noble gases have been extensively measured after collection

on special foils and on moon rocks. Geiss *et al.* (1972) averaged the results of several Apollo foil collection experiments and obtained $^3He/^4He = 4.3 \pm 0.2 \times 10^{-4}$, $^{22}Ne/^{20}Ne = 0.073 \pm 0.002$, and $^{21}Ne/^{22}Ne = 0.033 \pm 0.004$. Eberhardt *et al.* (1970,1972) analyzed trapped solar wind noble gases in lunar soils and obtain $^3He/^4He = 3.7 \pm 0.1 \times 10^{-4}$ and $^{22}Ne/^{20}Ne = 0.078 \pm 0.001$ for the present day solar wind. There is a slight difference between the two sets of values, which is evidence that the lighter isotopes are slightly depleted in the moon rocks.

Eberhardt *et al.* (1972) report that for trapped Ar in lunar soils, the abundance ratio is $^{36}Ar/^{38}Ar = 5.33 \pm 0.03$, in agreement with terrestrial $^{36}Ar/^{38}Ar$ values. They report trapped Kr isotope abundances in lunar soils that are fractionated by about 0.5% per a.m.u. relative to terrestrial values, but consider solar wind and terrestrial Kr to be consistent within the accuracy of the method. The lunar trapped Kr isotopic abundances also agree with the average value of trapped Kr in carbonaceous chondrites. The agreement of Ar and Kr isotope abundances with terrestrial values argues against solar wind mass fractionation of the noble gases, unless all of the terrestrial Ar and Kr was deposited on the earth by the solar wind. If there was solar wind isotope fractionation, then the terrestrial pattern would have to exactly match the solar wind pattern, to reproduce the experimental results.

The isotopes of Xe do not agree with the above picture (Podosek 1978, Eberhardt *et al.* 1972). Compared with terrestrial values, the trapped solar Xe isotope abundances show mass fractionation of about 3% per a.m.u., difficult to explain at the same time as the Ar and Kr results. The average isotopic composition of carbonaceous chondrites agrees with solar trapped Xe for mass numbers 124-130. Xe mass numbers 132-136 for the chondrites's abundances show an excess compared to the solar trapped Xe, which has been attributed to

fission fragments. However, the mass spectrum of the Xe is not that expected from common fission parents. Xe then may question the internal consistency of the above picture that the solar wind has undergone minimal mass fractionation.

Other elements have been identified on the surface of moon rocks as having possibly been implanted there by the solar wind. There is evidence that the surface component of lunar nitrogen has had its $^{15}N/^{14}N$ abundance ratio increase in the past by about 15-20% (Kerridge *et al.* 1977, Becker and Clayton 1975). For samples in which both $^{15}N/^{14}N$ and $^{22}Ne/^{20}Ne$ were measured, the change in the $^{15}N/^{14}N$ abundance is not correlated with the $^{22}Ne/^{20}Ne$ abundance. Becker (1980) finds a weak correlation between the $^{15}N/^{14}N$ abundance and $^{13}C/^{12}C$ abundance, though the change in $^{13}C/^{12}C$ abundance is about $\frac{1}{10}$ as large as the change in the $^{15}N/^{14}N$ abundance. Kerridge *et al.* (1977) find no convincing explanation of the variable $^{15}N/^{14}N$ abundance ratio, and they consider both effects at the lunar surface and mechanisms that change the solar wind composition with time.

Epstein and Taylor (1972) have found that carbon in lunar soils has a total carbon content that is correlated with the hydrogen content. Samples with high carbon content have $^{13}C/^{12}C$ enriched by about 5% over soils with a low carbon content. They do not believe that they have positively identified the source of the isotopically heavy carbon, though one of the possibilities that they mention is that the heavy carbon comes from the solar wind.

Thus, for carbon and nitrogen, incomplete physical understanding of the source of lunar carbon and nitrogen prevent a sure identification of the isotopic composition of solar wind carbon and nitrogen. We can distinguish several possibilities. For the first, we may suppose that neither the $^{15}N/^{14}N$ nor the $^{13}C/^{12}C$ abundance ratios measured above accurately reflect the composition of

the solar wind. For the second, if either the carbon or the nitrogen isotopic abundance accurately reflects the solar wind, then that would be strong evidence against a simple linear mass fractionation process operating in the solar wind acceleration process. If the nitrogen results accurately measure the solar wind and solar wind compositional time variations, and are not a result of a changing solar surface composition, then the problem becomes more complex. If some unknown effect can cause the $^{15}N/^{14}N$ ratio to vary and not other isotope ratios, like $^{22}Ne/^{20}Ne$ and $^{13}C/^{12}C$, then we cannot predict the behavior of one isotope ratio by observing another isotope ratio. The nitrogen results, like the Xe results, might tend to question the internal consistency of of a simple picture suggesting the absence of solar wind mass fractionation for isotope ratios in the solar wind.

Zinner *et al.* (1977) analyzed surface enhancements of Mg that may be due to the solar wind. They find isotopic abundances that are consistent with terrestrial values within the experimental uncertainties estimated (Zinner 1979) to be about 20%.

5.6. Comparison of SEP and Solar Isotope Abundances

The goal of our analysis is to compare solar and SEP isotope measurements. That task is made difficult by the scarcity of direct solar isotope measurements. As discussed in section 5.4, the direct measurements of the isotope ratios $^{3}He/^{4}He$, $^{13}C/^{12}C$, $^{18}O/^{16}O$, $^{25}Mg/^{24}Mg$, and $^{26}Mg/^{24}Mg$, have uncertainties of 50%, 10%, 35%, 30%, and 30%, respectively. We could not find direct solar values for the isotope ratios $^{22}Ne/^{20}Ne$ and $^{15}N/^{14}N$. Table 5.6.1 contains a list of measurements of the isotope ratios of the elements He, C, N, O, Ne, and Mg, discussed in this chapter, along with our SEP measurements.

A source for indirect information about the isotopic composition of the Sun is the composition of the carbonaceous chondrite class of meteorite. As

discussed in Wasserburg *et al.* (1980), the isotopic composition of meteorites and terrestrial materials is characterized by its homogeneity, the isotopic compositions of any two samples of solar system material are likely to be the same to an accuracy of much better than a per cent. This was thought to be strong evidence for the view that the solar system at "birth" had a uniform isotopic composition, and that the small variations in isotopic composition seen today on the Earth are the result of various physical and chemical fractionation processes. Recently, as discussed in Wasserburg *et al.* (1980), evidence of primordial inhomogeneities has been found, in the anomalous isotopic composition of parts of certain meteorites. Except for some noble gases, the maximum difference between the anomalous and terrestrial isotopic abundances that has been seen is about 5-6%.

The best accuracy that we report for our SEP isotope ratio results in tables 4.2.1 and 5.6.1 is about 20%. For our purposes we can take as "solar" the terrestrial and meteoritic abundances for the elements which are not noble gases, C, N, O, and Mg. We have used the terrestrial and meteoritic abundance compilation of Cameron (1981) as a source for these values, also listed in tables 4.2.1 and 5.6.1.

Table 5.6.1 -

abundance ratio	value	source	reference
^{3}He/^{4}He	$4.3 \pm 0.2 \times 10^{-4}$	solar wind	Geiss *et al.* (1972)
	$4.0 \pm 2.0 \times 10^{-4}$	solar spectra	Hall (1973)
	$3.7 \pm 0.1 \times 10^{-4}$	solar wind implanted in lunar soils	Eberhardt *et al.* (1972)
	$4.2 \pm 0.8 \times 10^{-4}$	meteorites (He-B)	Mazor *et al.* (1970)
	$1.3 \pm 0.8 \times 10^{-4}$	meteorites (He-A)	Mazor *et al.* (1970)
	0.027 ± 0.005	SEPs	Anglin (1975)
	0.009 ± 0.004	SEPs	Hurford (1975)
	≤ 0.0026	SEPs	this work
^{13}C/^{12}C	$0.0104 \pm .0011$	solar spectra	Hall (1973)
	0.0111		Cameron (1981)
	$0.0095 + 0.0042 - 0.0029$	SEPs	this work
^{15}N/^{14}N	$\approx +10\%$ to $\approx -5\%$ of terrestrial	solar wind implanted in lunar soils	Kerridge *et al.* (1977)
	0.0037		Cameron (1981)
	$0.008 + 0.010 - 0.005$	SEPs	this work

Table 5.6.1 -
(cont.)

abundance ratio	value	source	reference
$^{18}O/^{16}O$	0.0021 ± 0.0007	solar spectra	Hall (1973)
	0.0020		Cameron (1981)
	0.0015 + 0.0011 − 0.0007	SEPs	this work
$^{21}Ne/^{20}Ne$	0.0026 ± 0.0001	Ne-B	Black(1972a)
	0.0024 ± 0.0003	solar wind	Geiss *et al.* (1972)
	0.0025 ± 0.0001	solar wind implanted in lunar rocks	Eberhardt *et al.* (1970)
	0.0030		Cameron (1981)
	≤ 0.014	SEPs	Mewaldt *et al.* (1979)
	≤ 0.014	SEPs	this work
$^{22}Ne/^{20}Ne$	0.073 ± 0.001	solar wind	Geiss *et al.* (1972)
	0.078 ± 0.002	solar wind implanted in lunar soils	Eberhardt *et al.* (1972)
	0.080 ± 0.001	Ne-B	Black (1972a)
	0.122 ± 0.006	Ne-A	Pepin (1967)
	0.122		Cameron (1981)
	0.13 ± 0.03	SEPs	Dietrich and Simpson (1979)
	0.11 ± 0.04 0.15 ± 0.06	SEPs, Fe-poor SEPs, Fe-rich	" "
	0.13 + 0.04 − 0.03	SEPs	Mewaldt *et al.* (1979)
	0.109 + 0.026 − 0.019	SEPs	this work

**Table 5.6.1-
(cont.)**

abundance ratio	value	source	reference
$^{25}Mg/^{24}Mg$	0.125 ± 0.038	solar spectra	Boyer *et al.* (1971)
	terrestrial $\pm$ 20%	solar wind implanted in a lunar rock	Zinner (1977)
	0.129		Cameron (1981)
	$0.15 \begin{array}{c} +0.05 \\ -0.02 \end{array}$	SEPs	Mewaldt *et al.* (1981)
	$0.148 \begin{array}{c} +0.043 \\ -0.025 \end{array}$	SEPs	this work
$^{26}Mg/^{24}Mg$	0.125 ± 0.038	solar spectra	Boyer *et al.* (1971)
	terrestrial $\pm$ 20%	solar wind implanted in a lunar rock	Zinner (1977)
	0.142		Cameron (1981)
	$0.15 \begin{array}{c} +0.04 \\ -0.03 \end{array}$	SEPs	Mewaldt *et al.* (1981)
	0.13 ± 0.04	SEPs	Dietrich and Simpson (1981)
	$0.148 \begin{array}{c} +0.046 \\ -0.026 \end{array}$	SEPs	this work

The noble gases are a more complicated story. For the elements He and Ne observed in meteorites, two primary components have been discovered, "A", or the "planetary" component and "B", or the "solar" component. He-A has ^{3}He/^{4}He $\approx 1.5 \times 10^{-4}$ and He-B has ^{3}He/^{4}He $\approx 3.9 \times 10^{-4}$, while Ne-A has ^{22}Ne/^{20}Ne ≈ 0.122 and Ne-B has ^{22}Ne/^{20}Ne ≈ 0.080 (Podosek 1978). "B", the "solar" component, is thought to have been implanted in the meteorites by the solar wind. This idea is strengthened by the analysis of trapped solar wind gases in lunar soils, where ^{22}Ne/^{20}Ne $= 0.078 \pm 0.001$ and ^{3}He/^{4}He $= 3.7 \pm 0.1 \times 10^{-4}$ (Eberhardt et al. 1970) is obtained. It has been suggested that the difference between the present day solar wind neon measurements of Geiss et al. (1972), with ^{22}Ne/^{20}Ne $= 0.073 \pm 0.002$, and the two measurements of solar wind neon trapped in lunar soils and in meteorites may reflect mass fractionation that occurs in the trapping process. At argon the difference between the "solar" and "planetary" components becomes much smaller. In meteorites Mazor et al. (1970) have found that there are only small variations in ^{36}Ar/^{38}Ar. ^{36}Ar/^{38}Ar varies from 5.3 to 5.5, as the ^{22}Ne/^{20}Ne composition varies from ≈ 0.125 to ≈ 0.080, or from the "planetary" to "solar" compositions.

We want to know the isotopic composition of the Sun, for He and Ne; is it similar to the "solar" or "planetary" meteoritic compositions, or is it something else entirely? We will explore the views that the Sun is either "solar" or "planetary" in its noble gas isotopic composition, and examine the consequences of each.

The argument that the Sun has "solar" noble gas isotopic composition is supported by the noble gas elemental abundance patterns in "solar" and "planetary" gases. Relative to the "solar" gases, the "planetary" noble gas elemental composition pattern shows a depletion of about 4 orders of magnitude

for the light noble gases relative to the heavy noble gases (Podosek 1978). This elemental depletion could have been accompanied by isotope fractionation. The lighter isotopes of the "planetary" component of He and Ne are depleted relative to the "solar" component.

The close agreement between the isotopic composition of the "solar" meteoritic gases for the elements He and Ne, and the solar wind measurements of He and Ne, support the identification of the "solar" meteoritic component as implanted by the solar wind. Then the Sun would have " solar"noble gas isotopic abundances if the solar wind was an unfractionated sample of the Sun. In section 5.3 we discussed the evidence for the absence of a simple linear mass fractionation bias in the long term average isotopic composition of the solar wind. In general the evidence was consistent with a lack of a simple linear mass fractionation bias, but the elements nitrogen and xenon were not explained by the simple picture. If there is no mass fractionation bias to the solar wind, then the solar isotopic composition for the elements helium and neon would be that measured by Geiss et $al.$ (1972), with $^3He/^4He = 4.25 \pm 0.22 \times 10^{-4}$, and $^{22}Ne/^{20}Ne = 0.073 \pm 0.002$. Our SEP measurement of $^{22}Ne/^{20}Ne = 0.109 + 0.026 - 0.019$ disagrees with the solar wind measurement and we would then have to look for bias in the solar flare acceleration process.

The view that the Sun is made of "planetary" noble gases seems to require some type of mass fractionation in the solar wind acceleration process, for the elements helium and neon. That view assumes that the depletion of lighter noble gases in the "planetary" component of meteorites did not affect the isotopic composition of the gases left behind in the meteorites. The "planetary" isotopic compositions for helium and neon then more closely reflect the isotopic composition of the Sun, than does the isotopic composition of the solar wind. This view is supported by Cameron (1981) who uses "planetary" isotopic compo-

sitions for his noble gas isotopic compositions. Mewaldt *et al.* (1979,1981), in an earlier presentation of this work, have argued that their SEP measurements support the "planetary" view. Their SEP measurement of the $^{22}Ne/^{20}Ne$ ratio is much closer to neon-A than to neon-B. The other isotope abundance ratios that they measure for C, N, O, and Mg, do not show any evidence for a simple SEP mass fractionation bias that would explain the $^{22}Ne/^{20}Ne$ result.

The isotope abundance ratio results in this work do not represent a statistically significant difference between this work and Mewaldt *et al.* (1979, 1981). I do not find their suggestion that the Sun is made of neon-A attractive, primarily because I find no convincing evidence of solar wind mass fractionation. We have seen in the previous section that Ar and Kr isotope abundances for the solar wind implanted in moon rocks agree with terrestrial abundance ratios. This is a strong argument against a simple linear solar wind mass fractionation. According to the theory of Geiss *et al.* (1970), Ar requires a higher flux of H in the solar wind to be "pulled along" in the solar wind than does Ne, and so should be even more susceptible to mass fractionation. To me it is more plausible that an isotopic mass fractionation accompanied the observed depletion of the light noble gases in the formation of the "planetary" noble gas component of meteorites.

In the following discussion we will compare our measurements with our best estimate of the Sun's isotopic composition. We will take the position that the solar wind isotopic composition is identical to that of the Sun. The direct measurements of Geiss *et al.* (1972) will be used for the He and Ne abundance ratios. For C, N, O, and Mg, we will use the meteoritic and terrestrial isotope abundances from the Cameron compilation (1981).

Table 5.6.2 contains the comparison between our measurements (corrected for energy/nuc) and the solar values. The "reduced difference SEP - solar" is

the difference between our SEP measurement and the solar abundance ratio given in the table, divided by the error in the SEP measurement. There is good agreement between our SEP measurements and the solar abundances, except for $^{22}Ne/^{20}Ne$. The isotope abundance ratio for which the best solar wind and SEP measurements exist, shows a marked disagreement between the solar wind and SEP values. Our likelihood confidence interval calculations give a 2.5% probability that the SEP isotope ratio could be as low as $^{22}Ne/^{20}Ne = 0.073$, measured in the solar wind.

We can investigate the possibility that a simple linear mass fractionation in the SEPs produced the distribution of isotope abundance ratios that we measured. We define a normalized isotope abundance ratio for element Z as the ratio of our SEP isotope abundance ratio for element Z divided by the solar isotope abundance ratio for element Z. Figure 5.6.1 shows the normalized isotope abundance ratios for our measurements of $^{13}C/^{12}C$, $^{18}O/^{16}O$, $^{22}Ne/^{20}Ne$, $^{25}Mg/^{24}Mg$, and $^{26}Mg/^{24}Mg$, plotted as a function of the ratio of the isotope masses, A_j/A_i, where A_j is the heavier isotope. For a simple linear mass fractionation process, the enhancement, $\zeta(j,i)$, of isotope j relative to isotope i, is

$$\zeta(j,i) = \alpha \left[(\frac{A_j}{A_i}) - 1 \right] . \qquad (5.6.1)$$

If a linear mass fractionation process had operated on SEPs, the plot of reduced abundances vs. A_j/A_i would be a straight line. The line's intercept would be a normalized abundance equal to 1 at $A_j/A_i = 1$. The data for elements C, O, and Mg seem to be consistent with an absence of SEP mass fractionation. The Ne point does not follow the trend of the other data.

Figure 5.6.1 - A plot of the normalized isotope ratio abundance $(X_i / X_j)_{SEP} / (X_i / X_j)_{solar}$ as a function of the ratio of the masses of isotopes i and j, A_i / A_j.
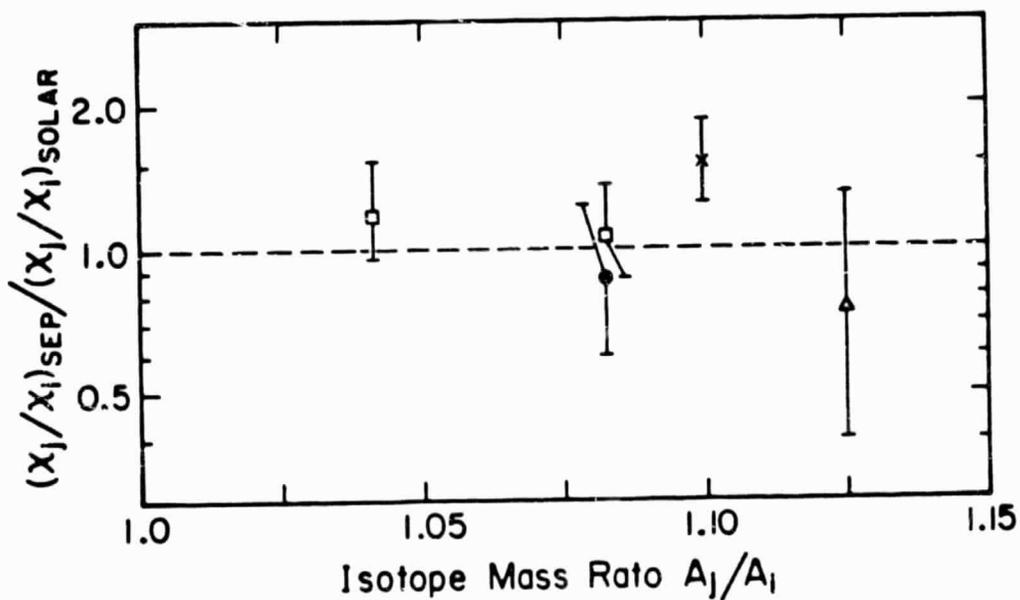
Mewaldt *et al.* (1979) investigated the possibility that the $^{22}Ne/^{20}Ne$ abundance ratio was altered by nuclear spallation reactions, which might have occurred as the SEPs pass through the solar atmosphere. They found that nuclear spallation reactions in the solar atmosphere were much more likely to produce ^{21}Ne than ^{22}Ne. Then the observed upper limit to the $^{21}Ne/^{20}Ne$ abundance ratio of $^{21}Ne/^{20}Ne \leq 0.014$, implies that much less than $0.014/0.109 = 13\%$ of the ^{22}Ne events could have been produced by high energy nuclear reactions as the SEPs propagated from the flare site to HIST. It is then not likely that nuclear spallation reactions by the SEP particles have caused the difference between the solar wind and the SEP $^{22}Ne/^{20}Ne$ measurements.

Thus, the neon seems to be a puzzle. If neon is fractionated in the solar wind, the fractionation process must be chemically selective, it must produce much more severe fractionation for neon than for argon and krypton. The same consideration applies to SEPs. If neon is fractionated in our SEP measurements, then it must be fractionated more than the isotopes of C, O, and Mg.

There is a model of the solar flare preacceleration process that seeks to explain the values of $^{22}Ne/^{20}Ne$ reported in solar flares in this work and by Dietrich and Simpson (1979) as a solar flare preacceleration enhancement of a solar wind - like neon composition for the Sun.

Mullan and Levine (1981) have introduced a theoretical model that seeks to explain the abundance enhancements observed in solar flares. They model a flare preacceleration process that takes place inside a collapsing neutral current sheet, in a magnetic flux tube loop. They assume that in such a structure the maximum temperature of the loop may regulate itself so that the collapse time scale, t_B, is only slightly smaller than the proton Coulomb loss time t_p. In such a situation, ions with atomic charges, $Z^2 \leq A$, are preheated along with the protons because they gain energy from the collapsing magnetic field at

a rate, $1/t_B$, and lose energy at a rate, t_l, such that $t_l \le t_p \le t_B$. The populations of preheated ions might be converted to element abundance enhancements in SEPs by a SEP acceleration process that accelerated only particles above a certain energy threshold, for example.

The Mullan and Levine model predicts that the SEP abundances for charges in the regions around Si and Fe will be enhanced compared to elements in the charge regions S-Cl and C-O. The abundance enhancements in this model may vary depending on assumptions made about conditions at the flare site. Mullan and Levine do not propose specific models for the possible flare to flare abundance variations.

Mullan (1982) has applied Mullan and Levine's (1981) model to SEP isotope enhancements. Mullan finds enhancements of neutron rich isotopes of various elements for certain values of ε in the relation

$$t_p = (1 - \varepsilon)\, t_B \qquad\qquad (5.6.2)$$

that defines the relation between the magnetic collapse time and the Coulomb energy loss time. Mullan introduces a measure of inhomogeneity into the preflare conditions at the flare site by integrating the fractions of various ions that are preheated over a distribution of ε values. For a distribution for ε that is constant for $|\varepsilon| \le \delta\varepsilon$ and zero for $|\varepsilon| \ge \delta\varepsilon$, and for $\delta\varepsilon \approx 0.20$, Mullan finds that the preheat mechanism would enhance the $^{22}Ne/^{20}Ne$ ratio more than for other measured isotope ratios.

The theory predicts that enhancements in the abundance ratio $^{13}C/^{12}C$ will be produced for the same flare site conditions that produce the $^{22}Ne/^{20}Ne$ enhancements. Future high precision measurements of correlations between $^{13}C/^{12}C$ and $^{22}Ne/^{20}Ne$ would be strong evidence for the Mullan and Levine, and Mullan models. Unfortunately, the Mullan and Levine theory has too many free parameters for a precise element by element comparison with SEP measure-

ments.

There is a need for more measurements. SEP measurements of isotope abundances should be made for more flares, to assess the extent of variability of the isotope abundances. Difficult measurements of the present day solar wind isotopic composition for C, N, O, Mg, and other common elements that are not noble gases, should be attempted.

5.7. Spectral Correction to Isotope Abundance Ratios

A subsidiary issue that has been left unmentioned so far is the question of making corrections to the isotope abundance ratios based on considering the spectra as functions of energy/nuc or total momentum. There are two possible ways to discriminate between the two hypotheses. One method to discriminate between the energy/nuc and total momentum isotope abundance corrections, is to plot isotope abundance ratios vs. energy and correct in turn for energy/nuc and total momentum. If one hypothesis produced an isotope abundance ratio that was approximately constant as a function of energy, and the other hypothesis did not, then a choice could be made. Unfortunately, marginal statistics would make such a test inconclusive when applied to the isotope abundance ratios measured for the 78:266 flare.

A second method considers the isotope abundance ratios integrated over all energies. The ratio of the energy/nuc correction to the total momentum correction, for the $^{26}Mg/^{24}Mg$ abundance ratio in RANGEs 2-4, is $0.856/1.444 = 0.59$, a considerable difference. Table 5.7.1 lists the isotope abundance ratio results for the 266 flare corrected for the total momentum functional dependence. Also listed in table 5.7.1 are the ratios of the correction factors for total momentum to the correction factors for energy/nuc. Table 5.7.1 lists the factors by which to multiply the isotope ratio results of section 4.2 in order to obtain isotope abundance ratios corrected for total momentum or equivalently,

rigidity.

The reduced differences of SEP minus solar isotope abundance are all positive, when we correct for total momentum, and much larger than would be expected from random statistical fluctuations. Then we conclude that the spectra of the heavier isotopes are better represented by a spectral shape that is a function of energy/nuc.

5.8. Conclusions

We have measured isotope abundance in a large solar flare for the elements of He, C, N, O, Ne, and Mg. The element abundances in the flare are not very different from the SEP average of Cook (1981). The 78:266 flare is slightly depleted in elements heavier than oxygen and in iron, relative to the four flare average of Cook(1981). The SEP isotope abundances observed in the flare agree with terrestrial and solar isotope abundances, with the exception of neon. The neon isotopic abundance we measure for the flare, $^{22}Ne/^{20}Ne = 0.109+0.026-0.019$, is different from the neon isotope abundance measured by Geiss et al. (1972) for the solar wind, $^{22}Ne/^{20}Ne = 0.073 \pm 0.002$. The neon isotopic abundance for this flare is the same as "planetary neon", or neon-A, which Cameron (1981) has adopted as a solar system value.

Separate arguments appear to rule out simple linear mass fractionation in the solar wind and in our SEP measurements as the cause of the discrepancy in the composition of the apparent compositions of these two sources of solar material.

SEP and Solar Isotope Abundances
(SEP corrected for energy/nuc)

Table 5.6.2 -

Ratio	solar abundance	source	SEP measurement	reduced[a] difference SEP - solar
$^3He/\,^4He$	4.3×10^{-4}	Geiss *et al.* (1972)	≤ 0.0026	---
$^{13}C/\,^{12}C$	0.0111	Cameron (1980)	$0.0095 + 0.042 - 0.029$	-0.4
$^{15}N/\,^{14}N$	0.0037	"	$0.008 + 0.010 - 0.005$	+0.9
$^{18}O/\,^{16}O$	0.0020	"	$0.0015 + 0.0011 - 0.0007$	-0.5
$^{22}Ne/\,^{20}Ne$	0.073	Geiss *et al.* (1972)	$0.109 + 0.026 - 0.019$	+1.9
$^{25}Mg/\,^{24}Mg$	0.129	Cameron (1980)	$0.148 + 0.046 - 0.028$	+0.8
$^{26}Mg/\,^{24}Mg$	0.142	"	$0.148 + 0.043 - 0.025$	+0.3

[a] The reduced difference between the SEP and solar abundances is the difference between the SEP and solar abundances divided by the error bar for the SEP measurement.

Isotope Abundances Corrected for Total Momentum

Table 5.7.1 -

Ratio	(total momentum correction)/ (energy/nuc correction)	SEP abundance ratio corrected for momentum	reduced[a] difference SEP - solar
$^{13}C/^{12}C$	1.390	0.0132 + 0.0058 − 0.0040	+0.5
$^{15}N/^{14}N$	1.356	0.010 + 0.014 − 0.005	+1.2
$^{18}O/^{16}O$	1.656	0.0025 + 0.0019 − 0.0012	+0.4
$^{22}Ne/^{20}Ne$	1.611	0.175 + 0.043 − 0.030	+3.4
$^{25}Mg/^{24}Mg$	1.302	0.192 + 0.060 − 0.034	+1.9
$^{26}Mg/^{24}Mg$	1.687	0.249 + 0.073 − 0.042	+2.6

[a] The reduced difference between the SEP and solar abundances is the difference between the SEP and solar abundances divided by the error bar for the SEP measurement.

Appendix A - Hodoscope Efficiency

To calculate spectra we must be able to compute the efficiency, or the percentage of a given type of particle eliminated, for various restrictions placed on the data set. In detectors M1 and M2, the "signal defect" problem discussed in section 3.5.1, makes it difficult to determine the efficiency of hodoscope coincidence requirements directly from flight data. We identify elements in the low resolution data set by two parameter analysis. When we must use the matrix detector energies in the two parameter analysis, for RANGEs 0 or 1, the " signal defect" problem could cause us to misidentify elements. For example, particles near the carbon track may be carbon nuclei or they may be oxygen nuclei, with a pulse height defect. To be sure that we identify the elements correctly, we must require that only one matrix detector strip be triggered in each plane of the hodoscope. Then to calculate spectra for each element and RANGE, we need to know what fraction of the total events have single strip matrix detector triggers.

If the percentage of events with double strip triggers varies with energy deposited in the matrix detectors, then analysis of flight data from RANGEs 0 and 1 to determine those percentages would involve a complicated deconvolution procedure with simultaneous fits to element abundances, energy spectra, and double strip fractions as a function of energy. Flight data from RANGEs 2-8 can be used over a portion of the necessary energy range, but suffers from statistical limitations. Thus we chose to compute the double strip efficiency from calibration data taken at the Bevalac in Berkeley. The same silicon detectors were used for M1 and M2 in flight and for the Bevalac run. We looked for a relation between the probability of a double strip event in either plane of a matrix detector and the energy deposited in that detector.

An ^{56}Fe beam at ≈ 600 MeV/nuc was incident on a target of polyethylene

($n(CH_2)$). The ^{56}Fe beam and the products of nuclear reactions in the target stopped in HIST. The same procedure was followed with a ^{15}N beam at ≈ 600 MeV/nuc. As a result we collected data on nuclei with charges $Z = 7$ to 26 that primarily stopped in the back detectors (D5 to D8) of HIST.

We investigated the hypothesis that the fraction of events with double strip triggers in M1 or M2 depended on the total amount of energy deposited in M1 or M2. Three sets of calibration data were considered. ^{56}Fe ions that stopped in RANGEs 2-8, ^{28}Si, ^{29}Si and ^{30}Si ions that stopped in RANGEs 4-8, and ^{15}N ions that stopped in RANGES 4-8. Each RANGE was divided up into a number of energy intervals and a histogram of the M1 energy was accumulated for the single strip events in each interval.

Figure 3.8.1a is an example of a histogram of the M1 energies for events that stopped in one of the RANGE 4 energy intervals, for events with single strip triggers. Figure 3.8.1b is a histogram of events that stopped in the same RANGE 4 energy interval, and had double strip triggers in the "v plane" of M1. The mean energy deposited in M1 was computed from the histogram for the single strip events. The energy deposited in M2 is not read out of HIST, for RANGEs 4-8. We calculated the energy deposited in M2 corresponding to the mean M1 energy, using a range-energy relation with the Barkas and Berger correction of section 2.6.4.

For each energy the percentage of double strip triggers in either plane of a matrix detector was computed. Figure 3.8.2 shows the results plotted vs. energy deposited in M2. There is a smooth trend with energy and the values derived using different charges agree in regions where the data sets overlap. Data points from oxygen RANGE 2 and 3 events observed in flight are also plotted, and agree with the calibration data. The solid line in figures 3.8.2 is a fit to the calibration data, consisting of three line segments specified by six free

parameters. A quantitatively similar graph and fit were obtained for detector M1.

The functional form of the fit to the calibration data is given by the function P_{hole} (detector, E_{dep}), where "detector" specifies M1 or M2, and E_{dep} is the energy in MeV deposited in the specified detector. The highest energy for which this correction is used would correspond to a ^{28}Si nucleus that just stops in 50 μ of silicon, the nominal thickness of M1 or M2, and is about 140 MeV.

The matrix detectors are constructed with $\approx$ 3/4 mm. wide metal charge collection electrodes or strips and a $\approx$ 1/4 mm. gap between the strips. When a particle enters the gap between two strips, the charge divides and part goes to each strip. We might expect that as the energy deposited in the matrix detector gap increases, it would be more likely for the amount of charge in both strips surrounding the gap to be above the threshold for triggering. We then expect the double strip probability to rise slowly with the amount of energy deposited in the matrix detector. The maximum probability for a double strip in either plane of a matrix detector with a 1/4 mm. gap would then be $\approx (1 - 0.75)^2 \approx 44\%$.

We do not understand the reason for the fall off in double strip probability above 100 MeV, but it is observed to be quantitatively similar for detectors M1 and M2.

figure 3.8.1a-b - Histograms of the energy measured in detector M1, for ⁵⁶Fe events that stop in a restricted energy range of RANGE 4. Figure 3.8.1a is for single strip triggers and figure 3.8.1b is for double strip triggers.
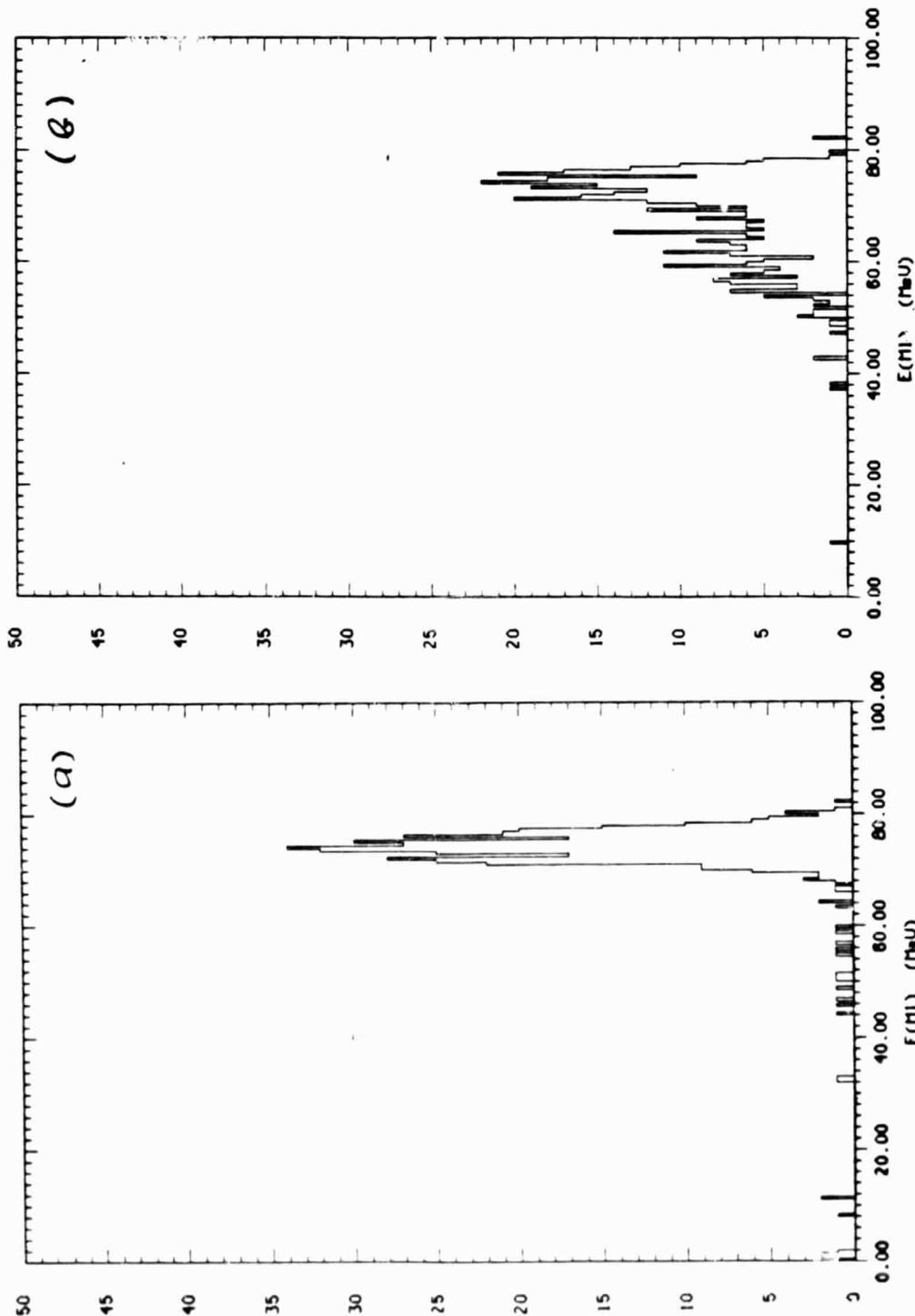
**figure** 3.8.2 - The probability of a double strip event in detector M2 is plotted as a function of the energy deposited in detector M2. Crosses are ^{15}N calibration data in RANGEs 4-8, solid squares are ^{28}Si, ^{29}Si, and ^{30}Si calibration data from RANGEs 4-8, and the solid triangles are ^{56}Fe calibration data from RANGEs 2-8. The open circles are oxygen flight data from RANGEs 2 and 3.
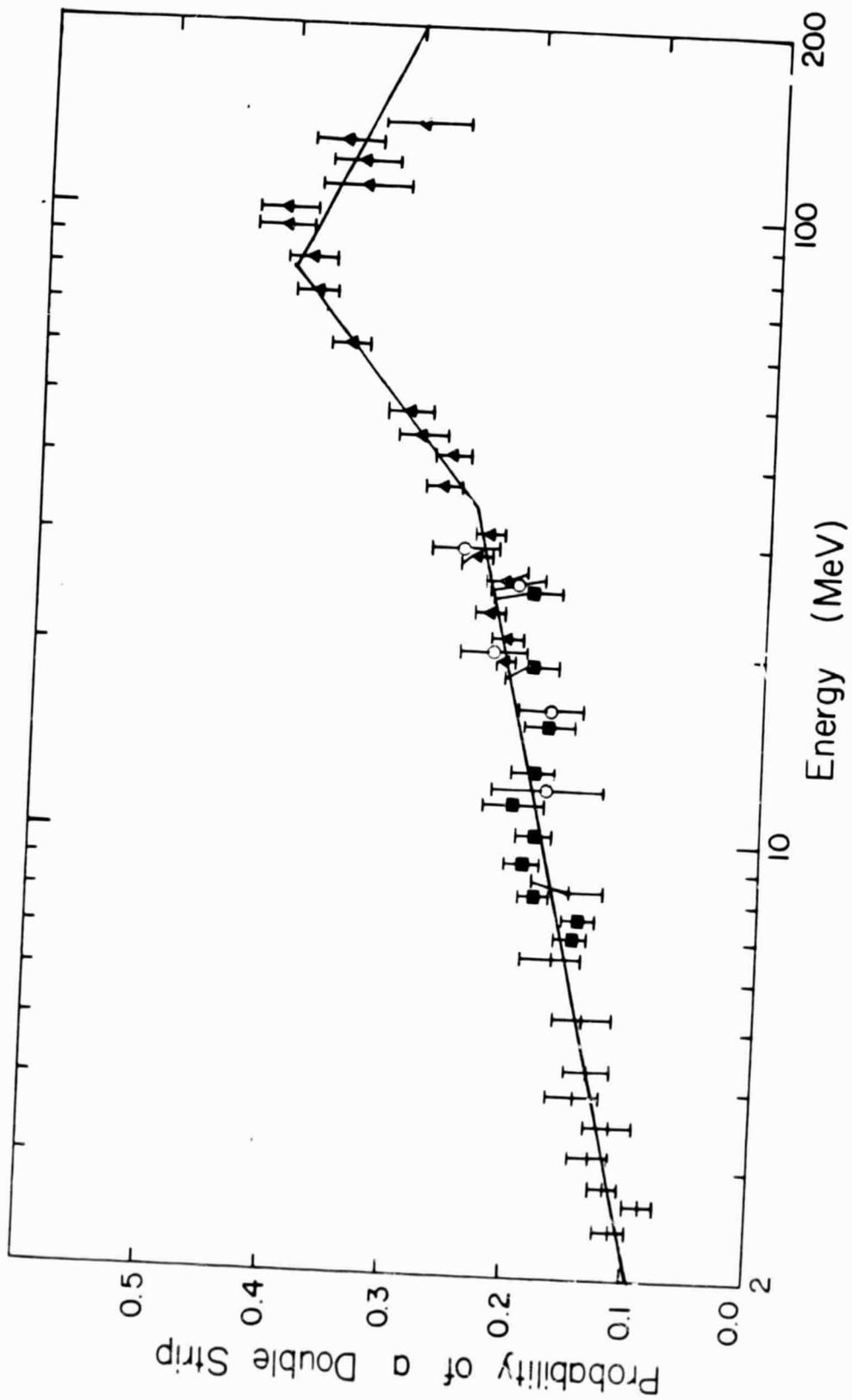
References

Althouse, W. E., Cummings, A. C., Garrard, T. L., Mewaldt, R. E., Stone, E. C., and Vogt, R. E. 1978, "A Cosmic Ray Spectrometer", *IEEE Transactions on Geoscience Electronics*, **GE-16**, 204-207.

Anglin, J. D. 1975, "The Relative Abundances and Energy Spectra of Solar-Flare-Accelerated Deuterium, Tritium, and Helium-3", *Astrophysical Journal*, **198**, 733-753.

Athay, R. G. 1976, *The Solar Chromosphere and Corona: Quiet Sun*, D. Reidel Publishing Company, Dordrecht, Holland.

Bame, S. J., Asbridge, J. R., Feldman, W. C., Fenmore, E. E., and Gosling, J. T. 1979, "Solar Wind Heavy Ions From Flare-Heated Coronal Plasma", *Solar Physics* **62**, 179-201.

Barkas, W. H. and Berger, M. J. 1964, "Tables of Energy Losses and Ranges of Heavy Charged Particles", NASA SP-3013,103-125.

Becker, R. H. 1980, "Evidence For a Secular Variation in the $^{13}C/^{12}C$ Ratio of Carbon Implanted in Lunar Soils", *Earth and Planetary Science Letters*, **50**, 189-196.

Becker, R. H., and Clayton, R. N. 1975, "Nitrogen Abundances and Isotopic Compositions in Lunar Samples", *Proc. 6th Lunar Science Conf.*, **2**, 2131-2149.

Bertolini, C., and Coche, A. 1968, *Semiconductor Detectors*, North Holland Publishing Company.

Black, D. C. 1972a, "On the Origins of Trapped Helium, Neon and Argon Isotopic Variations in Meteorites -- I. Gas-Rich Meteorites, Lunar Soil and Breccia", *Geochimica et Cosmochimica Acta*, **36**, 347-375.

Black, D. C. 1972b, "On the Origins of Trapped Helium, Neon and Argon Isotopic Variations in Meteorites -- II. Carbonaceous Meteorites", *Geochimica et Cosmochimica Acta*, **36**, 377-394.

Branch, D. 1970, "Isotopes of Magnesium in the Sun", *Astrophysical Journal*, **159**, 39-49.

Breneman, H. 1980, "Element and Isotope Identification from HIST Data Subsequent to the December 1, 1978 Readout Failure", *Space Radiation Laboratory Internal Report #75*, California Institute of Technology.

Boyer, R., Henoux, J. C., and Sotirovski, P. 1971, "Isotopes of Magnesium in the Solar Atmosphere", *Solar Phys.*, **19**, 330-337.

Cameron, A. G. W. 1981, "Elemental and Nuclidic Abundances in the Solar System", *in Essays in Nuclear Astrophysics*, ed. by C. A. Barnes, D. D. Clayton, and D. N. Schramm, Cambridge University Press.

Clayton, R. N., Grossman, L., and Mayeda, T. K. 1973, "A Component of Primative Nuclear Composition in Carbonaceous Meteorites", *Science* **182**, 485-488.

Coffey, H. E. (ed.) 1979, *Solar Geophysical Data*, **415-416**, part II.

Cook, W. R. 1981, "The Elemental Composition of Solar Energetic Particles", *thesis, California Institute of Technology*.

Cook, W. R., Stone, E. C., and Vogt, R. E. 1980, "The Elemental Composition of Solar Energetic Nuclei", *Astrophysical Journal*, **238**, L97-L101.

Dietrich, W. F., and Simpson, J. A. 1979, "The Isotopic and Elemental Abundances of Neon Nuclei Accelerated in Solar Flares", *Astrophysical Journal*, **231**, L91-L95.

Dietrich, W. F., and Simpson, J. A. 1981, "The Isotopic Composition of Magnesium Nuclei in Solar Flares", *Astrophysical Journal*, **245**, L41-L44.

Eberhardt, P., Jungek, M. H. A., Meier, F. O., and Niederer, F. 1979, "Presolar Grains in Orgueil: Evidence From Neon-E", *Astrophysical Journal*, **234**, L169-L171.

Eberhardt, P., Geiss, J., Graf, H., Grögier, N., Krähenbühl, U., Schwaller, H., Schwarzmüller, and Stettler, A. 1970, "Trapped Solar Wind Noble Gases, Exposure Age and K/Ar-age in Apollo 11 Lunar Fine Material", *Geochimica et Cosmochimica Acta Suppl.*, **1**, 1037-1070.

Eberhardt, P., Geiss, J., Graf, H., Grögler, N., Mendia, M. D., Mörgeli, M., Schwaller, H., and Stettler, A. 1972, "Trapped Solar Wind Noble Gases in Apollo 12 Lunar Fines 12001 and Apollo 11 Breccia 10046", *Geochimica et Cosmochimica Acta Suppl.*, **3**, 1821-1856.

Epstein, S., and Taylor, H. P. Jr. 1972, "$^{18}O/^{16}O$, $^{30}Si/^{28}Si$, $^{13}C/^{12}C$, and D/H Studies of Apollo 14 and 15 Samples", *Proc. Third Lunar*

Science Conf., **2**, 1429-1454.

Etique, Ph., Signer, P., Wieler, R. 1981, "An In-Depth Study of Neon and Argon in Lunar Soil Plagioclases, Revisited: Implanted Solar Flare Noble Gases", *Lunar and Planetary Science*, **12**, 265-267.

Fisk, L. A. 1978, "^{3}He-Rich Flares: A Possible Explanation", *Astrophysical Journal*, **224**, 1048-1055.

Garcia-Munoz, M., Mason, G. M., and Simpson, J. A. 1977, "The Age of the Galactic Cosmic Rays Derived from the Abundance of ^{10}Be", *Astrophysical Journal*, **217**, 859-877.

Garrard, T. L., Stone, E. C., and Vogt, R. E. 1973, "The Isotopes of H and He in Solar Cosmic Rays", *High Energy Phenomena on the Sun Symposium Proceedings*, ed. R. Ramaty and R. G. Stone (NASA SP-342), 341-354.

Geiss, J. 1973, "Solar Wind Composition and Implications About the History of the Solar System", *Proceedings of the* 13th *Int. Cosmic Ray Conf., Denver*, **5**, 3375-3398.

Geiss, J., Buehler, F., Cerutti, H., Eberhardt, P., and Filleux, Ch. 1972, "Solar Wind Composition Experiment", *Apollo 16 Preliminary Science Report*, NASA SP-315, 14-1 - 14.10.

Geiss, J., Hirt, P., and Leutwyler, H. 1970, "On Acceleration and Motion of Ions in Corona and Solar Wind", *Solar Physics*, **12**, 458-483.

Geiss, J., and Reeves, H. 1972, "Cosmic and Solar System Abundances of Deuterium and Helium-3", *Astronomy and Astrophysics*, **18**, 126-

C - 3

132.

Geiss, J., and Reeves, H. 1981, "Deuterium in the Solar System", *Astron- omy and Astrophysics*, **93**, 189-199.

Gloekler, G., Sciambi, R. K., Fan, C. Y., and Hovestadt, D. 1976, "A Direct Measurement of the Charge States of Energetic Iron Emitted by the Sun", *Astrophysical Journal*, **209**, L93-L96.

Hall, Donald N. B. 1973, "The Detection of ^{13}C, ^{17}O, and ^{18}O Isotope Bands of CO in the Infrared Solar Spectrum", *Astrophysical Journal*, **182**, 977-982.

Hall, Donald N. B. 1975, "Spectroscopic Detection of Solar ^3He", *Astrophy- sical Journal*, **197**, 509-512.

Hall, Donald N. B., Noyes, Robert W., and Ayres, Thomas R. 1972, "The Identification of $^{13}C^{16}O$ in the Infrared Sunspot Spectrum and the Determination of the Solar $^{13}C/^{12}C$ Abundance Ratio", I. Astrophy- sical Journal, **171**, 615-620

Heasley, J. N., and Milkey, R. W. 1978, "Structure and Spectrum of Quies- cent Prominences. III. Applications of Theoretical Models in Helium Abundance Determinations", *Astrophysical Journal*, **221**, 677-688.

Hovestadt, D., Kleckler, B., Volmer, O., Gloeckler, G., Fan, C. Y. 1975, "Heavy Particle Emission of Unusual Composition From the Sun", *Proceedings of the* 14th *Int. Cosmic Ray Conf., Munich, Germany*, **5**, 1613-1618.

Hundhausen, A. J. 1972, *Coronal Expansion and Solar Wind*, Springer-

Verlag, Berlin.

Hurford, G. J. 1975, "Observations of Hydrogen and Helium Isotopes in Solar Cosmic Rays", *thesis, California Institute of Technology.*

Hurford, G. J., Mewaldt, R. A., Stone, E. C., Vogt, R. E. 1975, "Enrichment of Heavy Nuclei in ^{3}He-Rich Flares", *Astrophysical Journal*, **201**, L95-L97.

Janni, J. F. 1966, "Calculations of Energy Loss, Range, Pathlength, Straggling, Multiple Scattering, and the Probability of Inelastic Nuclear Collisions for 0.1 to 1000 MeV Protons", *Air Force Weapons Laboratory TR-65-1500.*

Jordan, C. 1969, "The Ionization Equilibrium of Elements Between Carbon and Nickel", *M. N. R. A. S.*, **142**, 501-521.

Kerridge, J. F., Kaplan, I. R., Lingenfelter, R. E., and Boynton, W. V. 1977, "Solar wind Nitrogen: Mechanisms for Isotopic Evolution", *Geochimica et Cosmochimica Acta Suppl.*, **8**, 3773-3789.

Lambert, D. L. 1967, *Nature*, **215**, 43-44.

Lambert, D. L., Mallia, E. A., and Petford, A. D. 1971, "Magnesium Hydride in the Sun", *M.N.R.A.S.*, **154**, 265-278.

Marmier, P. and Sheldon, E. 1969, *Physics of Nuclei and Particles*, Academic Press, vol 1.

McGuire, R. E., von Rosenvinge, T. T., McDonald, F. B. 1979, "A Survey of Solar Cosmic Ray Composition 1974-1978", *Proceedings of the 16th Int. Cosmic Ray Conf., Kyoto, Japan*, **5**, 61-66.

McGuire, R. E., von Rosenvinge, T. T., and McDonald, F. B. 1981, "Energy Dependence in Solar Cosmic Ray Composition", *Proceedings of the* 17th *Int. Cosmic Ray Conf., Paris, France*, **10**, SH3.1-2, 33-36.

Mason, G. M. Fisk, L. A., Hovestadt, D., Gloeckler, G. 1980, "A Survey of ≈ 1MeV Nucleon^{-1} Solar Flare Particle Abundances $1 \le Z \le 26$, During the 1973-1977 Solar Minimum Period", *Astrophysical Journal*, **239**, 1070-1088.

Mazor, E., Heymann, D., and Anders, E. 1970, "Noble Gases in Carbonaceous Chondrites", *Geochimica et Cosmochimica Acta*, **34**, 781-824.

Mewaldt, R. A. 1980, "Geometry Factors and Other Data for the Heavy Isotope Spectrometer Telescope (HIST) on ISEE-3", *Space Radiation Laboratory Internal Report #76*, California Institute of Technology.

Mewaldt, R. A., Spalding, J. D., Stone, E. C., and Vogt, R. E. 1979, "The Isotopic Composition of Solar Flare Accelerated Neon", *Astrophysical Journal*, **231**, L97-L100.

Mewaldt, R. A., Spalding, J. D., Stone, E. C., and Vogt, R. E. 1981, "The Isotopic Composition of Solar Flare Accelerated Magnesium", *Astrophysical Journal*, **243**, L163-L165.

Meyer, J. P. 1981a, "A Tentative Ordering of All Available Solar Energetic Particles Abundance Observations, I- The Mass Unbiased Baseline", *Proceedings of the* 17th *Int. Cosmic Ray Conf., Paris, France*, **3**, SH3.1-10, 145-148.

Meyer, J. P. 1981b, "A Tentative Ordering of All Available Solar Energetic Particles Abundance Observations, II- Discussion and Comparison

With Coronal Abundances", *Proceedings of the 17th Int. Cosmic Ray Conf., Paris, France*, **3**, SH3.1-13, 149-152.

Mullan, D. J. 1982, "Isotopic Anomalies Among Solar Energetic Particles: Pre-Acceleration in Collapsing Magnetic Neutral Sheets", *preprint*.

Mullan, D. J., and Levine, R. H. 1981, "Preacceleration in Collapsing Magnetic Neutral Sheets and Anomalous Abundances of Solar Flare Particles", *Astrophysical Journal Supplement*, **47**, 87-102.

Neugebauer, M. 1981, "Observations of Solar-Wind Helium", *Fundamentals of Cosmic Physics*, **7**, 131-199.

O'Gallagher, J. J., Hovestadt, D., Kleckler, B., Gleockler, G., and Fan, C. Y. 1976, "Time Dispersion of Energetic Solar Particles Unexpected Velocity and Species Dependence", *Astrophysical Journal*, **209**, L97-L100.

Ogilvie, K. W., Coplan, M. A., Boschler, P., and Geiss, J. 1980, "Abundance Ratios of ^{4}He^{++}/^{3}He^{++} in the Solar Wind", *Journal of Geophysical Research*, **85**, 6021-6024.

Ogilvie, K. W., Durney, A., and von Rosenvinge, T. 1978, "Descriptions of Experimental Investigations and Instruments for the ISEE Spacecraft", *IEEE Transaction on Geoscience Electronics*, GF-16, 151-153.

Ogilvie, K. W., and Hirshberg, J. 1974, "The Solar Cycle Variation of the Solar Wind Helium Abundance", *Journal of Geophysical Research*, **79**, 4595-4602.

Ogilvie, K. W., von Rosenvinge, T., Durney, A. C. 1977, "International Sun-Earth Explorer: A Three-Spacecraft Program", *Science*, 198, 131-138.

Pepin, R. O. 1967, "Trapped Neon in Meteorites", *Earth and Planetary Science Letters*, 2, 13-

Piembert, M. 1975, "Chemical Composition of Extragalactic Gaseous Nebulae", *Annual Reviews of Astronomy and Astrophysics*, 13, 113-131.

Podosek, F. A. 1978, "Isotopic Structures in Solar System Materials", *Annual Reviews of Astronomy and Astrophysics*", 16, 293-334.

Ross, J. E., and Aller, L. H. 1976, "The Chemical Composition of the Sun", *Science*, 191, 1223-1229.

Rossi, B. 1952, *High Energy Particles*, Prentice-Hall Inc.

Sciambi, R. K., Gleockler, G., Fan, C. Y., and Hovestadt, D. 1977, "Direct Measurement of the Ionization States of Energetic Carbon and Oxygen Emitted by the Sun", *Astrophysical Journal*, 214, 316-327.

Schmidt, W. K. H., Rosenbauer, H., Shelly, E. G., and Geiss, J. 1980, "On Temperature and Speed of He^{++} and O^{6+} in the Solar Wind", *Geophysical Research Letters*, 7, 697-700.

Scholer, M., Hovestadt, D., Kleckler, B., Gloeckler, G., and Fan, C. Y. 1978, "Temporal Development of the Energetic Particle Composition During Solar Flares", *Journal of Geophysical Research*, 83, 3349-3354.

Spalding, J. 1981, "Energy Loss Fluctuations in Thick Absorbers", Space Radiation Laboratory Internal Report #81.

Spalding, J. 1983, "A Summary of Some of HIST's Problems", to be published as a Space Radiation Laboratory internal report.

Stone, E. C., and Vogt, R. E. 1972, "Proposal to NASA for an Experiment to Measure the Isotopic Abundances of Heavy Cosmic-Ray Nuclei (3 ≤ Z ≤ 28) with a Heavy–Isotope–Spectrometer Telescope (HIST) on the 1 AU Heliocentric (H) Mission.

Svestka, Z. 1976, *Solar Flares*, D. Reidel Publishing Company, Dordrecht, Holland.

Venkatesan, T. R., Nautiyal, C. M., and Rao, M. N. 1981, "Neon Composition in Solar Flares", *Geophysical Research Letters*, **34**, 1143-1146.

Vidor, S. B. 1975, "Observations of Nitrogen and Oxygen Isotopes in Low Energy Cosmic Rays", *thesis, California Institute of Technology*.

von Rosenvinge, T. T., and Reames, D. V. 1979, "ISEE-3 Measurements of Solar Energetic Particle Composition", *Proceedings of the 16th Int. Cosmic Ray Conf., Kyoto, Japan*, **5**, SP 2-3, 68-73.

Wagoner, R. V. 1973, "Big-Bang Nucleosynthesis Revisited", *Astrophysical Journal*, **179**, 343-360.

Wasserburg, G. J., Papanastassiou, D. A., and Lee, T. 1979, "Isotopic Heterogeneities in the Solar System", *in Les Elements et Leurs Isotopes Dans l'Universe*, Universite de Liege.

Webber, W. R. 1975, "Solar and Galactic Cosmic Ray Abundances - A

Comparison and Some Comments", *Proceedings of the* 14th *Int. Cosmic Ray Conf., Munich, Germany,* **5,** 1597-1602.

Webber, W. R., Roelof, E. C., McDonald, F. B., Teegarden, B. J., Trainor, J. 1975, "Pioneer 10 Measurements of the Charge and Energy Spectrum of Solar Cosmic Rays During 1972 August", *Astrophysical Journal,* **199,** 482-493.

Witte, M., Wibberenz, G., Kunow, H., and Muller-Mellin, R. 1979, "On the Rigidity Dependence of the Mean Free Path $\partial\lambda/\partial P$ for Solar Flare Particles Derived From Their Proton/Helium Time Variations", *Proceedings of the* 16th *Int. Cosmic Ray Conf., Kyoto, Japan,* **2,** 79-84.

Yaniv, A., and Marti, K. 1981, "Detection of Stopped Solar Flare Helium in Lunar Rock 68815", *Astrophysical Journal,* **247,** L143-L146.

Zinner, E. 1979, private communication.

Zinner, E., Walker, R. M., Chaumont, J., and Dran, J. C. 1977, "Ion Probe Surface Concentration Measurements of Mg and Fe and Microcraters in Crystals from Lunar Rock and Soil Samples", *Proc.* 8th *Lunar Science Conf.,* **3,** 3859-3883.